Title
Simulating the interplay between plasma transport, electric field, and magnetic field in the near-Earth nightside magnetosphere

Author
Gkioulidou, Malamati

Publication Date
2012

Peer reviewed|Thesis/dissertation

UNIVERSITY OF CALIFORNIA

Los Angeles

Simulating the interplay between plasma transport, electric field, and magnetic field in the near-Earth nightside magnetosphere

A dissertation submitted in partial satisfaction of the

requirements for the degree Doctor of Philosophy

in Atmospheric and Oceanic Sciences

by

Malamati Gkioulidou

2012

ABSTRACT OF THE DISSERTATION

Simulating the interplay between plasma transport, electric field, and magnetic field in the near-Earth nightside magnetosphere

by

Malamati Gkioulidou

Doctor of Philosophy in Atmospheric and Oceanic Sciences

University of California, Los Angeles, 2012

Professor Larry R. Lyons, Chair

The convection electric field resulting from the coupling of the Earth's magnetosphere with the solar wind and interplanetary magnetic field (IMF) drives plasma in the tail plasma sheet earthward. This transport and the resulting energy storage in the near Earth plasma sheet are important for setting up the conditions that lead to major space weather disturbances, such as storms and substorms. Penetration of plasma sheet particles into the near-Earth magnetosphere in response to enhanced convection is crucial to the development of the Region 2 field-aligned current system and large-scale magnetosphere-ionosphere (M-I) coupling, which results in the shielding of the convection electric field. In addition to the electric field, plasma transport is also strongly affected by the magnetic field, which is distinctly different from dipole field in the inner plasma sheet and changes with plasma pressure in maintaining force balance. The goal of this

dissertation is to investigate how the plasma transport into the inner magnetosphere is affected by the interplay between plasma, electric field and magnetic field. For this purpose, we conduct simulations using the Rice Convection Model (RCM), which self-consistently calculates the electric field resulting from M-I coupling. In order to quantitatively evaluate the interplay, we improved the RCM simulations by establishing realistic plasma sheet particle sources, by incorporating it with a modified Dungey force balance magnetic field solver (RCM-Dungey runs), and by adopting more realistic electron loss rates. We found that plasma sheet particle sources strongly affect the shielding of the convection electric field, with a hotter and more tenuous plasma sheet resulting in less shielding than a colder and denser one and thus in more earthward penetration of the plasma sheet. The Harang reversal, which is closely associated with the shielding of the convection electric field and the earthward penetration of low-energy protons, is found to be located at lower latitudes and extend more dawnward for a hotter and more tenuous plasma sheet. In comparison with simulation runs under an empirical but not force balance magnetic field from the Tsyganenko 96 model, the simulation results show that transport under force-balanced magnetic field results in weaker pressure gradients and thus weaker R2 FAC in the near-earth region, weaker shielding of the penetration electric field and, as a result, more earthward penetration of plasma sheet protons and electrons with their inner edges being closer together and more azimuthally symmetric. To evaluate the effect of electron loss rate on ionospheric conductivity, a major contributing factor to M-I coupling, we run RCM-Dungey with a more realistic, MLT dependent electron loss rate established from observed wave activity. Comparing our results with those using a strong diffusion everywhere rate, we found that under the MLT dependent loss rate, the dawn-dusk asymmetry in the precipitating electron energy fluxes agrees better with statistical DMSP observations. The more realistic loss rate is much weaker than the strong diffusion limit in the inner magnetosphere. This allows high-energy electrons in the inner magnetosphere to remain much longer and produce substantial conductivity at lower latitudes. The higher conductivity at lower latitudes under the MLT dependent loss rate results in less efficient shielding in response to an enhanced convection electric field, and thus to deeper penetration of the ion plasma sheet into the inner magnetosphere than under the strong diffusion everywhere rate.

The dissertation of Malamati Gkioulidou is approved.

Vassilis Angelopoulos

Richard M. Thorne

Chih-Ping Wang

Larry R. Lyons, Committee Chair

University of California, Los Angeles

2012

Στους γονείς μου,

Γιώργο και Βάσω

και στον μικρό μου αδερφό,

Μιλτιάδη

TABLE OF CONTENTS

LIST OF FIGURES

LIST OF TABLES

ACKNOWLEDGEMENTS

First, I would like to thank my advisors, Professor Larry Lyons and Dr. Chih-Ping Wang, for giving me the opportunity to work with their group and most importanly, for being great mentors to me. They immersed me into the world of space physics and instilled in me their child-like enthusiasm for exploring new territories of knowledge. Additionally, they taught me that new discoveries are the result of careful thinking and persistent work with attention to detail.

I am grateful to Professor Richard Thorne and Professor Vassilis Angelopoulos for their guidance as my committee members and for their constructive comments on my dissertation.

Throughout my years in graduate school, I was priviledged to have numerous, valuable discussions with Professor Richard Wolf, Dr. Mike Schulz and Dr. Sorin Zaharia. Their unique physical insight has always helped me tackle the most difficult parts of my research. I was also fortunate to have taken a plasma physics class under the instuction of Professor George Morales whose teaching style was of great inspiration to me.

I am deeply grateful to my undergratuate advisor Professor Loukas Vlahos for suggesting the pursuit of a Ph.D, supporting me througout the preparation process, and being the first to introduce me to the beauty of research and its distinct difference from classwork. I would also like to thank Professor Gaetano Zimbardo because his supervision led to the completion of my undergraduate thesis, which resulted in my very first published paper.

I benefited a great deal from discussions with fellow graduate students Shasha Zou and Sarah Kapnick, as well as with fellow members of our space physics group, Dr. Xiaoyan Xing and Dr. Toshi Nishimura.

I have a special place in my heart for people who have been very close to me throughout the ups and downs of my graduate years: my true friends all around the world. I would especially like to thank Kallia Petraki, whose long path from Greece to UCLA I had promised to follow during our undergraduate years, because her friendship has been invaluable to me, Dmitriy Subbotin for being, by far, the most fun office mate and a loyal friend, and Philip Hon for making my last year at UCLA extra special.

Last but definitely not least, I would like to thank my family for their unconditional love all these years and for always supporting my pursuit of happiness even if it means having to be thousands of miles away from them. *Μαμά, Μπαμπά, Μιλτιάδη σας ευχαριστώ και σας ευγνωμονώ όχι μόνο για την αγάπη και την φροντίδα σας, αλλά κυρίως για την άνευ όρων υποστήριξή σας σε κάθε μου προσπάθεια, ακόμη και σε αυτήν εδώ που με οδήγησε στην άλλη άκρη του κόσμου.*

Chapter 2 is a version of Gkioulidou, M., C.-P. Wang, L. R. Lyons, and R. A. Wolf (2009), "Formation of the Harang reversal and its dependence on plasma sheet conditions: Rice convection model simulations", *J. Geophys. Res., 114*, A07204, doi:10.1029/2008JA013955.

Chapter 3 is a version of Gkioulidou, M., C.-P. Wang, and L. R. Lyons (2011), "Effect of self-consistent magnetic field on plasma sheet penetration to the inner magnetosphere: Rice convection model simulations combined with modified Dungey force-balanced magnetic field solver", *J. Geophys. Res.*, 116, A12213, doi:10.1029/2011JA016810.

Chapter 4 is a version of Gkioulidou, M., C.-P. Wang, Wing S., L. R. Lyons, and R. A. Wolf (2012), Effect of a MLT dependent electron loss rate on the magnetosphere – ionosphere coupling, *J. Geophys. Res*., submitted.

This research was funded by NASA grants NNX07AF66G, NNX09AQ41, NNX07AG42G, and NNX08A135G and by NSF grant ATM-0819864.

VITA

March 3, 1984	Born, Thessaloniki, Greece
2006	B.Sc., Physics Aristotle University of Thessaloniki, Greece
2008	M. S., Atmospheric Sciences Department of Atmospheric and Oceanic Sciences University of California, Los Angeles, USA
2009	NASA Earth and Space Science Fellowship
2011	Jacob A. Bjerknes Award
2006-present	Graduate Student Research Assistant Department of Atmospheric and Oceanic Sciences University of California, Los Angeles, USA

PUBLICATIONS

Gkioulidou, M., C.-P. Wang, Wing S., and L. R. Lyons (2012), Effect of a MLT dependent electron loss rate on the magnetosphere – ionosphere coupling, *J. Geophys. Res*., submitted.

Gkioulidou, M., C.-P. Wang, and L. R. Lyons (2011), Effect of self-consistent magnetic field on plasma sheet penetration to the inner magnetosphere: Rice convection model simulations combined with modified Dungey force-balanced magnetic field solver, *J. Geophys. Res.*, 116, A12213, doi:10.1029/2011JA016810.

Gkioulidou, M., C.-P. Wang, L. R. Lyons, and R. A. Wolf (2009), Formation of the Harang reversal and its dependence on plasma sheet conditions: Rice convection model simulations, *J. Geophys. Res.*, 114, A07204, doi:10.1029/2008JA013955.

Gkioulidou, M., G. Zimbardo, P. Pommois, P. Veltri, and L. Vlahos, High energy particle transport in stochastic magnetic fields in the solar corona (2007), *Astr. Astroph.,* 462,1113-1120.

Lyons, L. R., Y. Nishimura, X, Xing, Y. Shi, M. Gkioulidou, C.-P. Wang, H.-J. Kim, S. Zou, V. Angelopoulos, and E. Donovan, (2011), Auroral disturbances as a manifestation of interplay between large- and meso-scale structure of magnetosphere-ionosphere electrodynamical coupling, *Auroral Phenomenology and Magnetospheric Processes: Earth and other Planets*, AGU monograph.

Wang, C.-P., M. Gkioulidou, L. R. Lyons, R. A. Wolf, V. Angelopoulos, T. Nagai, J. M. Weygand, and A. T. Y. Lui (2011), Spatial distributions of ions and electrons from the plasma sheet to the inner magnetosphere: Comparisons between THEMIS-Geotail statistical results and the Rice convection model, *J. Geophys. Res.*, 116, A11216, doi:10.1029/2011JA016809.

Subbotin, D. A., Y. Y. Shprits, M. Gkioulidou, L. R. Lyons, B. Ni, V. G. Merkin, F. R. Toffoletto, R. M. Thorne, R. Horne, and M. K. Hudson (2011), Simulation of the acceleration of relativistic electrons in the inner magnetosphere using RCM-VERB coupled codes, J. Geophys. Res., 116, A08211, doi:10.1029/2010JA016350.

Chen, L., R. M. Thorne, V. K. Jordanova, C.-P. Wang, M. Gkioulidou, L. Lyons, and R. B. Horne (2010), Global simulation of EMIC wave excitation during the 21 April 2001 storm from coupled RCM-RAM-HOTRAY modeling, *J. Geophys. Res.*, 115, A07209, doi:10.1029/2009JA015075.

Lyons, L. R., C.-P. Wang, M. Gkioulidou, and S. Zou (2009), Connections between plasma sheet transport, Region 2 currents, and entropy changes associated with convection, steady magnetospheric convection periods, and substorms, J. Geophys. Res., 114, A00D01, doi:10.1029/2008JA013743.

CHAPTER 1 | Introduction

1.1 The Earth's magnetosphere

When the solar wind plasma and the interplanetary magnetic field (IMF) reach the Earth and interact with the intrinsic dipolar geomagnetic field, the result is a cavity with a particular magnetic field configuration formed around the earth called the magnetosphere. While the supersonic solar wind approaches the terrestrial magnetic field, a collisionless bow shock is formed to slow the solar wind down. The region between the bow shock and the magnetopause (the outer boundary of the magnetosphere) is called the magnetosheath. *Chapman and Ferraro* [1930, 1931, 1932] proposed a model where the terrestrial magnetic field is compressed at the dayside of the Earth by the highly conducting solar wind. Some of solar wind plasma is able to enter the Earth's magnetosphere and get energized; these particles produce electric currents that stretch the terrestrial magnetic field on the nightside, creating an elongated tail. The Earth's magnetosphere extends from the ionosphere, the atmosphere's ionized layer approximately 100 km above the earth, all the way to hundreds of earth radii (R_E) in the anti-sunward direction (tail region), but only up to ~ 10 R_E in the sunward direction. A schematic of the main regions of the earth's magnetosphere can be seen in Figure 1.1.

There are several ways for the solar wind particles to access the magnetosphere. They can enter directly through the dayside cusp region, or through the open magnetic field lines (a geomagnetic field line is called open if one end is connected to the IMF). The ones that enter through the open field lines flow anti-sunward (called the plasma mantle) and at the same time drift toward the equatorial plane and eventually get into the closed field line region at the distant tail. During periods of northward IMF, the magnetosheath particles can also enter the closed field line region of the magnetosphere through the low latitude magnetopause and form a boundary of cold and dense plasma known as the low latitude boundary layer (LLBL), providing another important source of plasma.

Once inside the closed field line region of the magnetosphere, particles are energized and become much hotter than the magnetosheath particles. This region of "hot" plasma population is confined to near the equatorial plane and is called the plasma sheet, with typical temperatures of ~ 5 keV for ions and ~1 keV for electrons, and number density of 0.1 - 1 cm^{-3}. In fact plasma sheet density and temperature is a combination of a hotter and more tenuous component coming from the tail, and a colder and denser component coming from the flank magnetosheath, with the former prevailing under southward IMF conditions and the latter under northward IMF conditions [*Wing and Newell*, 2002, 2005; *Wang et al.*, 2007].

The plasma sheet is a major plasma and energy storage region in the earth's magnetosphere and plays a crucial role in the generation of plasma and field disturbances causing geomagnetic activity.

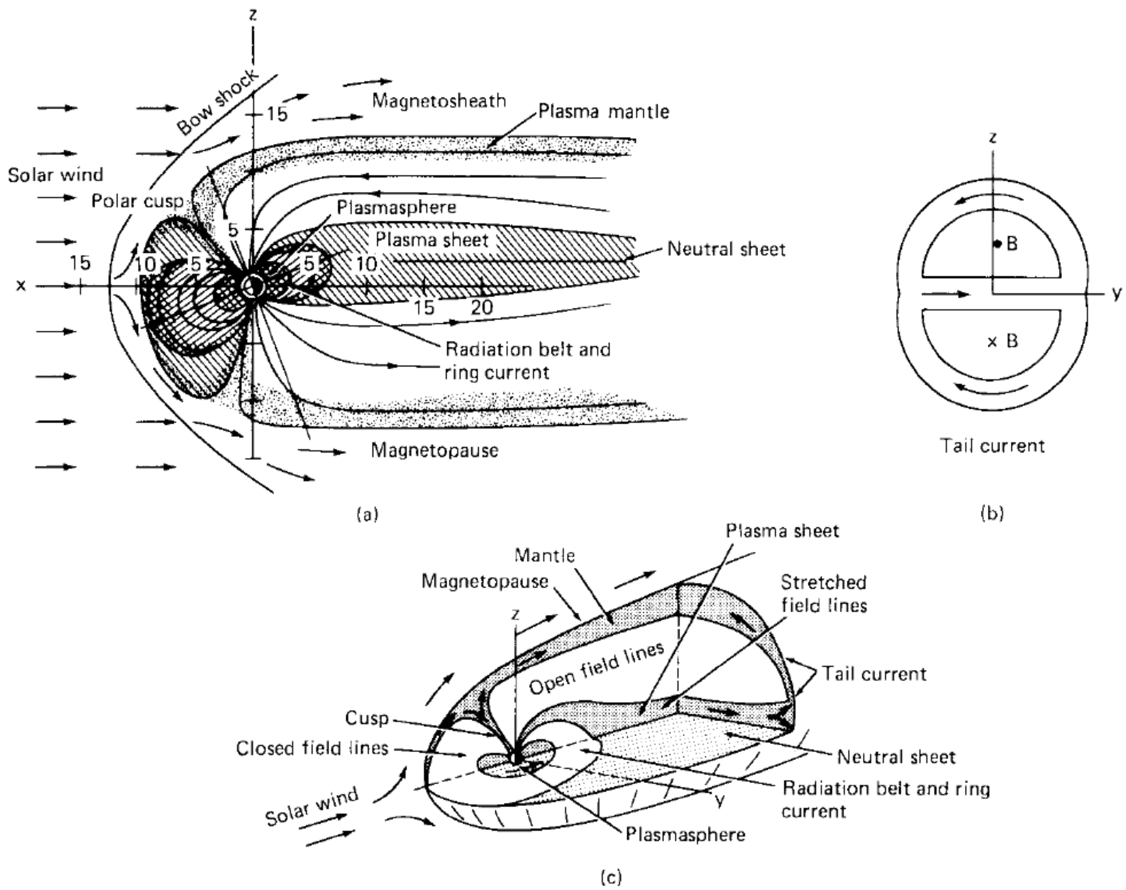

Figure 1.1 Earth's magnetosphere and its main regions. a) Noon-midnight projection, b) tail current systems as viewed from the sun, c) three-dimensional perspective of a) (from *Lyons and Williams* [1984])

1.2 Plasma sheet transport into the inner magnetosphere

The motion of charged particles is restrained by the magnetic field: they gyrate about, and bounce along the field line, and, at longer time scales, they slowly drift perpendicular to the magnetic field.

The large-scale drift motion of the particles is also affected by electric fields. The electric field in the earth's magnetosphere comes from the solar wind. While in the solar wind frame of reference plasma is frozen in with the magnetic field and there is no electric field, in the Earth's frame of reference an electric field appears $\mathbf{E}_{sw} = -\mathbf{V}_{sw} \times \mathbf{B}_{IMF}$, where $\mathbf{V}_{sw}$ is the solar wind velocity, and $\mathbf{B}_{IMF}$ is the IMF. Magnetic field lines are considered as highly conducting, therefore no significant electric potential drops along them. This allows solar wind's electric field to map to the ionosphere along the open magnetic field lines, generating a cross polar cap potential drop, $\Delta\Phi_{PCP}$. The result is a potential difference imposed across the open-closed field line boundary in the magnetosphere, which produces a dawn-to-dusk electric field in the closed field line region [*Lyons and Williams*, 1984]. This electric field, usually referred to as the convection electric field, is the driver of large-scale plasma transport in the Earth's magnetosphere.

Particles coming from the tail plasma sheet first drift earthward due to electric drift $\mathbf{E}\times\mathbf{B}/B^2$ (where $\mathbf{E}$ is the convection electric field mentioned above and $\mathbf{B}$ is the magnetic field). As they move closer to the earth, they gain energy from the convection electric field. As their energy increases, their magnetic gradient/curvature drift, which depends on both energy and the electric charge, $mv_\perp^2(\mathbf{B}\times\nabla B)/2qB^3 + mv_{||}^2(\mathbf{r}_c\times\mathbf{B})/qr_c^2B^2$ (where $\mathbf{r}_c$ is the local radius of the field line curvature, q is the electric charge, and $v_\perp$, $v_{||}$ are the velocities perpendicular and parallel to the magnetic field respectively) also becomes important. The azimuthally directed magnetic drift thus moves the particles around the earth, with electrons towards dawn and ions towards dusk.

Stronger convection electric field results in larger transport speed toward the Earth at the nightside, which is more likely to move particles closer to the Earth. Once reaching the inner magnetosphere (r < ~8 R_E where magnetic field is dominated by the dipole filed), the gradient/curvature drifts of energetic particles (from tens to hundreds of keV) create an electric current circling around the earth, called the ring current.

Plasma and magnetic field are most of time in force balance in the magnetosphere. The earthward convection and energization of particles lead to plasma pressure enhancement. Under the slow flow approximation assumption, when flow velocity is much smaller than the Alfven speed, the inertial terms in the momentum equation can be neglected, and the force balance yields $\nabla P = \mathbf{J}\text{x}\mathbf{B}$ (where P is the plasma pressure and $\mathbf{J}$ is the current density). Thus, plasma pressure and magnetic field are coupled together. The physical interpretation of this coupling is that magnetic field configuration changes in response to plasma pressure change to maintain force balance, and this new magnetic field, in turn, affects particles' drift and energization, and thus changes eventually the plasma pressure.

Plasma sheet and ring current particles under certain conditions can get lost from magnetosphere. An important loss process, especially effective for electrons, is due to encounter with the ionosphere during their bounce motion along the magnetic field lines within the loss cone. Scattering of electrons into the loss cone is mainly due to wave-particle interactions [e.g. *Kennel and Petschek* 1966, *Kennel et al.*, 1970; *Lyons*, 1974; *Villalon and Burke*, 1995] while the current sheet scattering dominates for ions [e.g., *Sergeev et al.*, 1983]. When these charged particles precipitate to the earth's ionosphere, they excite the atmospheric atoms and molecules and create light called aurora. Ions close to the earth can also get lost via charge exchange with neutral exospheric atoms.

1.3 Magnetosphere – Ionosphere (M-I) coupling

The electrodynamic coupling between magnetosphere and ionosphere, through currents that flow between the two regions along the magnetic field lines, is one of the key factors affecting the plasma transport in the earth's magnetosphere.

There are two main large-scale field-aligned current (FAC) systems that connect magnetosphere and ionosphere, the Region 1 (R1) and Region 2 (R2) FAC. Figure 1.2 shows statistical distributions of large-scale FACs for quite time and active periods based on Triad satellite data from *Iijima and Potemra* [1976]. R1 FAC is upward (downward), flowing from (to) ionosphere to (from) magnetosphere, at the duskside (dawnside), and at higher latitudes mapping to the magnetopause and distant tail. The R1 FAC originates from shear stresses at the LLBL and magnetopause [*Sonnerup*, 1980]. The R2 FACs, on the other hand, which are of opposite polarity than the R1 FACs, i.e downward at duskide and upward at dawnside, are located at lower latitudes mapping to near-Earth plasma sheet.

The R2 FAC system, which is the main focus of this study, is generated by plasma spatial distributions in the near-Earth magnetosphere. Due to plasma sheet ions being more energetic than electrons, the duskward magnetic gradient/curvature drifts of ions establish a plasma pressure peak in the premidnight magnetic local times (MLTs) in the near-Earth magnetosphere. This peak causes a westward (eastward) pressure gradient in the dawnside (duskside). The perpendicular current density in the equatorial plane ($\mathbf{J}_\perp$) is associated with the plasma pressure through the force balance relation, $\mathbf{J}_\perp = \mathbf{B} \times \nabla P/B^2$. Pressure and magnetic field gradients give rise to divergence of the equatorial current in the magnetosphere,

$$\nabla \cdot \mathbf{J}_\perp = \nabla \cdot \left(\frac{B \times \nabla P}{B^2} \right) \tag{1.1}$$

However, current conservation in the magnetosphere – ionosphere system implies that the total current density should be divergenceless $\nabla \bullet \mathbf{J} = 0$. Therefore FAC ($\mathbf{J}_{\|}$) flows from and to the ionosphere is necessary for the current continuity, namely

$$\nabla \cdot \mathbf{J} \equiv B \frac{\partial (J_{\|}/B)}{\partial s} + \nabla \cdot \mathbf{J}_{\perp} = 0 \tag{1.2}$$

where $J_{\|} = \mathbf{J} \bullet \mathbf{b}$ where $\mathbf{b}$ is the unit vector along magnetic field $\mathbf{B}$ and $\partial/\partial s$ is the gradient along the field line. Integration of (1.2) over a flux tube with unit magnetic flux yields

$$\frac{J_{\|i}}{B_i} = -\frac{1}{2B_e} \mathbf{b} \cdot \nabla_e P \times \nabla_e V \tag{1.3}$$

where subscript *i* refers to the ionosphere and *e* to equatorial plane, and V is the flux tube volume per unit magnetic flux, $\int ds/B$. Equation (1.3) associates pressure gradients and flux tube volume gradients in the equatorial plane with FACs in the ionosphere and was first introduced by *Vasyliunas* [1970]. More specifically, since ∇V is mainly radial, a westward (eastward) pressure gradient results in upward (downward) FAC flowing out of (into) ionosphere. Therefore, the pressure peak in the premidnight sector in the near-Earth magnetosphere leads to an upward (downward) FAC near the dawnside (duskside), which is exactly the pair of R2 FACs discussed above. Therefore, the R2 FAC is determined by distributions of the plasma pressure and flux tube volumes while plasma pressure and the volume evolve together under force balance.

As within the magnetosphere, current continuity must be maintained in the ionosphere as well. However, plasma in the ionosphere, as opposed to in the magnetosphere, is not collisionless. In fact, in the partially ionized upper atmosphere collisions between the ionized particles and the neutrals in the presence of very strong magnetic field lead to a finite conductivity tensor. There are two elements of the tensor perpendicular to the magnetic field: i) the Pedersen conductivity Σ_P, which determines the Pedersen current in the direction of the electric field $\mathbf{E}_{\perp}$, which is transverse to magnetic field, and ii) the Hall conductivity Σ_H, which determines the Hall current in the direction perpendicular to both the electric and magnetic field. Satisfaction of current continuity in the ionosphere requires an electric field perturbation $\mathbf{\Delta E}$ in the ionosphere that causes Pedersen currents to converge or diverge to compensate for the upward or downward FAC respectively. On the nightside, the $\mathbf{\Delta E}$ is mainly eastward (dusk-to-dawn) in response to an enhancement in the large-scale westward (dawn-to-dusk) convection electric field, and thus acts to decrease the enhanced convection electric field in the near-Earth magnetosphere and prevent particles from moving closer to the Earth. This decrease of the convection electric field is referred to as "shielding". Therefore, in addition to the convection electric field driven by the solar wind and IMF, the M-I coupling also plays a critical role in determining the particle transport into the inner magnetosphere. A schematic of the M-I coupling can be seen in Figure 1.3.

Phenomena observed in ionosphere, such as the Harang reversal [*Harang*, 1946], a region of converging electric fields in nightside ionosphere at auroral latitudes, and the subauroral polarization streams (SAPS) [e.g. *Anderson et al*., 1991; *Foster and Burke*, 2002], enhanced westward flows at the duskside ionosphere, are manifestations of the M-I coupling physics related to magnetospheric plasma transport.

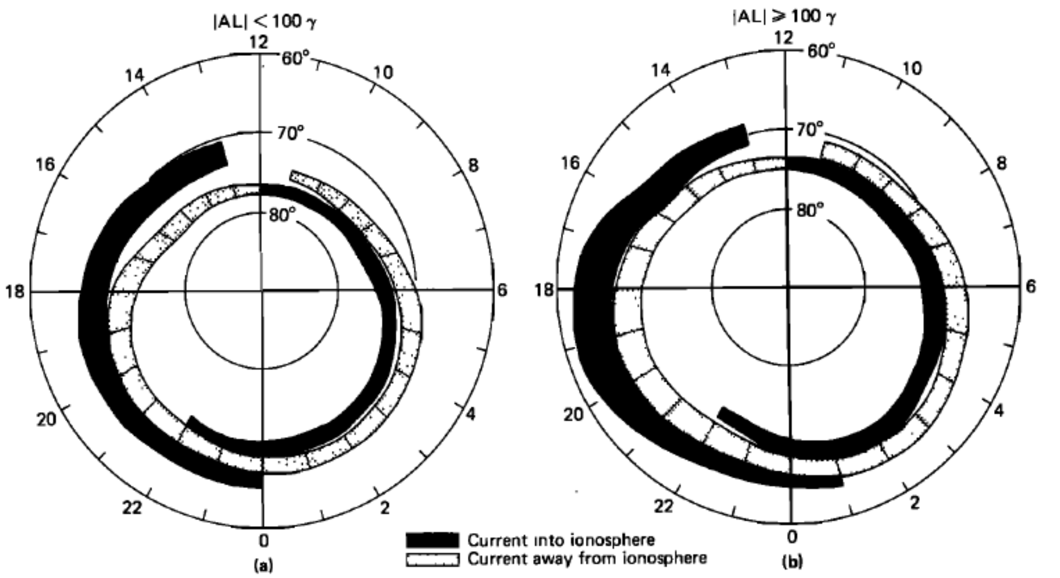

Figure 1.2 Large-scale statistical field aligned current distributions determined from data obtained from Triad satellite passes during a) weakly disturbed conditions and b) active periods (from *Iijima and Potemra* [1978])

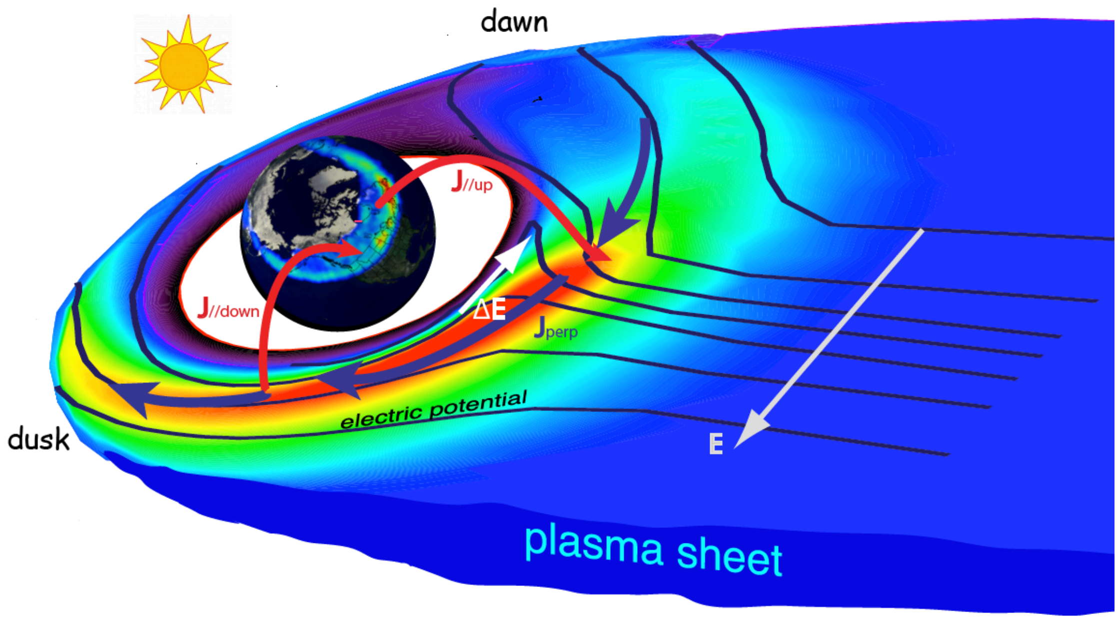

Figure 1.3 Schematic of the large scale Region 2 M-I coupling. Plasma pressure (color contour) and equipotentials (line contours) are from a RCM simulation result. FACs (the red arrows) flow from (to) the ionosphere to (from) magnetosphere towards dawnside (duskside) where the perpendicular current in equatorial magnetosphere (the blue arrows) converges (diverges). The white arrows represent the large-scale dawn-to-dusk convection electric field **E** and dusk-to-dawn electric field perturbation Δ**E** mapped from the ionosphere.

1.4 Importance of plasma sheet transport in causing geomagnetic disturbances

Transport of plasma sheet particles into the near-earth magnetosphere, and the associated magnetic and electric field changes through force balance and M-I coupling, is key to setting up the plasma and electric and magnetic field conditions that lead to major geomagnetic disturbances, such as geomagnetic storms and substorms.

During geomagnetic storms a prolonged and strong southward IMF leads to significant convection enhancement, which injects plasma sheet particles into the ring current region [*Chen et al.*, 1994; *Wang et al.*, 2008]. The ring current intensification causes a southward magnetic field perturbation on the earth's surface at low and mid-latitudes, resulting in a significant decrease of the observed northward geomagnetic field.

Substorms give an explosive brightening of the nighside aurora that subsequently expands both poleward and azimuthally [*Akasofu*, 1964]. The brightening is caused by upward FACs associated with a disruption of the cross tail current in the near-earth plasma sheet. *McPherron et al*. [1973] introduced the current system formed during the substorm's expansion phase as the "substorm current wedge". Although the trigger of the substorm onset is still under debate, recent observations show that substorm onset occurs at the inner edge of the plasma sheet, close to the Harang reversal region, [e.g. *Zou et al.*, 2009], indicating that substorm physics is closely related to the plasma sheet transport and its resulting plasma distributions and R2 FACs in the near-Earth region.

Therefore, to evaluate the conditions for the storms and substorms set up by the plasma transport, it is essential to take into account quantitatively the physical processes controlling the transport in simulations.

1.5 Modeling the plasma transport in the near-earth magnetosphere under self-consistent electric and magnetic fields

As discussed in section 1.3, the R2 electrodynamical coupling between the plasma sheet and ionosphere is driven within the plasma sheet by the spatial gradient in plasma pressure and flux tube volume, which result in divergence in the perpendicular current and thus the FACs. The ionosphere responds to the FACs by modifying the electric field distributions to maintain current continuity, which also depends on distributions of the ionospheric conductivity. The changed ionospheric electric field, in turn, modifies the transport in the magnetosphere and the resulting pressure profile. In fact, the changes in electric field resulting from this M-I coupling tend to shield the inner magnetosphere from the penetrating convection electric field, which is externally driven by the solar wind and IMF.

The FAC structure, and therefore the electric field evolution in response to a convection change depends on the pre-existing state of the plasma sheet [e.g., *Garner et al.*, 2003; *Gkioulidou et al.*, 2009], as well as auroral conductivity [e.g., *Garner et al.*, 2003; *Ebihara et al.*, 2004; *Gkioulidou et al.*, 2009], which is determined by the electron plasma sheet and the electron loss rate. Spatial distribution of the large-scale electric field determines the transport of plasma sheet particles into the inner magnetosphere.

Finally the transport of plasma sheet particles results in plasma heating, and, through force balance, in magnetic field line stretching. In fact, *in situ* observations have shown the magnetic field in the near-Earth region, under storm time convection, to be distinctly different than a dipole field [e.g. *Cahill et al.*, 1966].

Therefore, to quantitatively model the plasma transport into the inner magnetosphere, it is of great importance to include: i) self-consistent interplay between plasma and electric field, through coupling to ionosphere, as well as between plasma and magnetic field, through force-balance, ii) realistic plasma sheet number density and temperature for the particle sources, and iii) realistic electron losses and precipitation which produces the ionospheric auroral conductivity.

Through the years, modeling plasma transport under self-consistent electric and magnetic fields has been a major focus and there has been significant advance in the model development.

There are two main approaches to plasma transport modeling: the kinetic approach, which traces particle trajectories, and the fluid approach, which models the collective behavior of particles.

Some of the kinetic models such as the Hot Electron and Ion Drift Integrator (HEIDI) [e.g. *Liemohn et al.*, 2001] and Comprehensive Ring Current Model (CRCM) [e.g. Buzulokova et al., 2010] have included self-consistent electric field via the Vasyliunas M-I coupling equation (1.3). On the other hand, the Ring Current Atmosphere Model (RAM) has been coupled with a 3-D self-consistent magnetic field solver [*Jordanova et al.*, 2010], while the ring current model by *Chen et al.* [1994] has been combined with a modified Dungey force-balanced magnetic field solver [*Liu et al.*, 2006]. However, all of the above models include either only self-consistent electric field or only self-consistent magnetic field.

Other kinetic models, such as the Magnetospheric Specification Model (MSM) [*Freeman et al.*, 1993] and the Rice Convection Model (RCM) [*Wolf*, 1983; *Toffoletto et al.*, 2003], divide particles of similar energies into subgroups, simulate their dynamics separately taking into consideration the energy dependent magnetic drift, and then sum up together their collective effect. The MSM has no self-consistent electric field, however *Wang et al.*, [2003; 2004] performed MSM simulations maintaining 2-D force balance along the midnight meridian by adding adjustable currents to the empirical Tsyganenko 96 (T96) [*Tsyganenko*, 1995; 1996] magnetic fields. The RCM includes self-consistent electric field through M-I coupling and its equilibrium version, RCM-E [*Toffoletto et al.*, 1996, 2001; *Lemon et al.*, 2004; *Yang et al.*, 2010], has been coupled with a magnetic field relaxation technique developed by *Hesse and Birn* [1993] to obtain force-balanced magnetic field.

Regarding the fluid approach, magnetohydrodynamics (MHD) codes can self-consistently simulate plasma and fields and have also included the ionospheric response to magnetospheric transport [e.g. *Merkin and Lyon*, 2010]. However, in the inner magnetosphere, where the magnetic gradient/curvature drifts are important, the ideal MHD approximation, which requires the frozen-in condition **E** = -**v** x **B** (where **E** is electric field, **B** is magnetic field, and **v** is the plasma flow), in not valid. As a result, although MHD codes have the advantage of simulating the whole magnetosphere's response to highly time variable changes in the solar wind, the effects in the near-Earth plasma sheet cannot be properly evaluated.

In the recent years, there has been a substantial effort to couple different global MHD codes (e.g. BATS-R-US, LFM, Open-GGCM) with inner magnetosphere codes such as the RCM [e.g. *De Zeeuw et al.*, 2004; *Toffoletto et al.*, 2004; *Hu et al.*, 2010; *Pemproke et al., 2012*], however such an approach raises the concern of whether the MHD simulation can provide appropriate plasma density and temperature distributions at the outer boundary of the inner magnetosphere codes.

1.6 Motivation and Dissertation organization

In this study, we use the RCM in order to appropriately evaluate the plasma sheet transport into the near-Earth magnetosphere. As discussed in section 1.5, the RCM takes into account the key processes controlling the particle transport, including the energy-dependent drift transport physics and self-consistently calculates the electric field resulting from M-I coupling. The RCM can be also incorporated with different magnetic field models, including different force-balance magnetic field solvers.

We address three of the most important factors that determine the plasma sheet penetration into the inner magnetosphere:

(1) *Plasma sheet ion and electron sources*

Observations by *Thomsen et al.* [*2003*] have shown that the storm-time ring current depends on the pre-existing plasma sheet state before storms. The CRCM simulations by *Ebihara et al.* [2005] evaluated the impact of the plasma sheet density effect on the storm-time ring current. The RCM simulations by *Garner et al.* [2003] examined the plasma sheet temperature and density effects on the shielding of the near-earth convection electric field. However none of these simulations used realistic plasma boundary conditions based on observations. In Chapter 2, after we describe the RCM, we investigate the effect of a cold and dense versus a hot and tenuous plasma sheet prior to a convection enhancement on the shielding of the convection electric field, and as a result, on the inward plasma sheet penetration after a convection enhancement. For this purpose we have established observed statistical Geotail data as boundary conditions to realistically represent plasma sheet particle sources and the pre-existing plasma sheet state as a function of the interplanetary conditions, radial distance, and MLT. Our investigation reveals the physics behind the formation of Harang reversal and SAPS, phenomena strongly associated with the shielding of the convection electric field and the resulting plasma penetration in the inner magnetosphere. For these simulations we have used the empirical T96 magnetic field model.

(2) ***Force balance***

As explained in sections 1.2 and 1.5, self-consistent modeling of the feedback between plasma and magnetic field is crucial to quantitatively evaluate the plasma transport in the magnetosphere. In Chapter 3 we incorporate the RCM with a modified Dungey force-balanced magnetic field solver to self-consistently calculate the magnetic field according to the RCM plasma pressure and describe the coupled model. We then compare our results of plasma sheet transport after a convection enhancement using force-balanced magnetic field to those from Chapter 2 using the empirical T96 magnetic field, under the same hot and tenuous plasma boundary conditions as in Chapter 2 based on Geotail data.

(3) ***Electron losses and precipitation, and their effects on ionospheric conductivity***

Although the ion population is responsible for establishing the pressure gradients in the near-Earth magnetosphere that lead to magnetic field line stretching via force balance and shielding of the convection electric field via M-I coupling, the electron population and more specifically its precipitation to the ionosphere is the main contributor to the ionospheric conductivity at auroral latitudes, which is a major factor that controls the M-I coupling. The pitch angle scattering of electrons into the loss cone and their precipitation into the ionosphere result from wave particle interactions. In Chapter 4 we conduct different RCM simulations combined with the Dungey force-balanced magnetic field solver, using either a strong diffusion everywhere scattering rate or a realistic scattering rate model based on wave activity established by *Chen and Schulz* [2001]. This allows us to evaluate the effect of the electron loss rate on precipitating electron energy fluxes and ionospheric conductivity, and on the resulting electric field shielding and earthward penetration of the ion and electron plasma sheet. We also evaluate the simulated precipitation electron energy fluxes under different loss rates by comparing them with statistical results from DMSP satellite under similar substorm growth phase conditions.

Finally, in Chapter 5 we summarize the major tasks we have taken to understand the plasma transport into the inner magnetosphere as well as our key findings regarding the underlying physical processes and the resulting plasma and field environment in the near-Earth magnetosphere, which set the stage for storms and substorms.

CHAPTER 2 | Shielding of the convection electric field and its dependence on plasma sheet conditions: a study on the formation of the Harang reversal

The goal of this chapter is to understand the formation of the Harang reversal and its association with the Region-2 field-aligned current (FAC) system, which couples the plasma sheet transport to the ionosphere. We have run simulations with the Rice Convection Model (RCM) using the Tsyganenko 96 magnetic field model and realistic plasma sheet particle boundary conditions based on Geotail observations. Our results show that the existence of an overlap in MLT of the Region-2 upward and downward FAC is necessary for the formation of the Harang reversal. In the overlap region, the downward FAC, which is located at lower latitudes, is associated with low energy ions that penetrate closer to the Earth towards the dawn side, while the upward FAC, which is located at higher latitudes, is associated with high-energy ions. Under the same enhanced convection, we compare the Harang reversal resulting from a hotter and more tenuous plasma sheet with a colder and denser one. For the former case, the shielding of the convection electric field is less efficient than for the latter case, allowing low-energy protons to penetrate further earthward and resulting in a Harang reversal that extends to lower latitudes, expands wider in MLT, and is located further equatorward than the upward FAC peak and the conductivity peak. The return flows of the Harang reversal in the hot and tenuous case are located in a low conductivity region. This leads to an enhancement of these westward flows, resulting in what is known as SAPS (subauroral polarization streams). The results presented in this chapter are published in *Gkioulidou et al.* [2009].

2.1 Introduction

The Harang reversal is a region of converging electric fields in the nightside ionosphere at auroral latitudes. *Harang* [1946] originally referred to this phenomenon, using magnetometer data, as a discontinuity where the westward and eastward electrojets overlap in local time. However, we prefer to use the term “reversal” for it, since it involves the rotation of electric field vectors from south to north rather than a physical discontinuity.

Latitudinally, across the Harang reversal, **E**×**B** convection flow reverses its direction from eastward, at higher latitudes, to westward, at lower latitudes. Observations of these ionospheric flows, using radar data, have shown dependence of the reversal’s position on geomagnetic activity. More specifically, it moves equatorward when Kp increases [e.g *Nielsen and Greenwald*, 1979], and to earlier (later) MLT when IMF By becomes more positive in the northern (southern) hemisphere [*Rodger et al*. 1984].

The Harang reversal is located near the inner edge of plasma sheet and is closely related to the Region-2 FAC [*Zou et al*., 2009]. Moreover, recent larger scale analyses, also of radar data [*Bristow and Jensen*, 2007; *Zou et al*., 2009], have firmly shown a relationship between the evolution of the Harang reversal and the substorm onset. This last feature reveals the importance of the Harang reversal, since the substorm onset mechanism is still under debate and has been theoretically predicted to be related with the reversal [*Lyons et al.* 2003].

Erickson et al. [1991], using the Rice Convection Model (RCM) simulations with simplified MLT dependent boundary conditions having the number of hot ions reduced on the dawn side, gave a theoretical explanation for the formation of the Harang reversal. They described it as the result of the dawnside depletion of hot ions due to their duskward magnetic drift motion in addition to the absence of energetic ions source from the dawnside low latitude boundary layer.

This depletion causes upward Region-2 FAC to flow from the ionosphere to the plasma sheet. Current continuity in the ionosphere requires convergence of Pedersen currents, and therefore the formation of converging electric fields in the same region. This results in the reversal of the north – south electric field component forming the Harang reversal. However, since pressure and the associated distributions of the Region-2 FAC are contributed mostly by plasma sheet ions and conductivity depends mostly on plasma sheet electrons, boundary conditions that can represent the plasma sheet with realistic MLT dependence are important for quantitatively investigating the formation of the Harang reversal.

In this chapter we evaluate the underlying physical processes of the Harang reversal and determine how the plasma sheet, under different solar wind and IMF conditions, affects the formation and characteristics of the Harang reversal. We use the RCM with realistic plasma sheet boundary conditions based on a statistical study of 11-year Geotail data for 16 different interplanetary conditions. In section 2.3, we show that the dawnside energetic ion depletion effect described by *Erickson et al*. [1991] is by itself not enough; instead, an overlap in the midnight to dawn region of the downward (located at lower latitudes) and upward (located at higher latitudes) Region-2 currents in the midnight to dawn region, due to different drift paths of low and high energy particles [*Harel et al.*, 1981b], is necessary. In section 2.4, we quantitatively characterize the Harang reversal in terms of its MLT and latitudinal extent, as well as in terms of return westward flow in the Harang reversal. We determine the correlation between these properties and our boundary conditions and provide a physical explanation for this correlation. We also show that the auroral conductance, which depends on the plasma sheet electrons, plays an important role in the formation and characteristics of the Harang reversal.

2.2 The Rice Convection Model

2.2.1 Plasma Transport and Distributions

Our study requires a model that can appropriately describe the drift transport physics in the near-Earth magnetosphere and the coupling with the ionosphere self-consistently. The RCM [*Harel et al.,* 1981a; *Toffoletto et al*., 2003] simulates the electric and magnetic drift of ions and electrons and their electrodynamic coupling to ionosphere. More specifically, it calculates the bounce–averaged electric drift and magnetic drift of a flux tube filled with an isotropic distribution of ions or electrons at specified kinetic energies inside the closed field line region of the magnetosphere. In slow flow, a particle's total energy $E + q\Phi$ is conserved as it drifts, where E is the particle's kinetic energy, Φ is the electric potential, and q is the particle's electric charge. For an isotropic particle distribution, which is a good approximation in the plasma sheet [*Stiles et al*., 1978, *Nakamura et al.,* 1991], the particle kinetic energy change can be simply determined by the change in flux tube volume according to the relation $E = \lambda V^{-2/3}$ [*Wolf*, 1983], where λ is constant along a particle's drift path and is called the energy invariant and V is the flux tube volume

$$V = \int_{sh}^{nh} \frac{ds}{B(\vec{x},t)} \tag{2.1}$$

where *nh* and *sh* refer to the northern and southern hemisphere endpoints of the field line in the ionosphere.

For an isotropic particle distribution the bounce-averaged drift velocity $\mathbf{V}_D$ of particles of a given λ at position $\mathbf{x}$ and time t is independent of its pitch angle and can therefore be described as [*Wolf*, 1983],

$$\mathbf{V}_{\mathrm{D}}(\mathbf{x},t) = \frac{\mathbf{B}(\mathbf{x},t) \times \nabla \Phi(\mathbf{x},t)}{|\mathrm{B}(\mathbf{x},t)|^2} + \frac{\mathbf{B}(\mathbf{x},t) \times \lambda \nabla V(\mathbf{x},t)^{-2/3}/q}{|\mathrm{B}(\mathbf{x},t)|^2} \tag{2.2}$$

The first term on the right side of (2.2) is the electric drift and the second term is the magnetic drift. The RCM traces the drift trajectory of particles of different λ within a flux tube using (2.2) with given Φ ($\mathbf{x}$, t) and V ($\mathbf{x}$, t). The RCM grid is specified in the ionosphere, so **B** in equation (2.2) is the magnetic field in the ionosphere. The RCM solves for Φ ($\mathbf{x}$, t) self-consistently with plasma distributions. A 3-D distribution of magnetic fields in the magnetosphere is required for computing V and for mapping from the ionosphere to the plasma sheet. The magnetic field that we use in our simulations is the Tsyganenko 96 magnetic field model (T96) [*Tsyganenko*, 1995; 1996]. The T96 model is capable of providing a realistic large-scale magnetic field configuration within the region from our outer boundary locations (r ~ 20 R_E) to the inner magnetosphere. Therefore, it provides reasonable mapping between the ionosphere and magnetosphere. However, the T96 has limitations for our purposes, including the dawn-dusk symmetry of the magnetic field and that it is not in force balance with the RCM plasma pressure.

In the RCM, particle fluxes are modeled by dividing the energy spectrum into several energy channels (30 channels for electrons and 85 for protons in this study) and by approximating the plasma differential flux within each energy channel by j (E) = j_{k} (E_k), where E_k is the represented kinetic energy of the kth channel. The number of kth channel particles per unit magnetic flux, η_{k}, can be calculated from j_{k}, λ_{k}, and V, and is conserved along the drift trajectory described by equation (2.2) if there are no losses. Two particle species, protons and electrons are simulated in our study.

Each simulation starts from a specified distribution of η_k ($\mathbf{x}$, t = 0) at the model boundary (boundary conditions) and within the model region (initial conditions). No initial η_k is used in our runs. At a later time t_1, particles of different λ which occupied the same flux tube at t = 0 will have drifted apart because of their λ-dependent drift velocities (2.2). Plasma loss is modeled with specified loss rates due to charge exchange for ions and due to pitch-angle scattering for electrons (pitch-angle scattering losses, even under strong diffusion, are too small to be significant for plasma sheet ions). Therefore the spatial distribution of η_k ($\mathbf{x}$) at $t = t_1$ is obtained by tracing the trajectories of λ_k backward in time from $t = t_1$ to $t = 0$ and reducing the η_k values at $t = 0$ by the number of particle lost. The spatial distributions of plasma density n and pressure p for each species are then obtained from η_k ($\mathbf{x}$, $t = t_1$),

$$n(\mathbf{x},\, t) = \sum_k \frac{\eta_k(\mathbf{x},t)}{V(\mathbf{x},t)}, \text{ and } p(\mathbf{x},\, t) = \frac{2}{3}\sum_k \frac{\eta_k(\mathbf{x},t)}{V(\mathbf{x},t)}\lambda_k V(\mathbf{x},t)^{-2/3} \tag{2.3}$$

Temperature T can be obtained from p/nk_B where k_B is Boltzmann's constant.

2.2.2 Self-consistent electric field

In the magnetosphere, as discussed in the introduction, a pressure gradient perpendicular to ∇V causes a divergence or convergence of perpendicular currents. Since current continuity must be satisfied, field aligned currents flow into or out of ionosphere. Using the plasma pressure and flux tube volume, the field-aligned current can be computed according to the Vasyliunas equation [*Vasyliunas*, 1970],

$$j_{\|} = \frac{B_i\hat{b}}{2B_e}\cdot\nabla V \times \nabla p \tag{2.4}$$

where $j_{\parallel}$ is the ionospheric field aligned current density of the northern or southern hemisphere (north-south symmetry is assumed). If ∇V is radial, it is clear that a westward (eastward) pressure gradient results in upward (downward) field aligned currents flowing out of (into) ionosphere. The self-consistent electric field is obtained by satisfying current continuity in the ionosphere as well,

$$\nabla_i \cdot [\ddot{\Sigma} \cdot (\nabla_i \Phi_i)] = -j_{\parallel} \sin(I) = -\frac{B_i}{2B} \hat{b} \cdot \nabla V \times \nabla p \sin(I) \tag{2.5}$$

where $\ddot{\Sigma}$ is the field-line integrated conductivity tensor due to both hemispheres, I is the dip angle of the magnetic field in the ionosphere. Subscript i refers to ionosphere-computed quantities.

With given $\ddot{\Sigma}$ and boundary conditions at the high and low-latitude boundary, (5) can be solved to obtain Φ_i. The conductivity tensor $\ddot{\Sigma}$ includes both the Hall and Pedersen conductivities. The conductance includes Solar-EUV-generated conductance that is estimated from the IRI-90 empirical ionosphere driven by F10.7 and the Ap index, and auroral conductance, which, in this study, is estimated using the electron precipitation from the simulated plasma distributions, assuming 1/3 of strong pitch-angle scattering and the algorithm of *Robinson et al*. [1987]. Conductance change associated with the Region-1 FAC is not included. The electron precipitation rate is currently assumed to be local-time independent. The high-latitude boundary condition for the potential is a Dirichlet boundary condition; the overall strength of convection is determined by setting the total range of potential on the boundary equal to the polar-cap potential $\Delta\Phi_{PC}$. A two-cell convection pattern is assigned to describe the electric potential inside the polar cap. A phase shift is used to describe the rotation of the separation line of the two convection cells relative to the noon-midnight meridian (1 hr MLT westward rotation is used). The low-latitude boundary condition incorporates the effects of the equatorial electrojet.

Note that the RCM includes the contribution to the electric field in the magnetospheric equatorial plane from the induced electric field when time-changing magnetic fields are used for the mapping. Using the Φ solved at each time step, particles are moved to obtain the particle distributions for the next time step, thus completing one circuit around the RCM time loop.

2.2.3 Particle Boundary Conditions

The location of the outer (poleward) boundary is specified as a circle in the equatorial plane that reaches X ~ –20 R_E at midnight and |Y| ~ 15 R_E at dawn and dusk (the center of the circle is at X = -5 R_E and Y = 0). The inner (equatorward) boundary is specified in the ionosphere at the 10^o latitude circle. Along the outer boundary, the proton and electron distributions at different MLT are established from a fitting of two-component kappa distributions, which are a combination of one cold and one hot population, to statistical results from 11 years of Geotail observations. Statistical study of these data has already been done for northward IMF conditions [*Wang et al.* 2007]. In this study we extend the study to obtain the statistical results under southward IMF, which are needed for our boundary conditions. The Geotail results are binned into 16 different interplanetary conditions, each being a combination of three interplanetary parameters: solar wind number density (N_{sw}), solar wind speed (V_{sw}), and the magnitude of the northward (8 cases) or southward (8 cases) IMF B_z ($|B_{z,\mathrm{IMF}}|$), each of them being divided into a low and high energy range. This gives 16 different MLT-dependent boundary conditions that realistically represent the plasma sheet conditions observed corresponding to a variety of interplanetary conditions.

The two-component kappa distribution we use is shown below

$$
f = N_{\mathrm{c}}\left(\frac{m}{2\pi\kappa_c E_{0,\mathrm{c}}}\right)^{3/2}\frac{\Gamma(\kappa_c+1)}{\Gamma(\kappa_c-1/2)}\left[1+\frac{E}{\kappa_c E_{0,\mathrm{c}}}\right]^{-\kappa_c-1}
$$

$$
+N_h\left(\frac{m}{2\pi\kappa_h E_{0,\mathrm{h}}}\right)^{3/2}\frac{\Gamma(\kappa_h+1)}{\Gamma(\kappa_h-1/2)}\left[1+\frac{E}{\kappa_h E_{0,h}}\right]^{-\kappa_h-1} \tag{2.6}
$$

where N is density, m is particle mass, and κ and E_0 are parameters of the kappa distribution (subscript c is for cold population and h is for hot populations, E_0 is the energy of the peak particle flux). The ranges, averages, and standard deviations of the solar wind parameters for each one of the 16 cases are listed in Table 2.1, while the parameters used for the cold and hot population for each one of the 16 cases are listed in Table 2.2 (northward IMF cases) and Table 2.3 (southward IMF cases).

Table 2.1 Ranges (values inside the brackets), averages, and standard deviations of the solar wind density (N_{sw}), solar wind speed (V_{sw}), and the magnitude of the northward (N) or southward (S) IMF B_z ($|B_{z,\mathrm{IMF}}|$) for the 16 interplanetary conditions

Condition	1(N, S) N_{low} V_{low} B_{low}	2(N, S) N_{high} V_{low} B_{low}	3(N, S) N_{low} V_{low} B_{high}	4(N, S) N_{high} V_{low} B_{high}	5(N, S) N_{low} V_{high} B_{low}	6(N, S) N_{high} V_{high} B_{low}	7(N, S) N_{low} V_{high} B_{high}	8(N, S) N_{high} V_{high} B_{high}
N_{sw} (cm^{-3})	[0,6.5]	[6.5,15]	[0,6.5]	[6.5,15]	[0,6.5]	[6.5,15]	[0,6.5]	[6.5,15]
	4.8 ± 1.1	9.7 ± 2.3	4.8 ± 1.2	9.6 ± 2.1	3.8 ± 1.3	8.8 ± 2.0	3.7 ± 1.5	8.9 ± 2.1
V_{sw}	[0,4]	[0,4]	[0,4]	[0,4]	[4,10]	[4,10]	[4,10]	[4,10]
(10^2 km/s)	3.6 ± 0.3	3.5 ± 0.3	3.6 ± 0.2	3.6 ± 0.3	5.1 ± 0.9	4.4 ± 0.4	5.1 ± 0.9	4.5 ± 0.5
$\lvert B_{z,\mathrm{IMF}}\rvert$ (nT)	[0,1.3]	[0,1.3]	[1.3,8]	[1.3,8]	[0,1.3]	[0,1.3]	[1.3,8]	[1.3,8]
	0.6 ± 0.3	0.6 ± 0.4	2.5 ± 1.0	2.8 ± 1.5	0.6 ± 0.4	0.6 ± 0.4	2.5 ± 1.1	2.9 ± 1.4

Table 2.2 Values of κ for hot population, number density and temperature for cold (c) and hot (h) population of electrons (e) and protons (p) for the 8 cases under N IMF conditions. The first number is the value at dusk, the second at midnight and third at dawn. The values for the other nightside MLT are obtained by linear interpolation between these values.

	κ_h	N_h (cm^{-3})	T_h (keV)	N_c (cm^{-3})	T_c (keV)
			N IMF 1		
e	10, 6, 5	0.2, 0.05, 0.14	0.8, 0.8, 0.8	0.15, 0.06, 0.14	0.1, 0.1, 0.1
p	10, 5, 9.5	0.2, 0.06, 0.14	2.5, 4, 2,	0.15, 0.05, 0.6	1, 5, 2
			N IMF 2		
e	8, 7, 6	0.2, 0.15, 0.3	0.8, 0.8, 0.8	0.5, 0.1, 0.8	0.08, 0.12, 0.07
p	10.5, 5, 10.7	0.4, 0.15, 0.5	4, 4, 3	0.3, 0.1, 0.6	1, 3, 1
			N IMF 3		
e	10, 10.5, 8	0.1, 0.06, 0.1	0.6, 0.5, 0.7	0.5, 0.14, 0.7	0.05, 0.1, 0.07
p	10.5, 10.8, 7	0.15, 1, 0.3	2.5, 3.5, 5	0.45, 0.1, 0.5	0.6, 1.5, 1
			N IMF 4		
e	10.5, 8, 9.5	0.15, 0.04, 0.13	0.5, 1.2, 0.7	1, 0.3, 1.07	0.07, 0.07, 0.07
p	10.5, 10, 11	0.4, 0.12, 0.3	3, 4, 1.5	0.75, 0.22, 0.9	0.3, 1.3, 0.4
			N IMF 5		
e	9, 6, 3	0.1, 0.045, 0.2	1, 1, 1	0.15, 0.05, 0.25	0.15, 0.15, 0.15
p	7, 4, 10.5	0.1, 0.045, 0.2	6, 5, 4	0.15, 0.05, 0.25	1, 3, 1
			N IMF 6		
e	10.5, 8, 4	0.2, 0.1, 0.15	1, 1, 1	0.2, 0.03, 0.4	0.1, 0.1, 0.1
p	6, 4, 10.5	0.2, 0.06, 0.15	6, 6, 3	0.2, 0.07, 0.4	1, 4, 1
			N IMF 7		
e	10.3, 6, 4	0.05, 0.03, 0.1	0.8, 0.8, 0.8	0.3, 0.07, 0.4	0.07, 0.15, 0.08
p	10, 7, 11	0.1, 0.06, 0.2	5, 4, 3	0.25, 0.04, 0.3	1, 1.5, 2
			N IMF 8		
e	10.3, 6, 4	0.05, 0.1, 0.3	0.6, 0.8, 0.8	0.7, 0.08, 0.6	0.06, 0.12, 0.07
p	10.5, 8, 10.8	0.15, 0.1, 0.4	4, 4, 4	0.6, 0.08, 0.6	0.6, 4, 1

Table 2.3 Same as Table 2.2 but under S IMF conditions

	κ_h	N_h (cm^{-3})	T_h (keV)	N_c (cm^{-3})	T_c (keV)
			S IMF 1		
e	8, 7, 6	0.1, 0.08, 0.15	0.9, 0.9, 0.9	0.1, 0.02, 0.2	0.1, 0.09, 0.08
p	8, 6, 10.5	0.15, 0.05, 0.15	3, 5, 3	0.05, 0.05, 0.2	1, 4, 1
			S IMF 2		
e	9, 6, 7	0.2, 0.12, 0.3	0.8, 0.8, 0.8	0.2, 0.05, 0.6	0.1, 0.09, 0.07
p	7, 4, 10.5	0.2, 0.1, 0.3	4, 4, 4	0.2, 0.07, 0.6	0.5, 5, 0.4
			S IMF 3		
e	7, 9, 3	0.15, 0.1, 0.18	1, 1, 1	0.04, 0.02, 0.08	0.05, 0.06, 0.08
p	6, 10, 4	0.18, 0.07, 0.2	4, 5, 4	0.01, 0.05, 0.06	1.5, 3, 1
			S IMF 4		
e	8, 6, 7	0.1, 0.13, 0.3	1, 1, 1	0.07, 0.03, 0.1	0.09, 0.09, 0.09
p	5, 4, 11	0.15, 0.1, 0.3	6, 5, 4	0.12, 0.06, 0.1	3, 4, 3
			S IMF 5		
e	7, 6, 4	0.1, 0.05, 0.1	1.2, 1.2, 1.2	0.1, 0.02, 0.3	0.15, 0.1, 0.08
p	7, 4, 12	0.1, 0.05, 0.2	8, 6, 4	0.1, 0.02, 0.2	2, 4, 0.5
			S IMF 6		
e	8, 6, 8	0.15, 0.15, 0.15	1, 1, 1	0.2, 0.05, 0.25	0.1, 0.1, 0.1
p	12, 4, 8	0.15, 0.1, 0.2	6, 9, 4	0.2, 0.1, 0.2	2, 1, 4
			S IMF 7		
e	8, 6, 5	0.06, 0.08, 0.2	1.5, 1.5, 1.5	0.06, 0.02, 0.2	0.15, 0.1, 0.15
p	3, 8, 4	0.06, 0.08, 0.15	8, 8, 8	0.06, 0.02, 0.025	0.4, 1.5, 2
			S IMF 8		
e	5, 5, 5	0.2, 0.12, 0.2	1, 1, 1	0.1, 0.03, 0.3	0.1, 0.15, 0.09
p	6, 4, 12	0.2, 0.1, 0.2	5, 7, 5	0.1, 0.05, 0.3	2, 3, 1

2.3 Physics of Harang reversal formation

We first use the RCM results to examine what are the physical processes that result in the reversal of electric fields in the region of the Harang reversal.

We ran the simulation with constant cross polar-cap potential drop ($\Delta\Phi_{PCP}$) = 30 kV, IMF B_z = 0 and Dst = -10 nT (IMF B_z and D_{st} are used as an input for the T96) for 5 simulation hours, and then step increased $\Delta\Phi_{PCP}$ to 100 kV and decreased IMF B_z to -7 nT and Dst to -11 nT at t = 0 and kept them constant for another 5 hours (two other inputs, Pdyn = 1.7 nPa and IMF B_y = 0, for the T96, are kept constant throughout the simulation). Since the T96 magnetic field is not in force balance with the simulated plasma pressure, we chose the above values for the T96 parameters in order to give typical magnetic field configurations for weak and for enhanced convection conditions. Our plasma boundary conditions are those of case 5N (see Table 2.2) and are kept constant throughout the simulation.

In the top panels of Figure 2.1 we show equatorial plasma pressure, and in the middle panels ionospheric FAC (color contours, negative for upward FAC from and positive for downward to ionosphere) and equipotentials (contours) projected to the equatorial plane, for times t = 4 min, t = 8 min, t = 20 min and t = 1 hr after the increase of the polar cap potential drop. In the bottom panels we show the ionospheric FAC and equipotentials in the ionosphere for the same times. The Harang reversal, identified by a heavy dashed line, starts to form ~20 min after convection is enhanced (t = 20 min) and becomes well developed at t = 1 hr.

At t = 4 min, a pressure peak is located on the dusk side, due to the duskward magnetic drift of high-energy protons. Once a pressure peak is developed, there are both westward and eastward pressure gradients and thus an upward and downward FAC pair is formed, according to equation (2.4). We consider only the azimuthal pressure gradient, because the flux tube volume gradient is mainly in the radial direction. Near midnight, this FAC pair can be seen at X ~-7 to -10 R_E in the equatorial plane and at ~65° latitude in the ionosphere. There is another FAC pair located near midnight at higher latitudes (downward postmidnight, upward premidnight) resulting from our boundary conditions, which have a pressure minimum at midnight. They are actually part of the region-1 currents that extents into the RCM modeling region, though their structure depends substantially on the particle boundary conditions applied. This high latitude pair is not the focus of this study. At this early time, the electric field is only weakly shielded from the region earthward of the plasma sheet. By t = 8 min, particles drift further earthward leading to pressure gradients closer to the Earth and the FAC regions expand equatorward and azimuthally. This strengthens the shielding of the convection electric field from the near Earth region. The shielding effect will be discussed in more detail in section 2.4. At even later times (t = 20 min, t = 1 hr), the shielding is almost fully developed and the formation of the Harang reversal is apparent. Note that when the Harang reversal is formed at t = 20 min, there is a premidnight region of MLT overlap at ~62-64° latitude between the duskside region of substantial (~0.5×10^{-6} A/m^2) downward FAC and the dawnside region of upward FAC, an overlap which does not occur at the earlier times.

We next address the following two questions: What is responsible for the overlap of the upward and downward Region-2 FAC, and why does this overlap result in the Harang reversal?

2.3.1 MLT Overlap of FAC

In order to understand why an overlap region of FAC is created, we need to determine the relative contributions to the FAC from different energy particles in this region. In the left panels of Figure 2.2 we show pressure and the corresponding FAC caused by low-energy (30 eV – 420 eV at boundary location: X ~ -20 R_E at midnight) protons and high-energy (420 eV – 13 keV at the same boundary location) protons, as well as the total FAC contributed by protons of all energies, for time t = 4 min when there is no Harang reversal. In the right panels of Figure 2.2, we show the same quantities for t = 5 hr when the Harang reversal is well developed. Due to the energy dependent magnetic drift, which is different for electrons (dawnward) and protons (duskward), the electron and low-energy proton inner edge is located closer to the Earth on the dawn side, while the high-energy proton inner edge is located closer to the Earth on the dusk side. The closer to the Earth particles penetrate, the more they get energized. As a result, the pressure for electrons and the low-energy protons peaks at midnight towards the dawn side, while the high-energy proton pressure peak extends towards the dusk side. Each of these pressure peaks is associated with a downward and upward FAC pair. Notice the different positions of the centers of these FAC pairs. The boundary between the upward and downward FAC for the low-energy protons is located postmidnight while the boundary for the high-energy protons is located premidnight.

At the earlier time t = 4 min, the peaks of both low- and high-energy particle pressures, and therefore their corresponding FAC pair, are at the same distance from the Earth. This means that the total FAC has no overlap in MLT between the downward and upward FAC and the Harang reversal is not seen. At time t = 5 hr, the low-energy protons, following the electric drift, are able to penetrate further earthward, while the high-energy protons, which are more strongly affected by the magnetic drift, remain further away. This causes the dawn side pressure peak of the low-energy population as well as its associated FAC pair to be located closer to the Earth than for the high-energy population.

Therefore, when the Harang reversal is formed, the Region-2 FAC has an overlap region. The downward FAC associated with low energy protons extends to the same near midnight MLT as does the upward FAC associated with high energy protons, but the downward FAC lies closer to the Earth, that is, at lower latitudes in the ionosphere.

2.3.2 Electric field response to FAC changes

Having demonstrated the cause of the FAC overlap region, we now investigate how the electric field perturbations caused by the changes of the FAC result in the reversal of the total electric field.

We look at changes that occur during two time intervals: (1) t_1 =4 min to t_2 =8 min and (2) t_1 =20 min to t_2 =1 hr. Figure 2.3(a) shows for both time intervals, the FAC change $\Delta J_{//} = J_{//2} - J_{//1}$, the ionospheric Pedersen current change, $\Delta \mathbf{J_{ped}} = \mathbf{J_{ped2}} - \mathbf{J_{ped1}}$ caused by the FAC perturbation, and the direction of the electric field change $\Delta \mathbf{E} = \mathbf{E_2} - \mathbf{E_1}$ associated with the Pedersen current perturbation, as well as the equipotentials for times t_1 and t_2. All the above ionospheric properties are projected to the equatorial plane. We show these properties for the two different time intervals in order to show the electric field perturbations in situations with and without the FAC overlap region, and thus also with and without the Harang reversal.

To illustrate how electric field changes lead to the reversal of north-south electric field component associated with the Harang region, we show only the direction of $\Delta \mathbf{E}$ (unit vectors), which leaves out the effects of conductivity changes. Based on the simulation results, Figure 2.3(b) shows three simple illustrations of the electric field perturbations that lead to the formation of the Harang reversal.

Let us first focus on the first time interval results shown in the two top panels of Figure 2.3(a). At time t_1, 4 min after the potential drop has been increased, the penetrating electric field (dotted equipotentials) is strong. At time t_2 = 8 min, plasma has moved earthward, pressure gradients have built up and therefore FAC appear in the region, downward on the dusk side and upward on the dawn side (color contours). At this time, the low-energy protons have not yet moved closer to the earth than the higher-energy protons, so the two FAC regions do not overlap. Once FAC are flowing into (downward) or out of (upward) the ionosphere, divergence (in the region of downward FAC) or convergence (in the region of upward FAC) of perpendicular Pedersen currents is required to maintain current continuity in the ionosphere. These Pedersen current perturbations $\Delta\mathbf{J}_{\mathbf{ped}}$ are shown in the top left panel. The electric field perturbations $\Delta\mathbf{E}$ associated with these Pedersen currents are shown in the top right panel. For both of the above perturbations white arrows show the total vector and grey arrows show the x-component. Notice that $\Delta\mathbf{E}_{\mathbf{x}}$ is directed earthward in the region of upward FAC and tailward in the region of downward FAC. These electric field perturbations add to the electric fields at t_1 = 4 min. This bends the equipotentials azimuthally, so that some shielding can be seen at t_2 = 8 min (solid equipotentials). Notice also that the shielding in the top panels of Figure 2.3(a) is stronger on the evening side than on the dawn side. The top sketch of Figure 2.3(b) illustrates how this perturbation $\Delta\mathbf{E}_{\mathbf{x}}$ (red arrows), added to the background electric field (green arrows), results in the new, more shielded electric field (black arrows).

During the later time interval, the low-energy protons have moved closer to the earth than the higher-energy protons leading to an overlap region of downward and upward FAC as discussed in section 2.3.1. For this later time interval, we focus on the two different spatial regions separated by a purple dashed line in the bottom panels of Figure 2.3(a).

In the first region (Y_{GSM} from 2 to -1 R_E), we recognize the Harang reversal configuration. Notice that both $\Delta\mathbf{J}_{\mathbf{ped}}$ and the $\Delta\mathbf{E}$**,** which enhances the reversal of the electric fields, change direction from tailward to earthward in the region between the downward and upward FAC perturbations, and not in the region of upward FAC perturbation as inferred by *Erickson et al.* [1991]. The way the electric field perturbations in this region result in the Harang reversal is illustrated in the middle sketch of Figure 2.3(b).

In the second region (Y_{GSM} from 5 to 2 R_E) we notice that the equipotentials at time t_1 extend along the azimuthal direction. This is because the convection electric field has been strongly shielded on the evening side during the first time interval as mentioned before. In this region, the downward FAC perturbation is actually just equatorward of the inner edge of the electron plasma sheet, and is therefore a region of low conductivity. We should mention at this point that the strong shielding results from the very large electric field perturbations in this very low conductivity region. The perturbation $\Delta\mathbf{E}$ in this part of the overlapping region, being in the same direction as in the previous region, increases the total electric field in the region of downward FAC (equipotentials are piled up) and decreases the total electric field in the region of upward FAC (equipotentials are further apart from each other) at time t_2. The increased anti-earthward electric field on the evening side causes a strong westward $\mathbf{E}\times\mathbf{B}$ convection flow, which is known as SAPS and has been observed in the ionosphere [*Anderson et al.*, 1991, *Foster and Burke*, 2002]. Our results agree with the physical explanation that was given for the generation of SAPS by *Southwood and Wolf* [1978]. In section 2.4 we discuss more quantitatively the features of this westward flow, which we treat as part of the Harang reversal region. The electric field perturbations of this region can be seen in the bottom sketch of Figure 2.3(b).

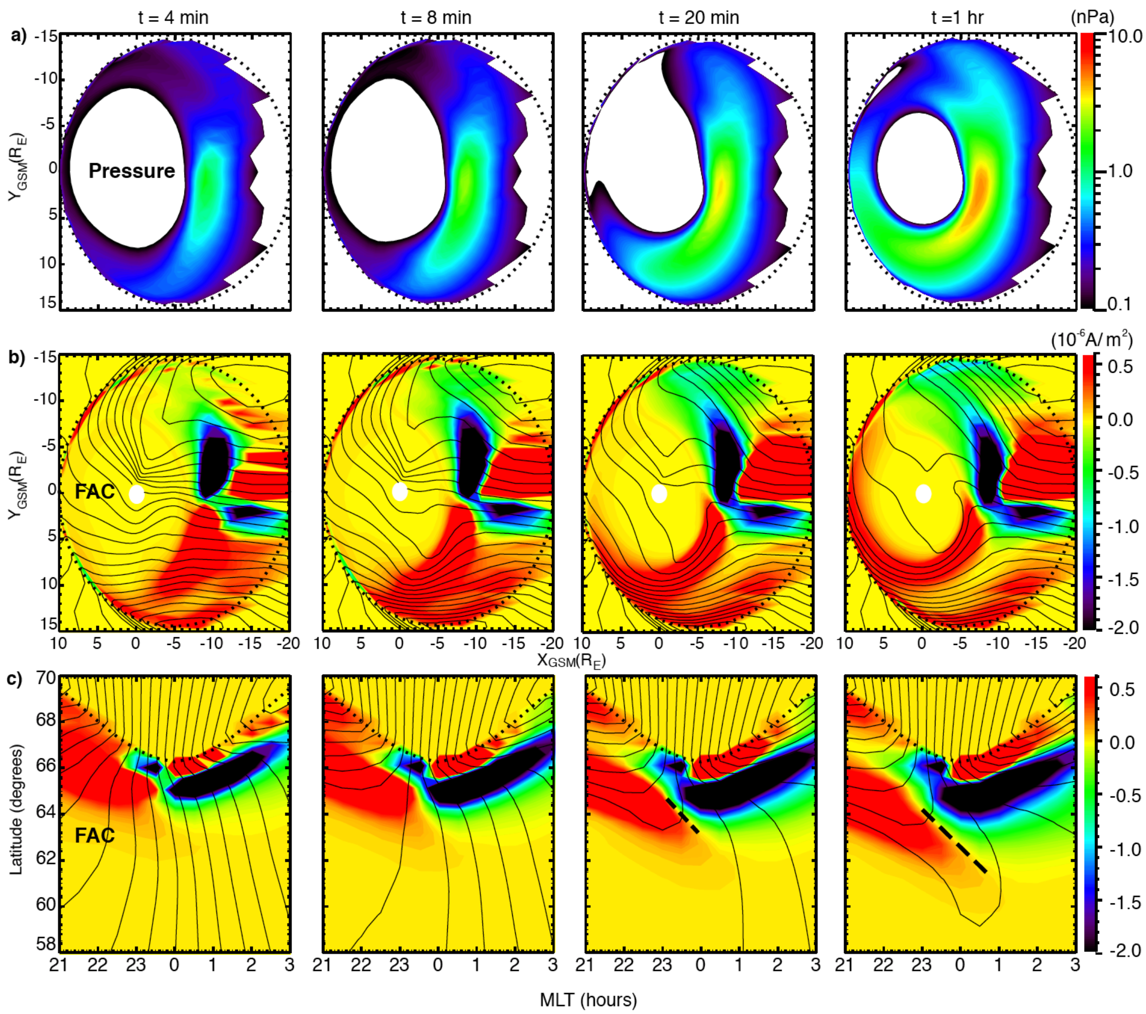

Figure 2.1 (a) Total plasma pressure in nPa at the equatorial plane, (b) Ionospheric field aligned currents (color contour, negative values for upward current from, and positive for downward to the ionosphere) and equipotentials (contours with 5 kV interval) mapped to the equatorial plane (the corotation electric field is not included in these plots), (c) same as (b) but in the ionosphere with 1 kV contour interval, for time t = 4 min, t = 8 min, t = 20 min and t = 1 hr after the increase of the potential drop. The equipotential pattern throughout this chapter does not include the corotation electric field. Dotted black line in all of the panels represents our outer boundary location. The heavy dashed line in the two bottom right panels indicates roughly the location of the Harang reversal.

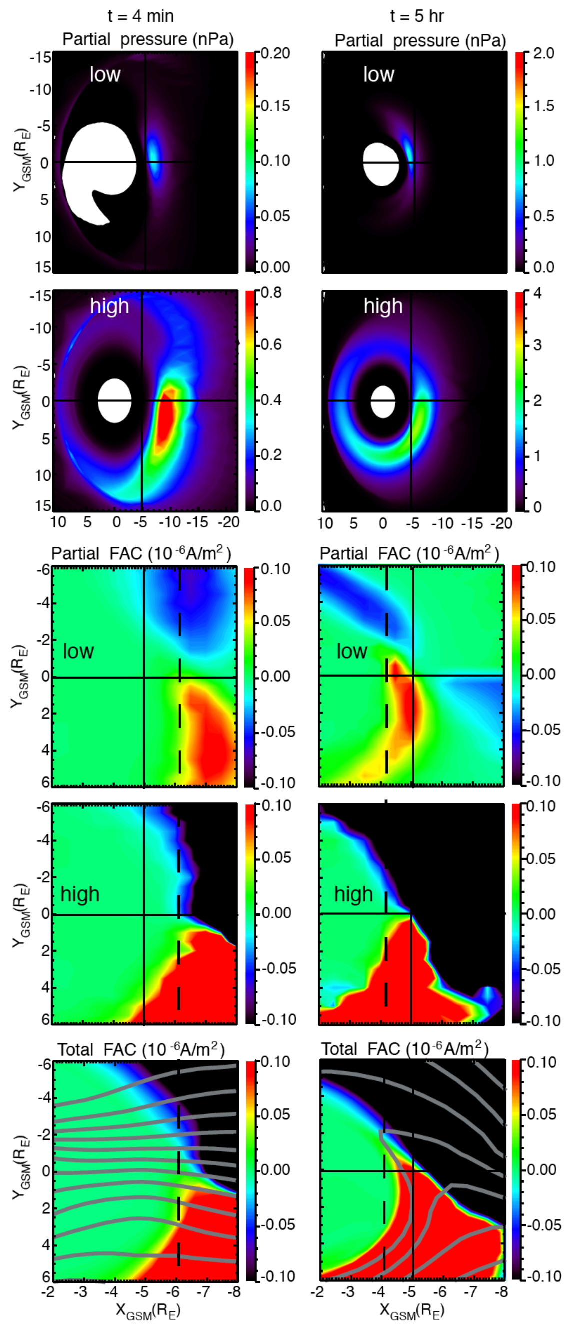

Figure 2.2 From top to bottom: pressure caused by low energy protons (30 eV – 420 eV at the boundary x = 20 R_E and y = 0), pressure caused by high-energy protons (420 eV – 13 keV at the boundary), ionospheric FAC associated with low energy protons, ionospheric FAC associated with high energy protons, and total ionospheric FAC (color contour) with equipotentials (contours), at equatorial plane for time t = 4 min (left column) and t = 5 hr (right column). The dashed line in the FAC panels shows the inner edge of the downward FAC caused by the low-energy protons around the midnight and dawn side.

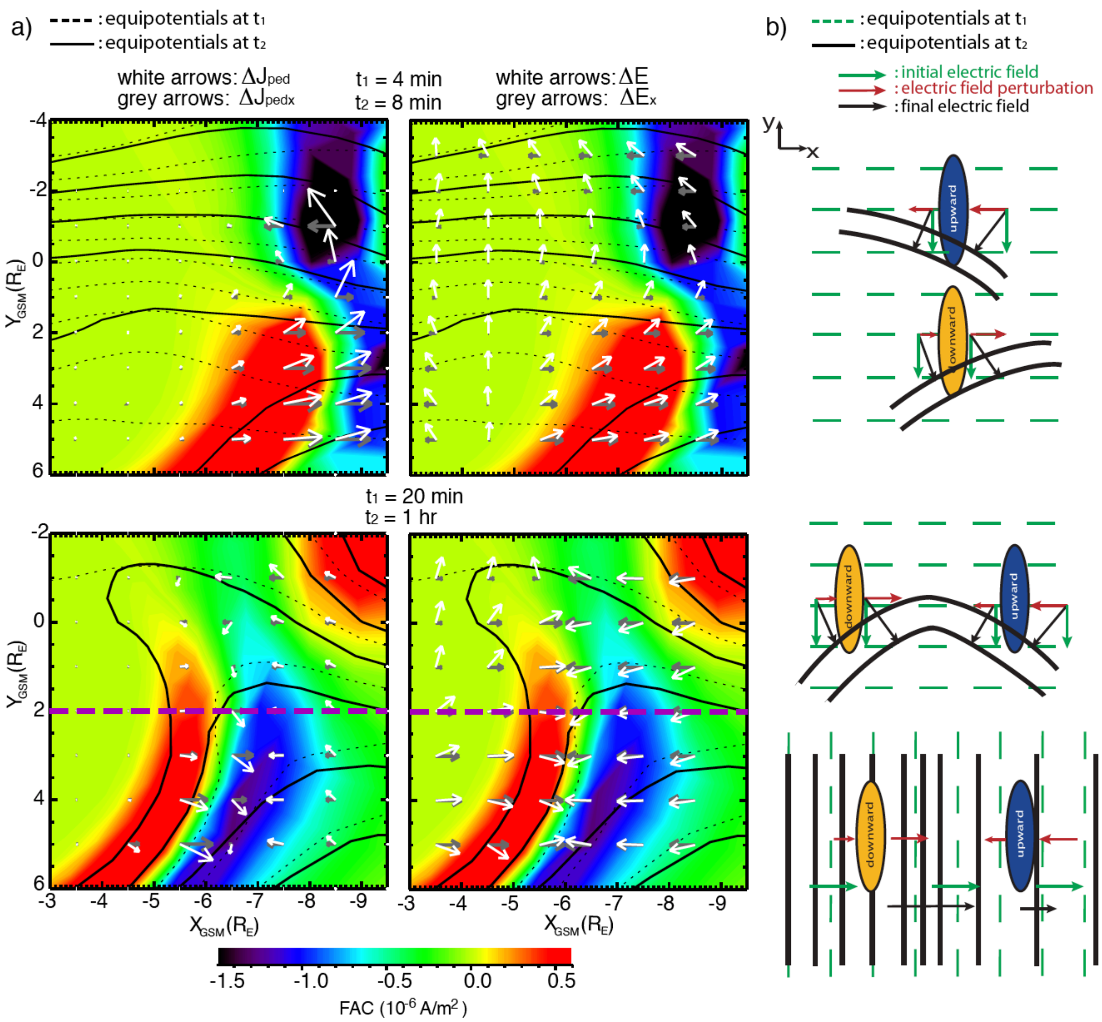

Figure 2.3 (a) Top panels: total vector and x-component of Pedersen current perturbation (left panel), unit vector and x-component of the total electric field perturbation (right panel), for the time interval $t_2 = 8$ min – $t_1 = 4$ min; bottom panels: the same as the top panels but for the time interval $t_2 = 1$ hr – $t_1 = 20$ min. In all of the panels the color contour shows the FAC change $\Delta J_{//}$ and the contours represent the equipotentials for t_1 (dotted) and t_2 (solid), (b) simple cartoon showing initial electric field (green arrows), the FAC change $\Delta J_{//}$, the associated electric field perturbations (red arrows), as well as the final electric field (black arrows); the green dashed lines represent the background equipotentials at t_1, and the solid black lines the equipotentials with the presence of FAC at t_2. The top cartoon refers to the time interval $t_2 = 8$ min – $t_1 = 4$ min, the middle one to the time interval $t_2 = 1$ hr – $t_1 = 20$ min and the region Y_{GSM} from 2 to -1 R_E and the bottom one to the time interval $t_2 = 1$ hr – $t_1 = 20$ min and the region Y_{GSM} from 5 to 2 R_E. All the above ionospheric quantities are projected to the equatorial plane.

2.4 Dependence of Harang reversal on plasma sheet conditions

As discussed in section 2.3, the physical processes that lead to the formation of the Harang reversal are strongly related to the different contributions from electrons and protons of different energies. Thus we next investigate how these physical processes are affected by the plasma sheet density and temperature, which vary significantly with the interplanetary conditions.

We have run the RCM, with the 16 different MLT-dependent plasma sheet boundary conditions listed in Table 2.2 for northward IMF (NIMF) and in Table 2.3 for southward IMF (SIMF) conditions. Except for the boundary conditions, all of these simulations were run the same as for the simulation described in the previous section, other than we now increase the potential drop gradually within an hour and not as a step function, and we decrease the Dst from -10 to -20 nT. Again we set t = 0 to be when the polar cap potential drop starts to increase. The boundary conditions in each run are kept time-independent. Note that although it is unrealistic to have plasma sheet corresponding to NIMF conditions when convection has been enhanced for 5 hr, the goal of this study is to investigate how the preconditioning of the plasma sheet prior to a convection enhancement affects the physical processes that lead to the formation of the Harang reversal.

For the 16 different boundary conditions, we have calculated the total number density, proton and electron total temperature, and proton total pressure from our phase space density function. These boundary values at dawn (light blue), dusk (black), and midnight (red) are shown in Figure 2.4. The numbers along the x-axis refer to the cases listed in Table 2.1 and the letters N and S refer to the NIMF and southward SIMF conditions respectively. The cases are ordered in this plot from less dense to more dense for both SIMF and NIMF. It can be seen that the plasma sheet under NIMF conditions is generally colder and denser than under SIMF conditions.

The bottom two panels of Figure 2.4 show that there is a correlation between the plasma sheet number density and plasma sheet pressure. It is known that plasma sheet pressure affects the evolution of the shielding of the convection electric field [*Garner et al.*, 2003] in the near Earth region. However, the shielding effect also depends on conductivity, which is related to the electron temperature. Therefore, both density and temperature contribute, in different ways, to the shielding effect. The shielding of the electric field controls whether the low energy protons will penetrate earthward enough so that the formation of the Harang reversal is possible. Among our 16 cases we pick two extreme ones, with different Harang reversal characteristics. The first one, in which the Harang reversal covers a very small region in MLT and latitude, is a cold and dense plasma sheet case, while the second one, in which the reversal extends to a much wider region both in MLT and latitude, is a hot and tenuous one. We investigate the reasons for this different behavior and then we show a more general correlation between the 16 plasma sheet conditions and the reversal's characteristics.

2.4.1 Cold and dense versus hot and tenuous plasma sheet: relation between shielding evolution and Harang reversal formation

2.4.1.1 Electric field, flow, FAC, and conductance in the vicinity of the Harang reversal

As mentioned above, to understand how the plasma sheet number density and temperature affect the overlap of FAC, and thus the Harang reversal, we compare the simulation results between cold and dense plasma sheet case 3 under N IMF conditions (3N) and hot and tenuous plasma sheet case 5 under S IMF conditions (5S).

Figure 2.5 shows ionospheric FAC projected to the equatorial plane and ionosphere, conductivity in the ionosphere, and pressure in the equatorial plane, for case 3N and 5S, at t = 5 hr. The Harang reversal in case 3N extends from 63^o latitude at 23:30 MLT to 62^o at 01:00 MLT, while in case 5S it extends substantially further equatorward and dawnward from the same latitudinal and longitudinal position (63^o at 23:30 MLT), reaching 58^o latitude at 3:00 MLT. The westward return flows associated with the Harang reversal in the premidnight sector, just equatorward of the region of high auroral conductance, is seen to be very strong for case 5S, since the electric field in that region is very strong, but weak for case 3N. How the Harang region and the return flows depend on the plasma sheet condition is discussed in section 2.4.2. It is also clear that the inner edge of Pedersen conductivity, which is actually the electron plasma sheet inner edge, is located at higher latitudes for case 3N than for case 5S.

The latitudinal profiles of ionospheric FAC, Pedersen conductance, and flux tube total content η of 30 eV protons (energy at boundary location: X = 20 R_E at midnight) are compared with the Harang reversal location at MLT = 00 hr for both cases in Figure 2.6. In the hot and tenuous plasma sheet case, the Harang reversal is located well equatorward of the peak of upward FAC and of the conductivity peak and very close to the boundary between the downward and upward FAC. On the other hand, for the cold and dense case the reversal is located almost at the upward FAC peak and the conductivity peak.

Our interpretation is that, in the 5S case, the shielding of the convection electric field is not effective. Thus low-energy protons penetrate further inward as can be seen by the η latitudinal profile. In fact, they are able to penetrate not only closer to the Earth than the high energy protons, which are responsible for the upward FAC peak in the overlap region (see section 2.3.1), but also closer than the high energy electrons that are responsible for the conductivity peak. This is why the downward current in the overlap region extends to lower latitudes (~58-60^o) where conductivity and upward FAC are very weak. Therefore, in the hot and tenuous case, the Harang reversal is located away from the upward FAC and conductivity peaks. The fact that the downward FAC is in the region of weak conductivity also explains the much stronger westward return flow (see discussion about SAPS in section 2.3.2) in the hot and tenuous case. The electric field perturbations induced by the downward current, being located in the low conductivity region, are very strong. Therefore, the total electric field is substantially increased, resulting in the enhancement of the **E**×**B** convection flow in this region.

On the other hand, the shielding in 3N case, when the plasma sheet is colder and denser, evolves quickly enough so that the low-energy protons remain further away from the Earth than in the 5S case. Thus the downward FAC of the overlap region remains at higher latitudes closer to the conductivity and upward FAC peaks and so does the Harang reversal.

In Figure 2.7 we show the latitudinal dependence of the same properties as in Figure 2.6 but at 03 MLT. We can see that for the hot and tenuous case there is still a weak electric field reversal attributed to the very small downward current caused by the penetration of the low-energy protons, while for the cold and dense case this penetration, and therefore the overlap of the downward FAC with the upward FAC, is not possible due to the strong shielding in this region.

Figure 2.8 shows equipotentials (solid black contours) and the η inner edge for protons (red curve) of the same energy channel (30 eV at the midnight tail boundary) at time t = 1:00, 1:30, 4:30 hr. These results confirm that, at all MLT, the low-energy protons in the 3N case cannot penetrate as close to the Earth as they do in the 5S one, because the shielding develops quicker in the cold and dense case than in the hot and tenuous one.

2.4.1.2 Effect of density and temperature on shielding

So far we have shown that penetration of the low energy protons in the near Earth region, and therefore the formation of the Harang reversal, strongly depends on the evolution of the shielding of the convection electric field. Since shielding is determined by two major factors, the FAC magnitude and the auroral conductivities, the next question is how the plasma sheet state affects these two factors.

Magnetic drift allows hotter particles to move more azimuthally than do colder particles. Therefore the plasma pressure in the hot and tenuous plasma sheet dominated by hotter particles is more azimuthally distributed than the pressure in the cold and dense plasma sheet dominated by colder particles. As a result, the azimuthal pressure gradients are larger in the cold and dense plasma sheet, creating larger total FAC strength in the near Earth region than in the hot and tenuous plasma sheet as shown in Figure 2.5. This is particularly true for the upward current region, which clearly can be seen to cover a larger region in the cold dense case. Furthermore, the region of enhanced auroral conductance, which is computed from the precipitating electron energy flux estimated from the simulated plasma sheet electron population in these RCM runs, remains restricted to higher latitudes in the cold and dense case, whereas the region is substantially broader and extends to lower latitudes (~60-62^{o}) in the hot and tenuous case. Lower FAC, which require weaker ionospheric currents to maintain current continuity than do higher FAC, and the broader region of higher conductivity means that less electric field perturbation (i.e., less shielding) is required in the hot and tenuous case. The reason for the difference in the conductivity profiles is in part due to the preconditioning, low-energy electrons being able to penetrate closer to the Earth for the hot and tenuous case than for the cold and dense case during the preceding period of weak convection.

We verify the point about the contribution of the conductivity to the shielding by doubling only the value of Pedersen conductivity for case 3N at t = 1:00 hr. This way, we keep the same magnitude of FAC at this time. Figure 2.9 shows FAC, conductivity, and magnitude of the electric field at 00 MLT at t= 1:00 hr versus distance from the Earth for cases 3N (red solid line) and 3N with double conductivity (dotted black line). It can be seen that, although the FACs are the same as expected, since we have not changed anything that would affect the pressure, the near Earth electric field increases dramatically in the latter case, that is, the shielding is weaker. This is because the electric field perturbations due to the FAC are of smaller magnitude in response to the much higher conductivity in this region.

Garner et al. [2003] also reached the conclusions that shielding is more efficient if the plasma sheet is colder or denser. However, in their numerical experiments with the RCM, they did not include the dependence of the shielding effect on auroral conductivity, since they used an empirical model of the Kp-dependent auroral precipitation by *Hardy et al.* [1985] to calculate the auroral conductivities, which does not depend on the plasma sheet condition.

2.4.2 Harang reversal latitudinal extent, MLT coverage, and westward return flow

Having determined the parameters that control the shielding of the convection electric field, and therefore the formation of the Harang reversal, we now proceed to our quantitative study of the Harang reversal characteristics.

In Figure 2.10 we plot the latitudinal and MLT extents, as well as the peak magnitude of the westward return flow at 23 MLT, of the Harang reversal for 14 of our cases (cases 2 and 4 for NIMF are excluded here because the Harang reversal was almost unidentifiably weak; this is due to the very high plasma sheet density and low electron temperature, and therefore the very strong shielding, for these two cases).

The Harang reversal in cases 1, 5 and 7 for both northward and southward IMF boundary conditions, which are cases of hot and tenuous plasma sheet, has larger latitudinal and longitudinal extent as well as larger peak westward return flow speed than in cases 3, 2, 4, 6 and 8 of colder and denser plasma sheet. These results agree with the physical explanation given in the previous sections about the correlation between plasma sheet conditions, the shielding effect, and the formation of the Harang reversal. In all of the cases, however, the poleward end of the Harang reversal is located around 63^{o} latitude and 23:30 hr MLT. This is because the poleward end of the Harang reversal depends only on the polar cap potential drop and not on the plasma sheet state. Note that observations show that the MLT of the westward end of the Harang reversal depends on the IMF By [*Rodger et al*. 1984], and the IMF By is known to affect the ionosphere convection pattern and the magnetic field in the magnetosphere. However, the present RCM assumes strict symmetry between the northern and southern ionospheres, and we use IMF By = 0 for the T96 magnetic field model. These restrictions do not allow us to investigate the IMF By effect on the westward-most MLT of the Harang reversal.

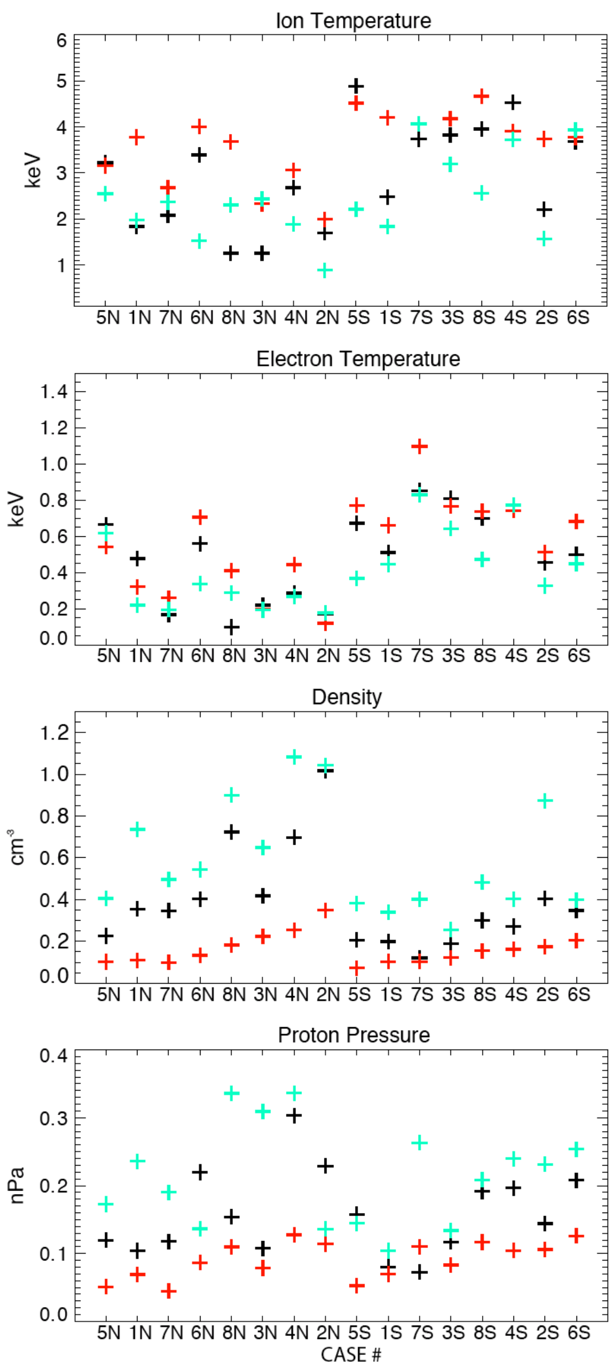

Figure 2.4 Ion and electron temperature, density and pressure at the outer boundary at MLT = 00 hr (red), MLT = 18 hr (black) and MLT = 06 hr (light blue), for each one of the 16 cases. The numbers refer to the cases of Table 2.1. The letter N (S) next to the number of each case corresponds to NIMF (SIMF) conditions.

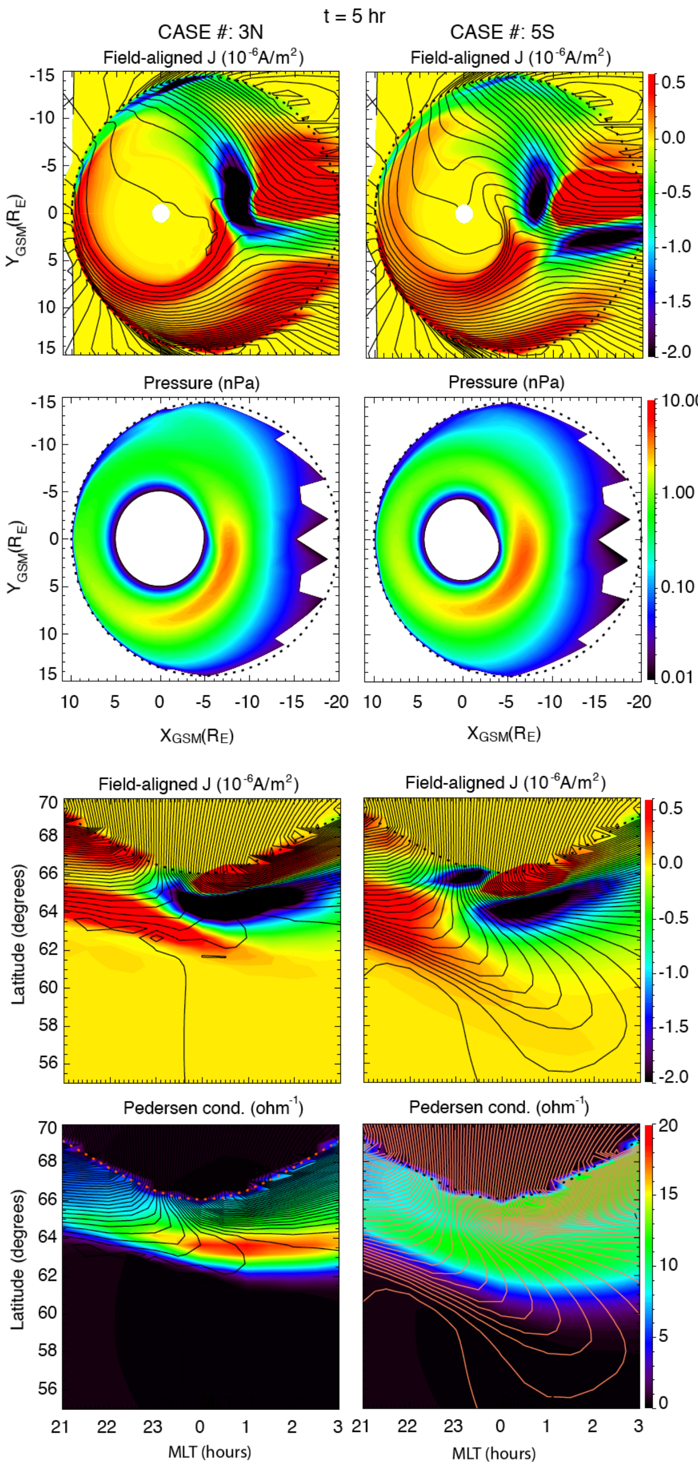

Figure 2.5 Ionospheric field aligned currents with equipotentials in the equatorial plane and in the ionosphere, pressure in the equatorial plane and Pedersen conductivity with equipotentials (1 kV interval) in ionosphere for the cases 3N and 5S.

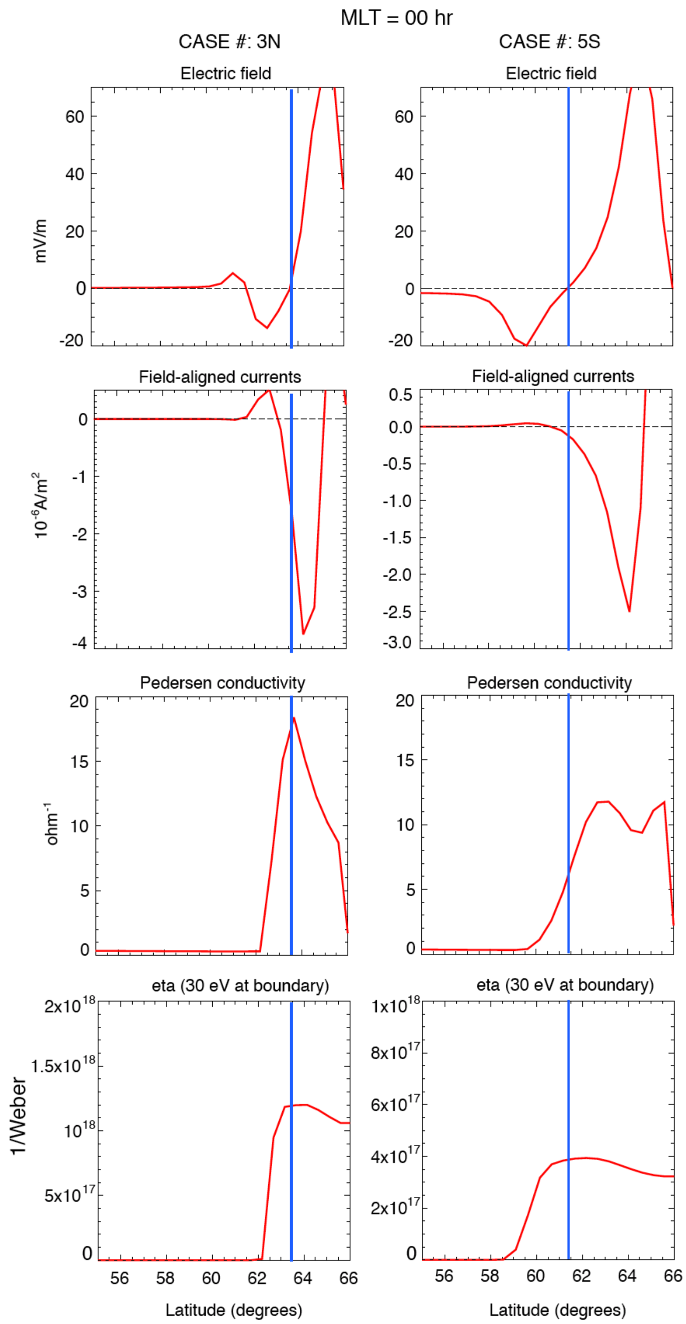

Figure 2.6 Latitudinal profiles of electric field, field aligned currents, Pedersen conductance and flux tube total content η of protons of energy 30 eV at the midnight tail boundary, at MLT = 00 hr, for the cases 3N and 5S. The blue line indicates the latitude where the Harang electric field reversal is located.

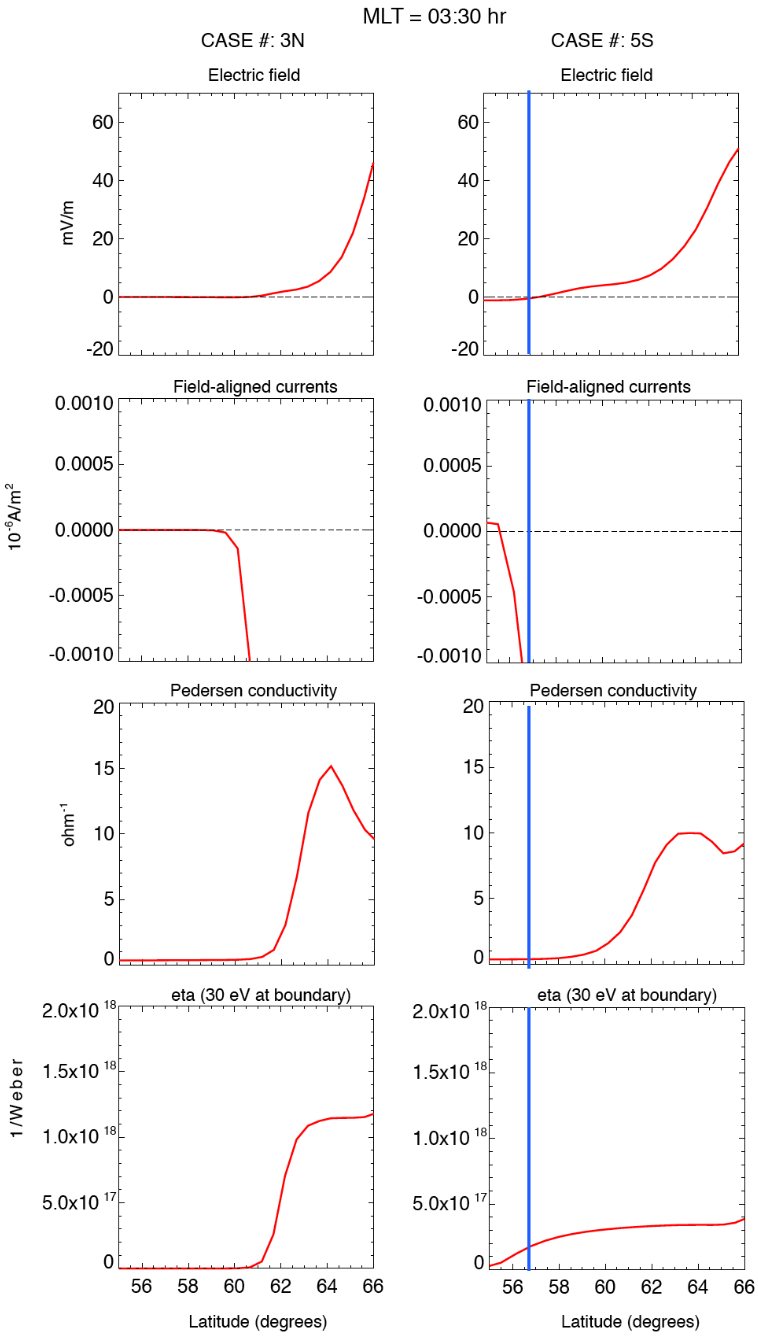

Figure 2.7 Same as Figure 2.6 but at MLT = 3:30 hr

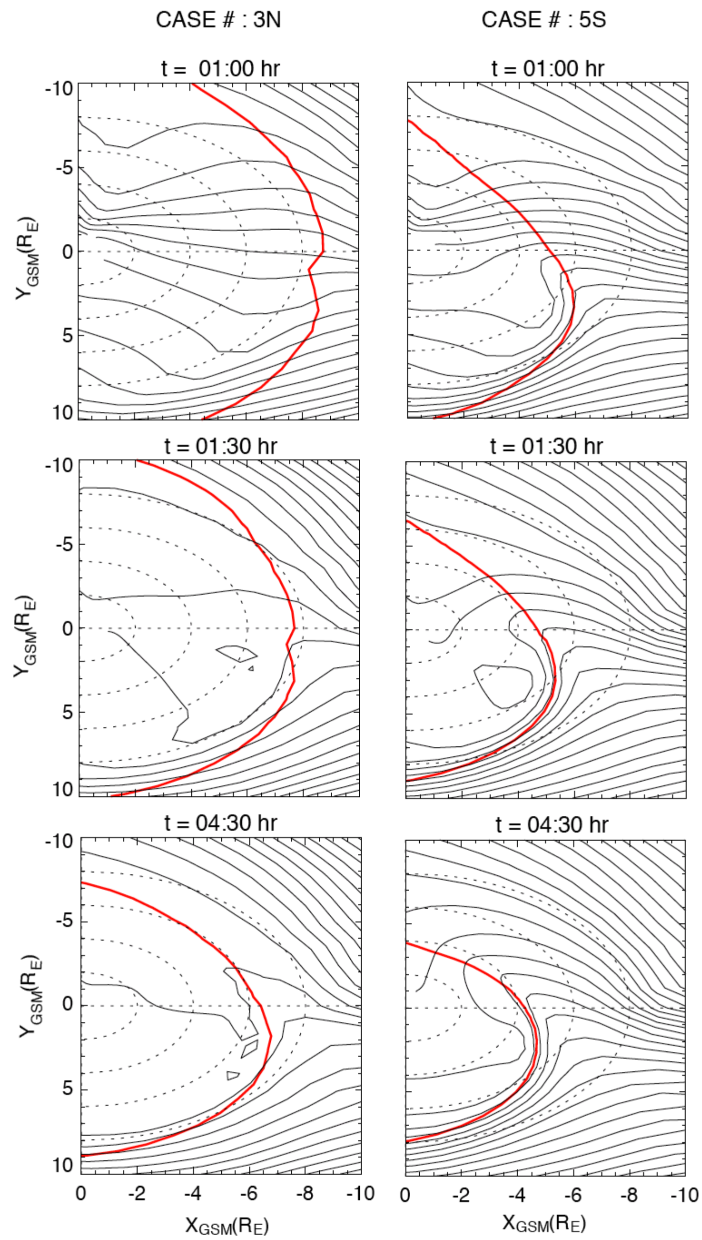

Figure 2.8 Equipotentials (black solid contours) and η inner edge (red curve) for 30 eV protons at the outer boundary at time t = 1, 1:30, 4:00 hr.

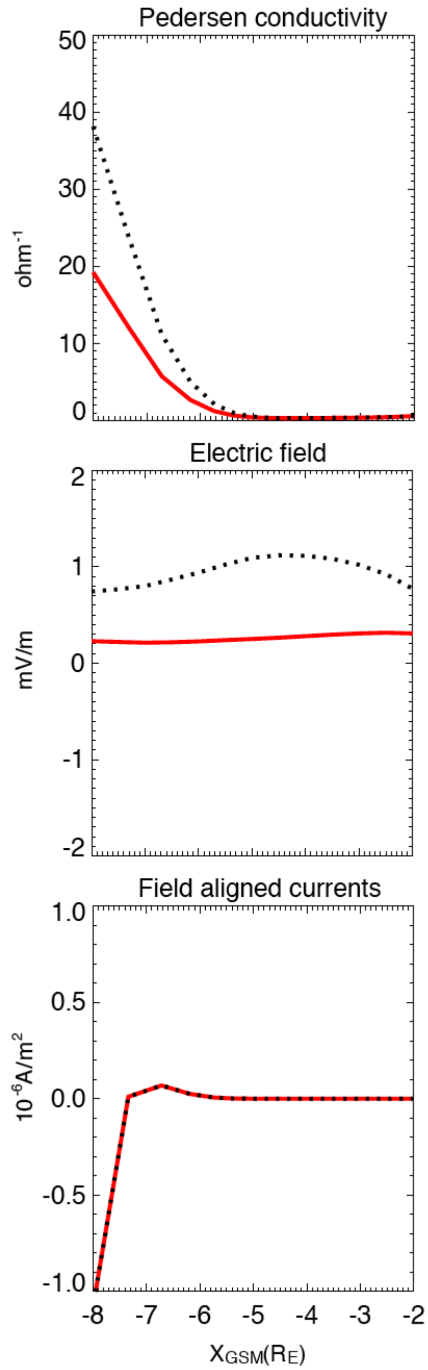

Figure 2.9 Pedersen conductivity, magnitude of the electric field, and ionospheric field aligned currents at MLT = 00 hr and time t = 1 hr, versus distance from the Earth for the cases 3N (red solid line) and 3N with double conductivity (black dotted line).

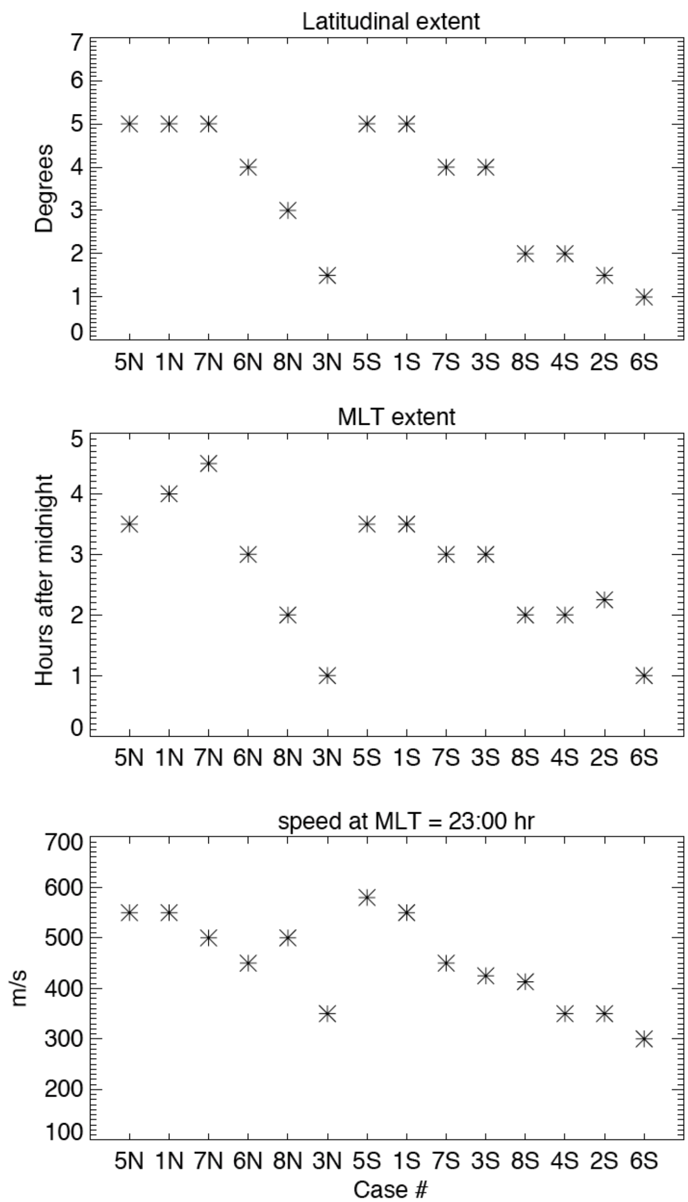

Figure 2.10 Latitudinal and MLT extent, and magnitude of the peak speed of the westward return flow of the Harang reversal for 14 of our cases.

2.5 Summary – Conclusions

In this chapter we have quantitatively evaluated the physical processes responsible for the Harang reversal and how these processes are affected by the plasma sheet density and temperature. We used the RCM with MLT-dependent plasma sheet boundary conditions that are a function of the interplanetary conditions based on 11 years of Geotail data.

First, we have found that the Harang reversal is a result of an overlap in MLT between the downward and upward Region-2 FAC. The upward FAC in the overlapping region is located at higher latitudes and is a result of the pressure peak contributed by the high-energy protons due to their duskward magnetic drift. The downward FAC, on the other hand, is located at lower latitudes and results from the pressure peak caused by the plasma sheet electrons and low-energy plasma sheet protons, which penetrate closer to the Earth at the midnight and postmidnight MLT than do the high energy protons. The earthward penetration of the low-energy protons into the near Earth region, which is crucial for the formation of the Harang reversal, strongly depends on the shielding of the convection electric field.

We found that the shielding is more efficient for a colder and denser plasma sheet, which is often found in the cases of higher solar wind density, than for a hotter and more tenuous plasma sheet found in the cases of lower solar wind density. A combination of higher pressure, and therefore stronger FAC in the near Earth region, and lower auroral conductance at low latitudes in the colder and denser plasma sheet, results in enhanced shielding of the penetration electric field. On the other hand, in the hot and tenuous case, the pressure and FAC magnitudes in the inner magnetosphere are lower and the conductivity is higher, therefore the shielding is weaker.

The above arguments lead us to the conclusion that in hot and tenuous plasma sheet conditions, when the shielding of the convection electric field is not efficient, the low-energy protons get much closer to the Earth than the high-energy protons and the high energy electrons. This way, the downward FAC in the overlapping region is located at lower latitudes, further equatorward from the upward FAC peak and the conductivity peak, and extends further towards postmidnight MLT. The location of the downward current in the region of weak conductivity also explains the much stronger SAPS for a hot and tenuous plasma sheet, since the electric field perturbations induced by the downward FAC are very strong, causing a substantial increase in the total electric field, thus an enhancement of the $\mathbf{E}\times\mathbf{B}$ convection flow in this region.

Therefore, in the cases of lower plasma sheet number density, the Harang reversal has larger latitudinal and MLT extent and stronger westward return flows (SAPS), than in the cases with higher plasma sheet number density.

CHAPTER 3 | Effect of self–consistent magnetic field on plasma sheet penetration to the inner magnetosphere

To determine the feedback of force-balanced magnetic field to the transport, we have integrated the Rice Convection Model (RCM) with a modified Dungey magnetic field solver to obtain the required force balance in the equatorial plane. Comparing our results with those from a RCM run using T96 magnetic field, we find that transport under force-balanced magnetic field results in weaker pressure gradients and thus weaker R2 FAC in the near Earth region and weaker shielding of the penetration electric field. As a result, plasma sheet protons and electrons penetrate further earthward and their inner edges become closer together and more azimuthally symmetric than in the T96 case. The Harang reversal extends further dawnward and the SAPS become more confined in radial and latitudinal extent. The magnitudes of azimuthal pressure gradient, the inner edges of thermal protons and electrons, the latitudinal range of the Harang reversal, and the radial and latitudinal width of the SAPS from the force-balanced run are found to be more consistent with observations. The results presented in this chapter are published in *Gkioulidou et al.* [2011].

3.1 Introduction

Plasma sheet particles moving towards the Earth under an enhanced convection electric field give rise to plasma pressure enhancements, which are associated with changes in magnetic field in maintaining force balance. The pressure changes cause changes in perpendicular current in the plasma sheet and eventually perpendicular current divergence, which requires a closure in the ionosphere through field-aligned currents (FAC). These FAC, referred to as the Region-2 (R2) FAC, are responsible for electrodynamical coupling between magnetosphere and ionosphere, and the FAC intensity is determined mainly by the azimuthal gradient of plasma pressures and the radial gradient of magnetic flux tube volumes [*Vasyliunas*, 1970]. In order to maintain current continuity in the ionosphere, the FAC lead to modification of the convection electric field in the ionosphere. The modified electric field maps back into the magnetosphere, which in turn affects the plasma sheet transport itself to the near-Earth region.

Using the Rice Convection Model (RCM) with non-force-balanced Tsyganenko 96 (T96) magnetic fields, we have previously investigated [*Gkioulidou et al.*, 2009] how the electrodynamic feedback to the transport through the R2 FAC is responsible for the formation of the Harang reversal and the Sub-Auroral Polarization Streams (SAPS), which have been found to be closely associated with substorms and storms [*Zou et al.*, 2009; *Bristol and Jensen,* 2007, *Nishimura et al.*, 2008; *Anderson et al.*, 2001]. Since plasma sheet transport and FAC are also strongly affected by the magnetic field, which is found to be distinctly different from dipole in the inner plasma sheet [*Cahill et al.*, 1966], feedback between the plasma transport and magnetic field is also essential to the R2 coupling. Therefore, in order to quantitatively determine inner magnetosphere plasma transport, it is necessary to self-consistently model plasma, electric and magnetic fields altogether.

In recent years there has been an ongoing effort in the community for modeling the self-consistent feedback between plasma and magnetic field in the magnetosphere. *Wang et al.*, [2003; 2004] created force-balanced magnetic fields for simulated plasma sheet plasma pressures around the midnight meridian by adding adjustable currents to the T96 magnetic fields. Using the Euler potentials method, *Zaharia et al.*, [2004] and *Zaharia* [2008] established a magnetic field model that can provide 3-D force-balanced magnetic fields with a given pressure distribution by numerically solving the force-balance equation. This model was later coupled with the Ring Current Atmosphere Interaction Model (RAM) (*Jordanova et al.*, [2010]) to obtain magnetic fields in force-balance with ring current pressures. Similarly, *Liu et al.,* [*2006*] developed a force-balanced magnetic field solver using Euler potentials method for a modified Dungey magnetic field. The solver has been coupled with a ring current model based on *Chen et al.*, [1994] to simulate transport of storm-time ring current ions under force-balanced magnetic field by numerically solving force-balance equation in the equatorial plane. These simulations showed that magnetic field becomes more stretched to balance increasing plasma pressure and results, in turn, in less earthward penetration of particles and lower near-Earth pressures. However, self-consistent electric field is not taken into account in the above models.

Self-consistent modeling of both electric and magnetic fields has been achieved by incorporating the RCM with a magnetic field relaxation technique developed by *Hesse and Birn* [1993] to simulate the near-Earth magnetosphere under enhanced convection [*Toffoletto et al.*, 1996, 2001; *Lemon et al.*, 2004; *Yang et al.*, 2010].

The objective of this study is, by self-consistently modeling plasma, electric and magnetic fields, to examine how the R2 coupling, and as a result the penetration of the plasma sheet into the inner magnetosphere, is affected by the self-consistent magnetic field. For this objective, we have substituted the non-force-balanced T96 magnetic field used in our previous RCM simulations [*Gkioulidou et al*., 2009] with force-balanced magnetic field provided by the modified Dungey force-balanced magnetic field solver mentioned above [*Liu et al*., 2006; *Schulz and Chen*, 2008] to achieve 2-D force-balance in the equatorial plane. The main reason for choosing this solver is its capability for efficient computation of magnetic field that exhibits the important features of magnetic local time (MLT) dependent field-line stretching, despite the tradeoff of being less accurate in its force balance in the z-direction than a 3-D force balance model. Additionally, the solver's scheme for solving the force balance equation is relatively stable numerically, so that the solver can easily find a solution. Another advantage of our coupled model is that we have included realistic MLT-dependent boundary particle conditions based on Geotail statistical data that are a mixture of a cold population coming from the flanks and a hot one coming from the tail. Different from other studies that have focused mainly on the effects of self-consistent magnetic field on storm-time ring current strength, we focus on how the feedback of magnetic field affects the R2 FAC and the penetration of the plasma sheet protons and electrons to the near Earth region, and how this eventually affects the structure of the convection electric field, including the Harang reversal and SAPS, in the inner magnetosphere.

The details of our coupled model, including the magnetic field solver, are described in section 2.2. In section 2.3.1 we show main features of the self-consistent magnetic field model and compare it with statistical THEMIS-Geotail observations. We then investigate the effect of the self-consistent magnetic fields on plasma pressure distributions in section 2.3.2, and on plasma sheet proton and electron inner edges in section 2.3.3. Based on the results of the sections 2.3.2 and 2.3.3, we explain in section 2.3.4 how the plasma sheet transport simulated in self-consistent magnetic field can affect the Harang reversal and SAPS. Comparisons are made with previous published observational results where feasible, and detailed comparison with observations of the spatial distributions of ion and electron populations from the mid-tail to inner magnetosphere is given in the paper by *Wang et al.* [2011] (hereafter referred to as Paper 2).

3.2 Model

3.2.1 Rice convection model

The RCM [*Toffoletto et al.*, 2003] calculates the bounce–averaged electric and magnetic drift of a flux tube filled with an isotropic distribution of ions or electrons under the assumption of slow flow approximation within a self-consistently computed electric field. The assumption of isotropy is reasonable, since, as can be seen in Figure 4 of Paper 2, plasma is quite isotropic in the plasma sheet. A detailed description of the model is given in section 2.2 of Chapter 2.

3.2.2 Plasma Boundary Conditions

The location of the outer boundary and the proton and electron distributions along the boundary are described in section 2.2.3. In this chapter we used the southward IMF boundary condition for $N_{SW} < 6.5$ cm^{-3}, $V_{SW} < 400$ km/s, $|B_{z\ IMF}| < 1.3$ nT (see Table 2.3).

3.2.3 Modified Dungey force-balanced magnetic field solver

In order to provide the RCM with self-consistent magnetic fields, we use a force-balance solver [*Liu et al.*, 2006; *Schulz and Chen*, 2007] to obtain magnetic fields that are in force balance with given plasma pressures in the equatorial plane. When in equilibrium, magnetic field and plasma pressure satisfy the force balance equation:

$$\mathbf{J} \times \mathbf{B} = \nabla P \tag{3.1}$$

where P is the isotropic pressure, and $\mathbf{B}$ is magnetic field and $\mathbf{J} = \nabla\times\mathbf{B}/\mu_o$ is current density.

The magnetic field $\mathbf{B}$ can be expressed in terms of two Euler potentials [*Stern*, 1967] as

$$\mathbf{B} = \nabla\alpha \times \nabla\varphi \tag{3.2}$$

where

$$\alpha = \partial\Phi_E / \partial\varphi = -\mu_E / L \tag{3.3}$$

is the magnetic flux per unit magnetic local time (MLT), Φ_B is the magnetic flux, φ is MLT, μ_E is the geomagnetic dipole moment, and L is the dimensionless label of the field line.

In our solver we make two important assumptions:

The first assumption is the fact that our second Euler potential is the azimuthal angle φ. This means that each magnetic field line always lie in the same meridian plane. Therefore, our solver does not account for azimuthal perturbations of the magnetic field. Observations inside r = 8 R_E [*Le et al.*, 2004] indicate the perturbations from FAC are too small to result in substantial bending, and magnetic field from the T96 also indicate strong field lines bending only occurs in regions very close to the magnetopause.

The second assumption is that the field lines satisfy the Dungey field line function:

$$L = r\left[\left(1 + \frac{r^3}{2b^3}\right)\sin^2\theta\right]^{-1} = r_0\left[\left(1 + \frac{r_0^3}{2b^3}\right)\right]^{-1} \tag{3.4}$$

where θ is magnetic colatitude and r_0 is radial distance from the point dipole at the equator in R_E, The parameter b represents field line stretching, and it is a function of both radial distance and MLT but remains constant along each field line. We should note here that the original Dungey model [*Dungey*, 1963] assumes a dipolar **B** field plus a uniform "southward" perturbation **ΔB** parallel to the magnetic dipole axis, that is, the stretching parameter b is constant and the model is current-free. Our solver allows b to vary from field line to field line to accommodate current, and is thus able to produce the required **J×B** to balance the pressure gradient force. For the rest of this chapter we refer to our solver as the modified Dungey solver.

With the first assumption, **B** can be expressed in spherical coordinates as a function of the partial derivative of α with respect only to geocentric radial distance r and colatitude θ

$$\mathbf{B}(r,\theta) = \nabla\alpha \times \nabla\varphi = \hat{r}\frac{\partial\alpha/\partial\theta}{r^2\sin\theta} - \hat{\theta}\frac{\partial\alpha/\partial r}{r\sin\theta} \tag{3.5}$$

which means that the curl of $\mathbf{B}(r,\theta)$ can be expressed as

$$\nabla\times\mathbf{B} = \hat{r}\frac{\partial^2\alpha/\partial r\partial\varphi}{r^2\sin^2\theta} + \hat{\theta}\frac{\partial^2\alpha/\partial\theta\partial\varphi}{r^3\sin^2\theta} - \frac{1}{r}\hat{\varphi}\left[\frac{\partial^2\alpha/\partial^2 r}{\sin\theta} + \frac{1}{r^2}\frac{\partial}{\partial\theta}\left(\frac{\partial\alpha/\partial\theta}{\sin\theta}\right)\right] \tag{3.6}$$

With the second assumption of using the Dungey field line equation (3.4), all the partial derivatives of α on the right-hand side of (3.6) can be converted into partial derivatives of α with respect to r_0 only at the equator, so that azimuthal current density at the equator becomes

$$\frac{\left[(\nabla\times\mathbf{B})_\varphi\right]_0}{\mu_0} = -\hat{\varphi}\frac{1}{r_0\mu_0}\left[\frac{\partial^2\alpha}{\partial r_0^2} - \frac{2\alpha}{3\mu_E + 2r_0\alpha}\frac{\partial\alpha}{\partial r_0}\right] \tag{3.7}$$

where the subscript "0" refers to quantities at the equatorial plane.

Therefore, given the above two assumptions, the 3-D force balance equation (3.1) is reduced to a 2-D problem that requires solving two ordinary differential equations, the radial and azimuthal components of force balance in the equatorial plane:

$$-\frac{[(\nabla\times\mathbf{B})_\varphi]_0}{\mu_0}B_0 = \frac{\partial P_{\perp 0}}{\partial r_0} \tag{3.8}$$

$$\frac{[(\nabla\times\mathbf{B})_r]_0}{\mu_0}B_0 = \frac{1}{r_0}\frac{\partial P_{\perp 0}}{\partial\varphi} \tag{3.9}$$

The azimuthal component has an analytical solution, namely,

$$\frac{B_0^2}{2\mu_0} + P_0 = P_{total}(r_0) \tag{3.10}$$

Equation (3.10) actually implies that the sum of magnetic and plasma perpendicular pressure in the equatorial plane is the same along the same radial distance circle.

Combining equations (3.3) and (3.7), the radial component of the force balance equation (3.8) becomes a second order ordinary non-linear differential equation in $1/L$ with respect to r_0, namely,

$$\frac{\partial^2(1/L)}{\partial r_0^2} = \left(-\frac{2}{\mu_0 P_{norm}(3L-2r_0)} - \frac{\partial \ln P_{norm}}{\partial r_0} + \frac{2}{r_0}\right)\left(\frac{\mu_0 P_{norm}}{1+2\mu_0 P_{norm}}\right)\frac{\partial(1/L)}{\partial r_0} \tag{3.11}$$

where $P_{norm} = P_0/B_0^2$ and B_0 is the magnetic field at the equator. Therefore, for a given plasma pressure distribution in the equatorial plane, force balanced magnetic field can be obtained by numerically solving equation (3.11) with boundary conditions for $1/L$, and $\partial(1/L)/\partial r_0$ specified at 2 R_E, which is our inner boundary, satisfying at the same time the condition of equation (3.10) for the same radial distance. The fact that the stretching parameter b does not appear in the equations (3.10) and (3.11) is because we have explicitly used the Dungey field line equation (3.4), and thus b, to express all the partial derivatives of $1/L(r,\theta)$ at the equator only as partial derivatives of $1/L$ with respect to r_0. To compute the flux tube volume which is used in the bounce-averaged equation of particle motion as well as in field-aligned current (FAC) calculation in the RCM, we use equation (21) in *Schulz and Chen*, [2007] and that equation's two required inputs, $b(r_0,\varphi)$ and $\partial b/\partial r_0$, can be simply obtained with equation (3.4).

3.2.4 The RCM with Self-Consistent Magnetic Field

By combining the RCM with the modified Dungey solver, we can conduct simulations under both self-consistent electric and magnetic fields. For this study, we ran the self-consistent simulation first with constant cross polar-cap potential drop ($\Delta\Phi_{PC}$) of 30 kV for 5 simulation hours (t = 5 hr), and then gradually, within an hour, increased $\Delta\Phi_{PC}$ to 90 kV (t = 6 hr) and kept it constant for another 4 hours (t = 10 hr). Figure 3.1 shows a schematic diagram of the time dependent $\Delta\Phi_{PC}$ change in our run. Every 10 minutes the magnetic field was updated so that it maintains force balance with the RCM pressures at all time. The plasma boundary condition that was described in section 2.2 remains constant throughout the simulation. For the two magnetic field boundary conditions, $1/L$ and $\partial(1/L)/\partial r_0$ at 2 R_E, we used dipole values for $1/L$ at all MLT but adjusted $\partial(1/L)/\partial r_0$ at each MLT to achieve the best overall force balance both radially and azimuthally.

There are some limitations in our current coupled model. The force balance is calculated only in the equatorial plane, thus balance in the off-equatorial region is not achieved perfectly. Since b is constant along each field line, the magnetic field lines are constrained to a "Dungey field line" shape. Also, no outer boundary conditions for the magnetic field solver are specified to include the effect of the magnetopause. Despite the above limitations, the modified Dungey solver is capable of describing the important features of field-line stretching according to equatorial pressure profiles and the fields can be numerically computed rather efficiently. Therefore, the coupled RCM-modified Dungey solver model allows us to more accurately evaluate how the self-consistent feedback between plasma and magnetic field affects the electromagnetic coupling between the magnetosphere and ionosphere that is crucial to the penetration of the plasma sheet into the inner magnetosphere.

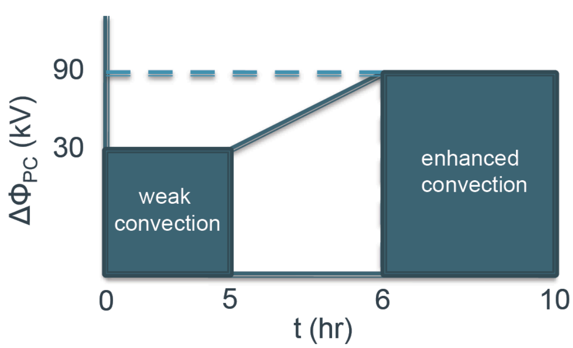

Figure 3.1 Schematic diagram illustrating the polar cap potential drop ($\Delta\Phi_{PC}$) change with time in our simulation runs.

3.3 Simulation results

3.3.1 Self-consistent magnetic field

First of all, we checked that our magnetic field is indeed in force balance with the plasma pressure at a given time. In Figure 3.2 we have plotted $|\mathbf{J}\mathrm{x}\mathbf{B}|$ (black solid line), $|\nabla P|$ (red solid line) and the absolute value of their difference (black dashed line) versus radial distance at the equator along the midnight meridian, at t = 10 hr, that is, 4 hr after $\Delta\Phi_{PC}$ was increased to 90kV. Apart from the region $-2 < X_{GSM} < -3$, where there is no plasma pressure because particles from the boundary cannot reach that region, the difference between the two forces throughout the simulation domain is clearly negligible comparable to the two forces, indicating that we have achieved satisfactory force balance.

In Figure 3.3 we show the magnetic field lines at midnight, also at t = 10 hr. The modified Dungey field lines are shown with solid lines while the corresponding dipole field lines are shown with dashed lines. Different colors correspond to different L-shells. We can clearly see the Dungey field line shape mentioned above, but also the stretching of the field lines in comparison to the dipole ones.

In order to show the amount of stretching of the field lines, in Figure 3.4 we have plotted the radial profile of L-shell at the equator at midnight for t = 5 hr (purple), t = 6 hr (light blue) and t = 10 hr (green). Going from weak (30kV) to enhanced convection (90kV), we see more stretching in the inner magnetosphere (lower L-shells for the same radial distance) but less stretching towards the tail. In the regions earthward (tailward) of the peak of the duskward cross-tail current, the perturbation of the magnetic field caused by this the current is negative (positive). Therefore, as the duskward current increases with increasing convection, magnetic field gets more (less) stretched in the inner (outer) magnetosphere.

One of the major advantages of using a self-consistent magnetic field model is its ability to produce a dawn-dusk asymmetric magnetic field according to the plasma pressure gradients, which, as is discussed later, plays an important role in magnetosphere-ionosphere coupling. Figure 3.5 shows the equatorial profiles of plasma pressure, B_z, and L-shell along the dawn (yellow line) and dusk (purple line) meridians at t = 6 hr (convection just reached 90kV). The dipole field (the black dashed line) is also plotted as a reference. At dusk, where the pressure is higher than at dawn, the magnetic field lines are more stretched and B_z is smaller in the inner magnetosphere.

To investigate if the above changes with increasing convection seen in our self-consistent (SC) magnetic field configuration are reasonable, we compare them with statistical values of magnetic field from Geotail and THEMIS. In Figure 3.6 we plot radial profiles of $V^{-2/3}$ (top panels) and B_z (bottom panels) at midnight for our SC magnetic field (red line), and for the data (black line corresponds to the median, while the minimum and maximum of the error bar indicate the 25% and 75% percentiles respectively). The simulations results are for t = 5 hr, that is, under weak convection of 30 kV, on the left, and for t = 6 hr, that is, right after convection has reached 90 kV, on the right. The Geotail and THEMIS data have been sorted out into 2 different convection levels with low AE values: (1) weak convection: $20 < \Delta\Phi_{PC} < 40$ kV, $10 < AE < 50$ nT, and (2) strong convection: $50 < \Delta\Phi_{PC} < 100$ kV, $50 < AE < 150$ nT. We included the additional criteria based on AE, indicated above, to minimize effects from the substorm expansion phase. We would like to point out that the model comparison with observations is not rigorous since the temporal variation of the convection and particle conditions for our simulation is rather simple compared with the more complicated conditions that correspond to the statistical results. Therefore, here we focus more on whether our self-consistent magnetic field model can reproduce the trends of the changes seen in the data. We can see that, the $V^{-2/3}$ of the SC run has in general good agreement with observations, although the modeled values are highter than the observed ones from r ~8 to 15 R_E. Note that $V^{-2/3}$ is the parameter related to the magnetic field that is actually used in the RCM calculations of bounce-averaged drift and FAC. The method of obtaining V from observations is discussed in Paper 2. The comparison of B_z with observations, on the other hand, is not as good. Our self-consistent B_z has, in general, larger values than the observed one. The discrepancy between observed and modeled values of both B_z and $V^{-2/3}$ has partially to do with the fact that we do not consider force balance in the z direction, due to our restriction to the Dungey field line shape, which limits the degree of stretching that is attainable. In addition, concerning the B_z values, the spacecraft measurements, as opposed to the simulated ones, were taken in the vicinity of the equatorial plane, not exactly at the center of the current sheet (where B_x and B_y are zero). The limitation to the stretching would mean that our mapping to magnetosphere might not be exact. However, the self-consistent B_z exhibits a slight increase towards the tail with enhanced convection (dashed lines indicate B_z = 10 nT for reference), which is consistent with the observational trend. This is also due to the different effect on the stretching of the magnetic field earthward and tailward of the duskward current's peak, as discussed earlier (see description of Figure 3.4).

3.3.2 Effect of the self-consistent magnetic field on plasma pressure distributions

As pressure evolves as a result of particle transport, magnetic field also changes to maintain force balance, which directly changes magnetic drift transport as well as FAC. The changing FAC modifies electric drift through coupling with the ionosphere, which changes particle transport in turn. To investigate how the feedback from magnetic field affects the plasma sheet dynamics and the resulting plasma and field distributions, we compare our current SC RCM runs with force-balanced magnetic field with results from our previous simulations [*Gkioulidou* et al., 2009] under specified non-force-balanced, dawn-dusk symmetric Tsyganenko 96 (T96) [*Tsyganenko*, 1995; 1996] magnetic field. All the setup for $\Delta\Phi_{PC}$ and boundary conditions in the two runs are exactly the same; the only difference is the magnetic field. To get the T96 magnetic field values, as in *Gkioulidou* et al., 2009, we decrease the IMF B_z from 0 to -7 nT and Dst from -10 nT to -11 nT when the $\Delta\Phi_{PC}$ increases from 30kV to 90kV (IMF B_z and D_{st} are used as an input for the T96), and two other inputs, Pdyn = 1.7 nPa and IMF B_y = 0, for the T96, are kept constant throughout the simulation. Since the T96 magnetic field is not in force balance with the simulated plasma pressure, we chose the above values for the T96 parameters in order to give typical magnetic field configurations for weak and for enhanced convection conditions. The relationship between IMF B_z reduction and $\Delta\Phi_{PC}$ drop change is based on equation 6 of *Weimer* [1995]. We decrease Dst only by 1nT because the ring current developed in our simulation, even after 5 hours, is not strong enough to justify a significant drop on the Dst index (note that we have not used initial plasma conditions that would account for a pre-existing ring current in the inner magnetosphere, so that we can purely investigate the plasma sheet transport from the boundary all the way to the inner magnetosphere).

In Figure 3.7 we show FAC and pressure profiles mapped to the equatorial plane (top four panels) as well as FAC and Pedersen conductivity profiles in the ionosphere (bottom four panels) at t = 10 hr, that is, 4 hours after constant 90 kV enhanced convection, under self-consistent (on the left) and under T96 (on the right) magnetic fields. The reason we show the above properties for t = 10 hr is that, by that time, the changes in our simulation results are insignificant which means that our simulation has essentially reached equilibrium. The line contours in all the plots are equipotentials. We also plotted electric field vectors (black arrows) at the equatorial plane in the night-side region on top of the FAC profiles.

We see that, in the SC run, compared to the T96 run, we have lower pressure in the inner magnetosphere and weaker dawn-dusk pressure asymmetry. Figure 3.8 shows azimuthal pressure profiles (top panel) and pressure gradients (middle panel) at r_0 = 9-12 R_E under weak convection (t = 5 hr) from the two simulation runs. The pressure gradients from the SC results are mainly duskward gradients (negative values); The T96 results, on the other hand, have a pressure peak near midnight MLT, thus resulting in duskward (dawnward) gradients at the postmidnight (premidnight) MLT. Using pressures simultaneously measured by two THEMIS spacecraft that were at the same radial distance but slightly separated in MLT, *Xing et al.*, [2009] showed that the azimuthal pressure gradients are mainly duskward at the nightside MLT with smaller magnitudes at the premidnight than postmidnight MLT, which is consistent with the SC results. Note that, by applying recent more accurate calibration of the THEMIS SST pressure, *Xing et al.* (X. Xing, personal communication, 2011) found that the magnitudes of the pressure gradients are actually about half of the magnitudes shown in the Figure 3 of *Xing et al.* [2009], which brings the comparison with the SC results to better agreement. Additionally, Figure 3.8 (bottom panel) shows observed statistical equatorial azimuthal pressure profiles at the same radial distances under weak convection obtained from the analysis of THEMIS-Geotail observations in Paper 2. The statistical profiles also indicate relatively weak azimuthal gradients as seen in the SC results and no prominent pressure peak around midnight as seen in the T96 results.

The effect of weaker azimuthal pressure gradients from the SC on the FAC and electric field distributions can be seen in Figure 3.7. The weaker azimuthal pressure gradients result in weaker R2 FAC (the pair of FAC at X ~ –5 to –10 R_E with downward FAC (in red) in the premidnight and upward FAC (in blue) in the postmidnight sector). The change in the R2 FAC modifies, in turn, electric field distributions through M-I coupling. We found that electric field becomes more dawn-dusk asymmetric under self-consistent magnetic field, with stronger electric field in the postmidnight sector than the premidnight one in the region beyond $X_{GSM} \sim -6\ R_E$. Also, the radial and latitudinal extent of the strong electric fields in the near-Earth premidnight sector (latitude ~65^o in the ionosphere and $X_{GSM} \sim -4\ R_E$ in the magnetosphere), also known as Subauroral Polarization Streams (SAPS) because of their strong westward **E**x**B** convection flow, become much more confined in latitudinal and radial extent than in the T96 run. The Harang reversal, the region of converging electric fields in the nightside ionosphere at auroral latitudes (60^o - 66^o), extends further towards dawn in the SC results.

In the next section we analyze in depth how particle transport under SC magnetic field results in the above different FAC and electric field distributions from those under fixed magnetic fields.

3.3.3 Effect of self-consistent magnetic field on plasma sheet protons and electrons inner edge

An important yet fundamental question arising from the above investigation of the plasma sheet properties is, how does applying a force-balanced magnetic field modify the plasma sheet particle transport to the inner magnetosphere relative to applying a non force-balanced magnetic field (namely T96)?

Figure 3.9 shows plasma sheet properties in the equatorial plane at t = 6 hr (just after $\Delta\Phi_{PC}$ has increased to 90 kV), with the SC run on the left and T96 run on the right. In all the panels, a thick dotted line gives a circle at r =10 R_E circle for reference. Figure 3.9(a) shows magnetic drift velocities (black arrows) for thermal plasma sheet protons (5 keV at 20 R_E at midnight, ~100 keV at 6.6 R_E), pressure profile (color contours) and equipotentials (black lines). As we can see, compared to the T96 run, using SC magnetic field results in weaker duskward magnetic drift for this thermal plasma sheet population, which is the main contributor to plasma pressure, thus leading to weaker azimuthal pressure gradient in the inner magnetosphere. The arrows in Figure 3.9(b) show the directions of ∇P and of ∇V, their magnitude being given by the arrow color. While in both runs ∇V is mainly in the radial direction, ∇P is also seen to be directed mainly radially only in the SC run (for the postmidnight region X ~ -8 to -10 R_E). Note that this is in agreement with results of *Zaharia* [2008] where he showed that, in a force-balanced magnetic field, the maximum angle between the pressure gradient and the field line curvature decreases with increasing plasma $\beta_0 = 2P_0/B_0^2$, that is, ∇P and ∇V become more aligned (antiparallel). As a result, the R2 FAC (color contours in Figure 3.9(c)), which depend on the cross product of pressure gradients and flux tube volume gradients, (see equation 2.4), are much weaker in the SC run and thus less efficient electric field shielding occurs in the near Earth region, especially in the postmidnight sector, where the upward FAC is significantly weaker than in the T96 run, as can be seen by the equipotentials (black contour lines in Figure 3.9(c)).

Finally, Figure 3.9(d) shows electric drift with orange arrows (drift due to induced electric field is neglected), as well as thermal protons' magnetic drift with blue arrows, trajectories beyond 5 R_E with black lines, partial pressure with grey-scale contour and inner edge with the red line (earthward of this red line the particle content, η, is less than 20% of the boundary value at midnight). Thermal protons' energy is the same as Figure 3.9(a). In the postmidnight sector, in the SC run, the plasma sheet protons are affected more by electric drift than in the T96 run, and, therefore, they penetrate further earthward. The change in particle transport also changes particle distributions, as can be seen from the inner edge of thermal protons becoming more aligned with the radial circle. That inner edge is also well correlated with the inner edge of the partial pressure profile of the same energy protons. As a result of this postmidnight earthward penetration, the inner edge of the plasma sheet thermal protons is more dawn-dusk symmetric in the SC run, as compared to the much more pronounced dawn-dusk asymmetry in the T96 run.

Given the above understanding of how different plasma sheet proton inner edges are obtained using SC magnetic field versus T96, we now investigate how the relative locations of plasma sheet protons' and electrons' inner edges are affected by the self-consistent magnetic field.

Figure 3.10 shows equatorial inner edges of particle content for plasma sheet thermal energies (same as in Figure 3.9) protons (red line) and electrons (blue line) for the two runs under weak and enhanced convection. Circles at 8 R_E and 10 R_E are shown for reference. The comparisons show that the inner edges of protons and electrons in the SC run are closer to each other and more azimuthally symmetric than in the T96 run. Comparing weak convection with enhanced convection, the inner edges of both protons and electrons in the SC run become more azimuthally symmetric with increasing convection and become even closer to each other. Also, the intersection of the ion and electron edges moves duskward with enhanced convection. The inner edges in the SC run is in better agreement than in the T96 run with those seen in statistical particle distributions shown in Figure 7 of Paper 2. The locations of the inner edges and relative position between ion and electron edges play important roles in determining the characteristics of the Harang reversal and the SAPS.

3.3.4 Effect of self-consistent magnetic fields on the Harang reversal and SAPS region

The earthward penetration of the plasma sheet strongly affects the spatial distribution of convection electric field in the near-Earth region, including the Harang reversal and the SAPS. In the recent years there has been a revival of the interest in these features since they seem to be closely associated with the two major geomagnetic disturbances, storms and substorms.

As can be seen in Figure 3.7, the Harang reversal in our SC simulation under enhanced convection extends from ~66^o to 60^o latitudes. This is in agreement with the ionospheric SuperDARN observations by *Zou et al.* [2009], who found the latitudinal extent of Harang reversal during the growth phase of nine substorms varied between 67.5^o and 62.5^o.

The ionospheric feature of the Harang reversal has been referred to as electric field skewing when mapped to magnetosphere. Observational evidence of this skewing has been shown in a paper by *Matsui et al.*, [2010]. By statistically analyzing Cluster data, they found changes in the sign of the x component of the electric field in the postmidnight sector between the main and recovery phases of storms, which is likely due to the bending of the equipotentials in the Harang region. Their electric field measurements are made at r = 3.5-6 R_E, which is within the radial distances of our simulated Harang reversal in the equatorial plane, especially in the postmidnight region.

Additionally, postmidnight storm-time enhancement of ions of tens of keV observed by ENA [*Brandt et al.*, 2002] has been associated with the above described electric field skewing [*Ebihara and Fok*, 2004; *Buzulukova et al.*, 2010]. Therefore, it is important to understand how this skewing in the Harang region is affected by the SC magnetic field, and more specifically why the Harang in the SC run extends more towards dawn, something that would definitely affect the above postmidnight ion enhancements.

In our previous study using the RCM simulations with T96 magnetic field model [*Gkioulidou et al.*, 2009], we have shown that the formation of the Harang reversal is a result of an overlap in the vicinity of midnight MLT of the R2 upward and downward FAC. In that overlap region, the downward FAC (located at lower latitudes) is associated with partial pressure peak of low energy protons (~up to 400 eV at the midnight boundary) that penetrate closer to the Earth towards the dawn side, while the upward FAC (located at higher latitudes) is associated with the dusk-side bulk pressure peak of high-energy protons. Combining this understanding from our previous results, our current SC results, we can explain why the Harang reversal extends more towards dawn than in the SC run than in the T96 run. In Figure 3.11 we plot trajectories with black contours and inner edge with red line for low-energy protons (400 eV at 20 R_E at midnight). It is clear that these low-energy protons, responsible for the downward FAC in the overlap region, penetrate closer to the Earth in the postmidnight sector in the SC run than in the T96 run, due to the reasons discussed in the previous section, that is, weaker shielding of the convection electric field. This means that the FAC overlap region extends more towards dawn and so does the Harang reversal, as can be clearly seen in Figure 3.7.

The second phenomenon associated with the convection electric field is SAPS, which refers to the region of very strong tailward electric fields in the near- Earth premidnight sector. These strong SAPS electric fields are a result of ions penetrating to a region earthward of electrons where conductivity is low, so that a strongly enhanced electric field is required to maintain current continuity with the enhanced downward FAC in that region [*Southwood and Wolf*, 1978, *Anderson et al.*, 2001]. Therefore, the fact that the SAPS in the SC run (X_{GSM} ~ -5 R_E in the magnetosphere) is more confined in its radial (equatorial plane) and latitudinal (ionosphere) extent can be attributed to the premidnight inner edges of protons and electrons being located closer to each other than in the T96 run. The narrow latitudinal (1^o-2^o) and radial extend of the simulated SAPS in the SC run is also in better agreement with the observations both in the ionosphere, 64^o-68^o [*Wang et al.*, 2011], and in magnetosphere ($< 1R_E$) [*Nishimura et al.*, 2008].

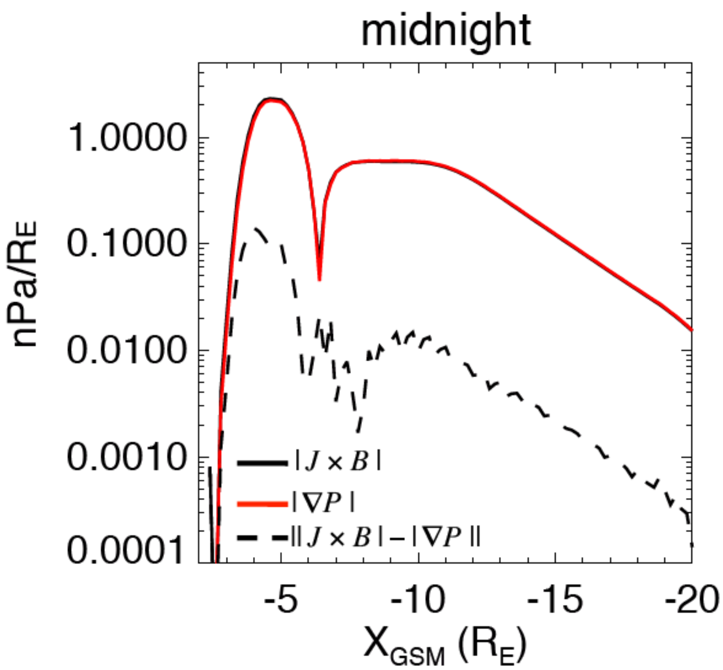

Figure 3.2 Radial profile along the midnight axis of |**J**x**B**| (black solid line), |∇*P*| (red solid line) and ||**J**x**B**|-|∇*P*|| (black dashed line) at t = 10 hr.

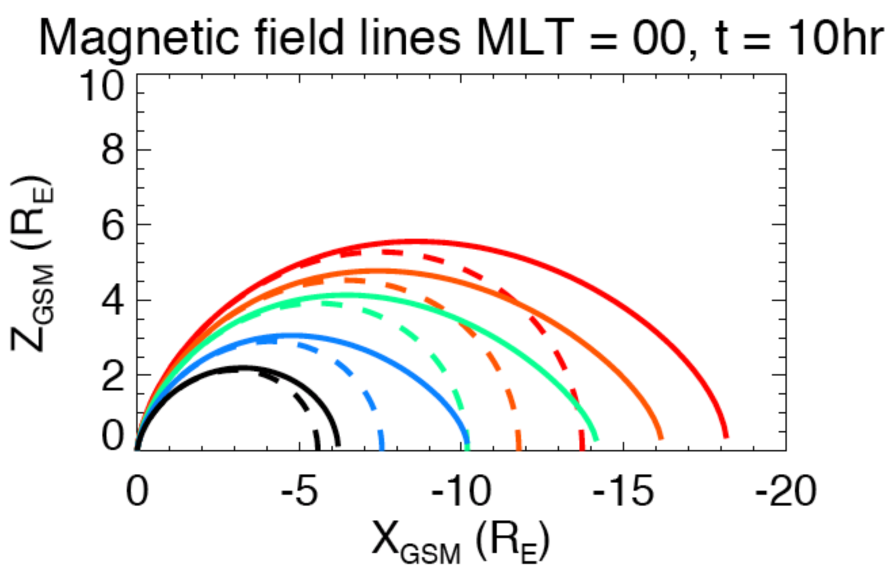

Figure 3.3 Magnetic field lines for dipole (dashed lines) and modified Dungey (solid lines) magnetic field model at midnight for t = 10 hr. Different colors represent different L-shells.

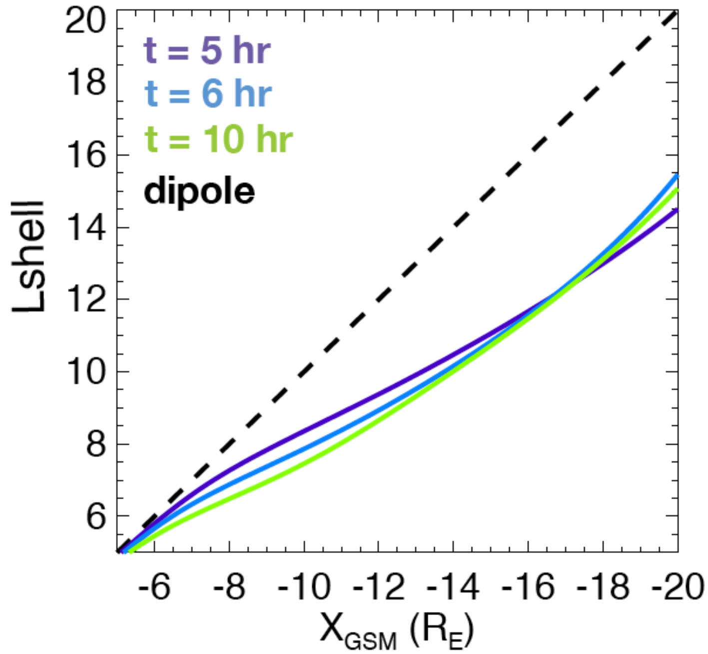

Figure 3.4 Radial profile of L-shell at the equator at midnight for t = 5 hr (purple), t = 6 hr (light blue) and t = 10 hr (green).

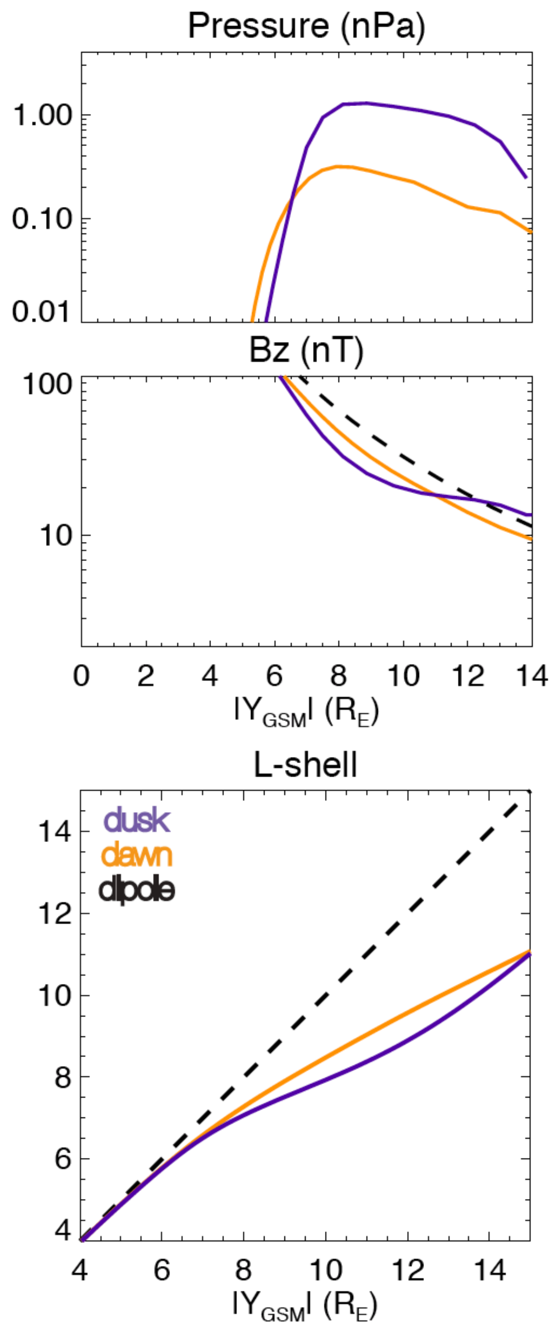

Figure 3.5 Equatorial profiles of plasma pressure, Bz and L-shell along the dawn (orange solid line) and dusk (purple solid line) meridians at t = 6 hr under enhanced convection (90kV). Dipole field (black dashed line) also plotted as a reference.

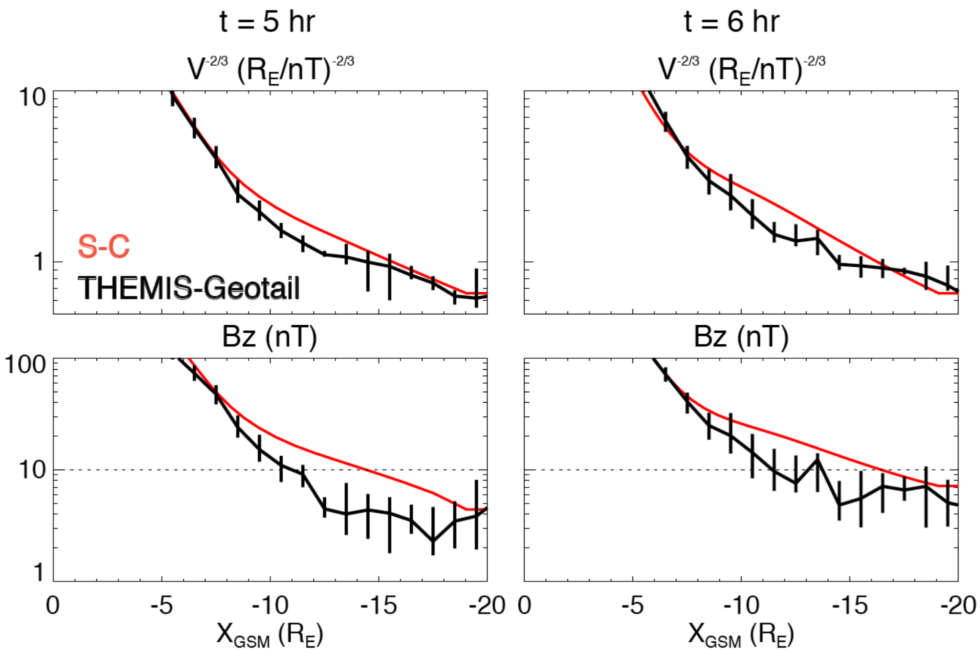

Figure 3.6 Radial profiles of $V^{-2/3}$ (top panels) and B_z (bottom panels), at midnight, for self-consistent magnetic field (red solid line) and THEMIS-Geotail statistical data (black line corresponds to the median, while the minimum and maximum of the error bar indicate the 25% and 75% percentiles respectively), under weak convection (on the left), and enhanced convection (on the right). Dashed lines indicate B_z = 10 nT for reference.

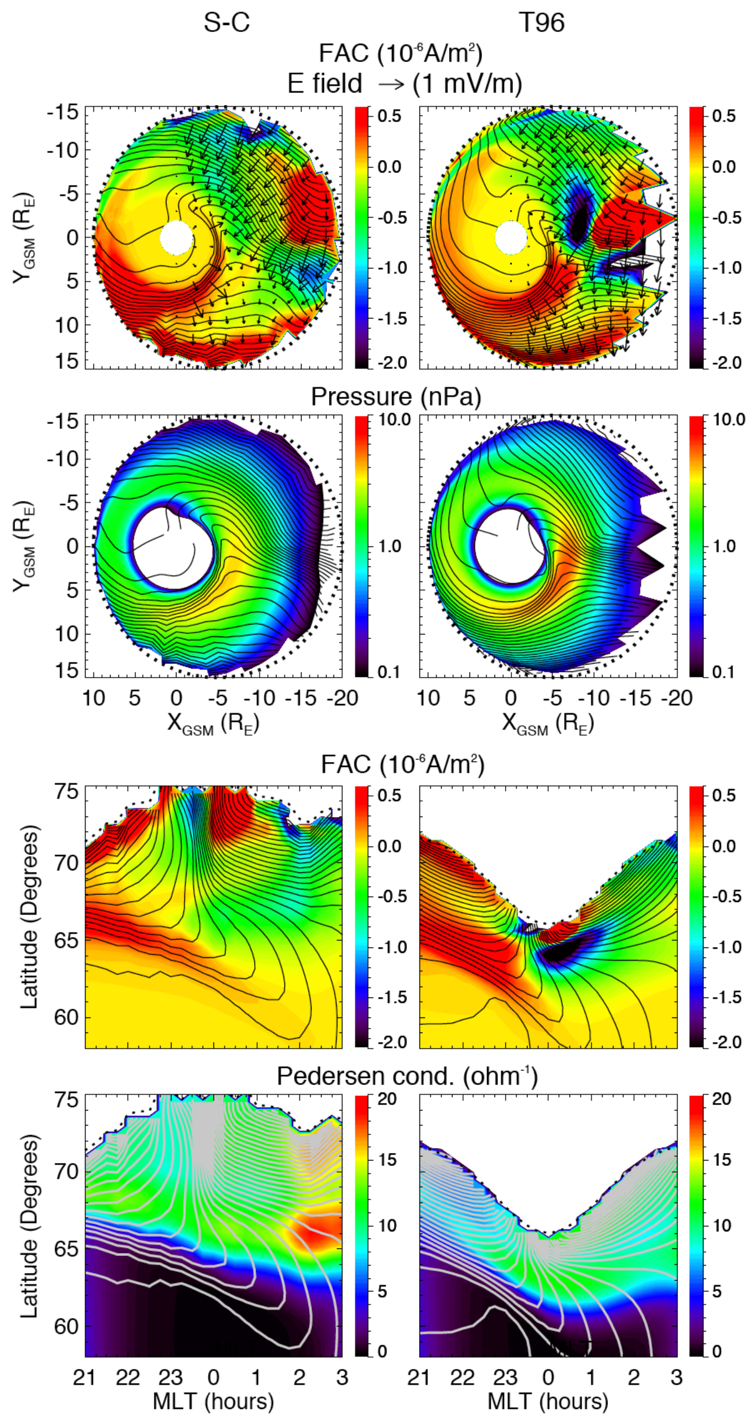

Figure 3.7 Field-aligned currents (FAC) (blue for upward, red for downward) and pressure profiles mapped to the equatorial plane, as well as electric fields (black arrows) (top four panels); FAC and Pedersen conductivity profiles in the ionosphere (bottom four panels) at t = 10 hr, under self-consistent (on the left) and under T96 (on the right) magnetic field.

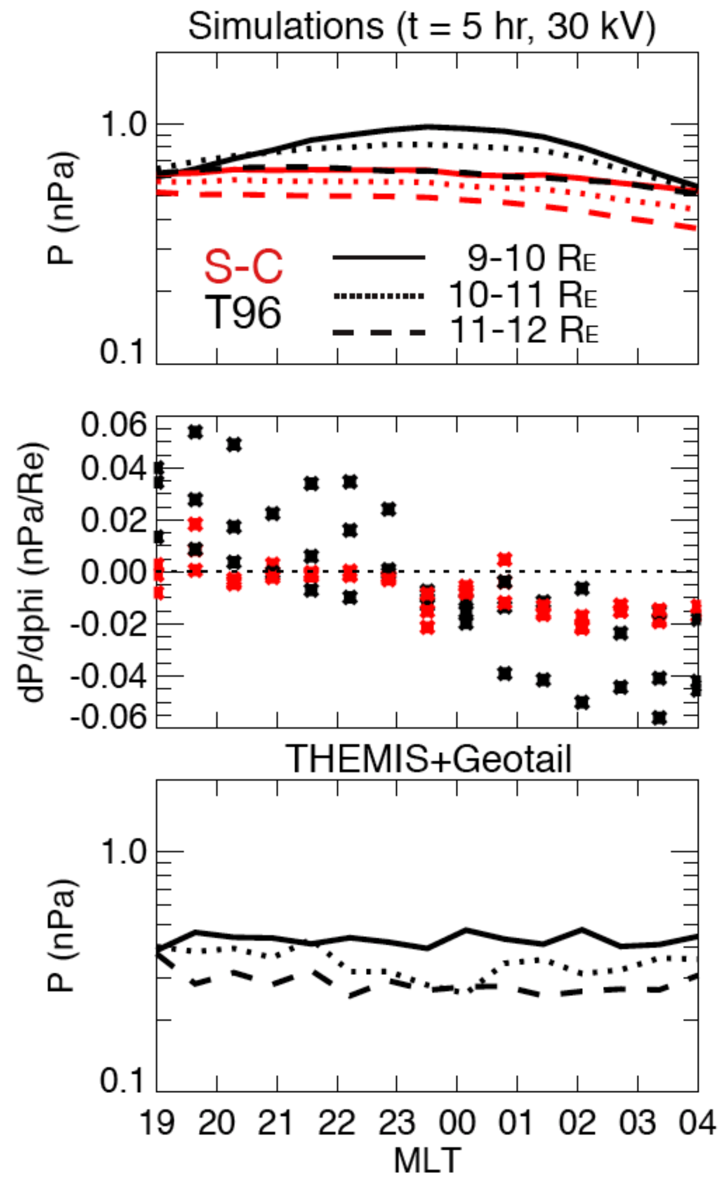

Figure 3.8 Azimuthal pressure profile (top panel) and pressure gradient (middle panel) using T96 (black) and self-consistent magnetic field (red), as well as statistical THEMIS-Geotail azimuthal pressure profiles (bottom panel), for r_0 = 9-10 R_E (solid line), r_0 = 10-11 R_E (dashed line) and r_0 = 11-12 R_E (dotted line) under weak convection.

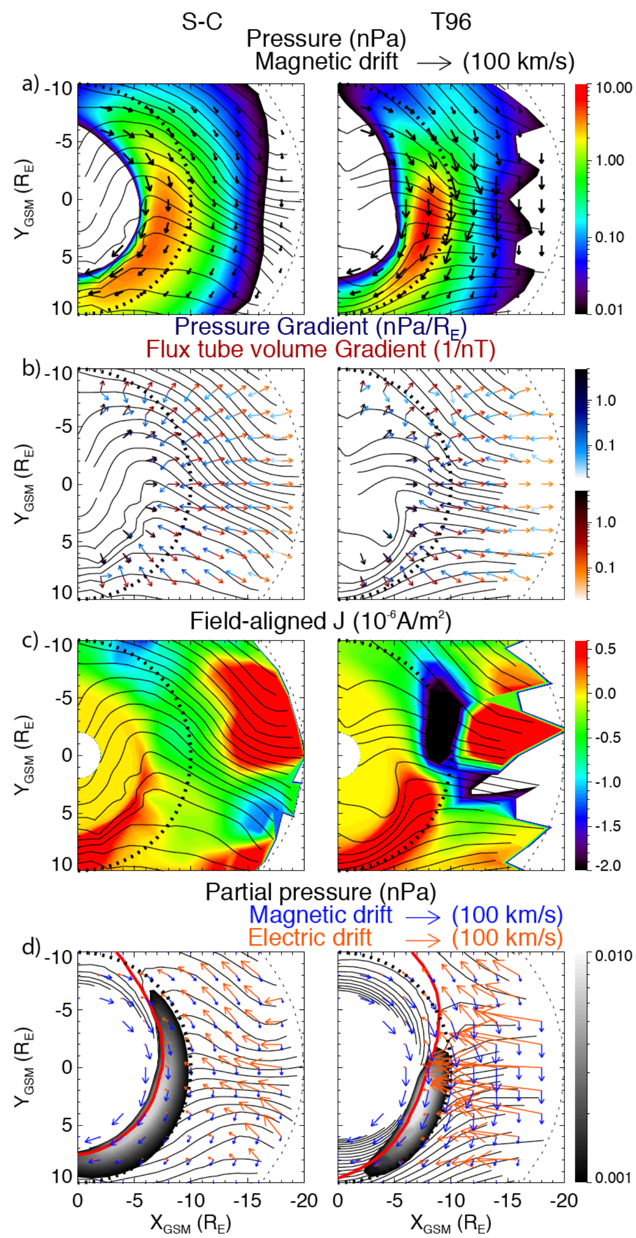

Figure 3.9 a) Pressure with color contours, equipotentials with black contours and magnetic drift with black arrows. b) Unit vectors of ∇P with blue and ∇V with red, going from lighter to darker color with increasing magnitude; equipotentials with black contours. c) FAC with color contours (blue for upward, red for downward), equipotentials with black contours. d) Magnetic drift of thermal protons (5 keV at 20 R_E at midnight) with blue arrows, electric drift with orange arrows, thermal protons' open trajectories (only beyond 5 R_E), with black contours, thermal protons' inner edge with red line (the particle content, η, in the region inward of the red line is less than 20% of the boundary value at midnight), partial pressure profile of the same energy protons with a grey-scale contour. The thick dotted line in all the plots is the 10RE circle and all the plots are for t = 6 hr (convection has just reached 90kV)

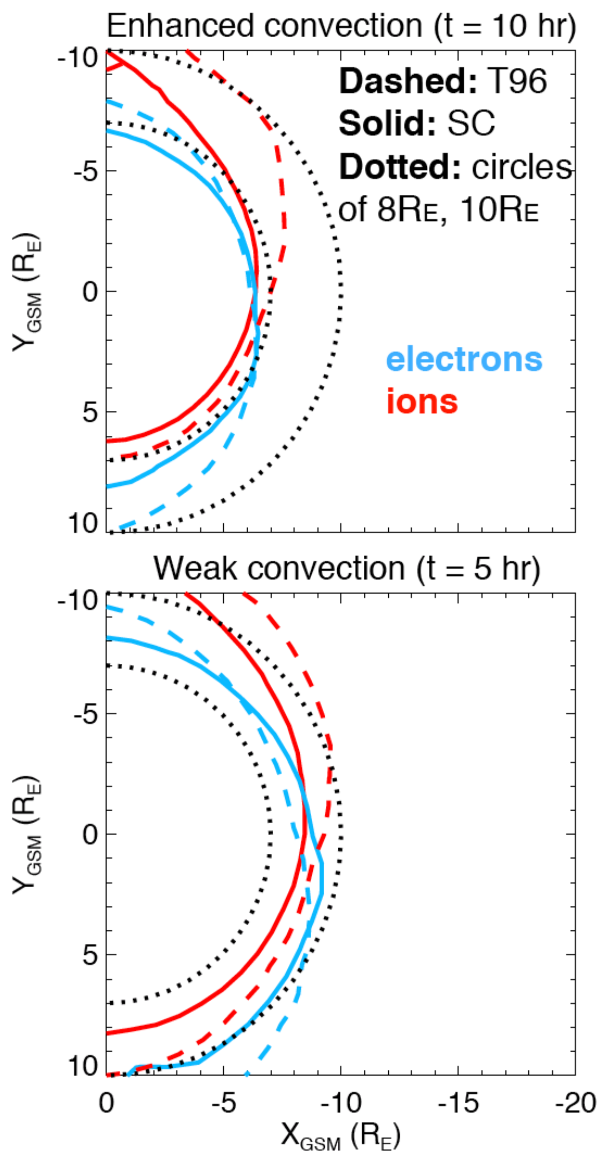

Figure 3.10 Equatorial inner edges of protons (red line) and electrons (blue line) of energies of 5 keV and 1 keV respectively (thermal energies) at 20 R_E at midnight, under self-consistent (solid line) and T96 (dashed line) magnetic field at t = 10 hr (after 4 hr of enhanced, 90kV, convection) on the left, and at t = 5 hr (after 5 hr of weak, 30kV, convection) on the right.

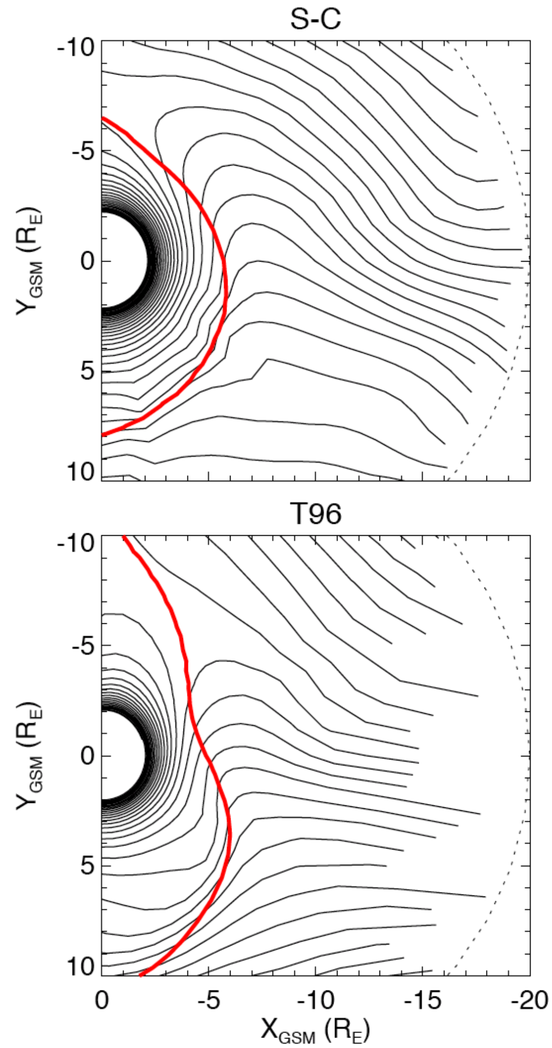

Figure 3.11 Proton trajectories with black contours and inner edge for low-energy protons (400 eV at 20 R_E at midnight) with red line, at t = 6 hr (convection has just reached 90kV).

3.4 Summary – Conclusions

In this chapter we have presented results from self-consistent simulations using the RCM coupled with a modified Dungey force-balanced magnetic field model. To investigate the role of the interplay between magnetic field and plasma sheet transport in the R2 coupling, we have compared our self-consistent RCM results (SC run) with the results from a RCM run using T96 magnetic field (T96 run).

In the SC run, compared to the T96 model run, duskward magnetic drift is weaker for the thermal plasma sheet protons, which is the main contributor to plasma pressure, thus leading to weaker azimuthal pressure gradient in the inner magnetosphere. Since the gradient of flux tube volume is mainly directed radially, the weaker azimuthal pressure gradients result in weaker R2 FAC and thus less efficient electric field shielding in the near Earth region. The less efficient shielding allows thermal plasma sheet protons to penetrate further earthward in the postmidnight sector. As a result, the inner edge of the these thermal protons is more azimuthally symmetric in the SC run, while in the T96 run there is a much more pronounced dawn-dusk asymmetry.

Investigation of the inner edges of both protons and electrons shows that they are closer to each other and are more azimuthally symmetric in the SC run than in the T96 run. The electron inner edge is earthward (tailward) of the proton inner edge in the postmidnight (premidnight) sector and the two edges intersect at around midnight. Comparing weak convection to enhanced convection, the inner edges of both protons and electrons in the SC run become more azimuthally symmetric with increasing convection and are located even closer to each other. Also, the intersection of the ion and electron edges moves duskward under enhanced convection.

The locations of the inner edges and the relative position between ion and electron edges determine the characteristics of the Harang reversal and the SAPS. More specifically, in the postmidnight sector, low-energy protons, which are responsible for the downward FAC of the overlapping FAC pair causing the Harang reversal, penetrate further toward dawn in the SC run because of less efficient shielding. This results in further dawnward extension of the Harang reversal. In the premidnight sector, the fact that the inner edges of protons and electrons are located closer to each other in the SC run causes the SAPS to be more confined in its radial and latitudinal width.

We found that the magnitudes of the azimuthal pressure gradient, the inner edges of thermal protons and electrons, the latitudinal range of the Harang reversal, and the radial and latitudinal width of the SAPS become more consistent with observations when taking into account the feedback from force-balanced magnetic fields.

CHAPTER 4 | Effect of an MLT dependent electron loss rate on the Magnetosphere - Ionosphere coupling

Electron loss reduces the plasma sheet electrons as they drift earthward, as well as causes electron precipitation that is the main contributor to auroral conductance. Realistic electron loss is thus important for modeling magnetosphere - ionosphere (M-I) coupling and the degree of plasma sheet electron penetration into the inner magnetosphere. We have evaluated these effects of the electron loss by simulating plasma sheet transport under self-consistent electric and magnetic field using and different loss rates with the Rice convection model (RCM) coupled with a force-balanced magnetic field solver. We used different magnitudes of i) strong diffusion everywhere electron loss rate (strong rate) and ii) a more realistic loss rate with its MLT dependence determined by wave activity (MLT rate). We found that electron pressure under the MLT rate is larger compared to the strong rate. The dawn-dusk asymmetry in the precipitating electron energy flux under the MLT rate, with much higher energy flux at dawn than at dusk, agrees better with statistical DMSP observations. High-energy electrons in the inner magnetosphere under the MLT rate can remain there for many hours or more while those under the strong rate get lost within minutes. Under the MLT rate, the remaining electrons cause higher conductance at lower latitudes; thus after a convection enhancement, the shielding of the convection electric field is less efficient, and as a result, the ion plasma sheet penetrates further earthward into the inner magnetosphere than under the strong rate. The results presented in this chapter have been submitted to *Journal of Geophysical Research* [*Gkioulidou et al.*, 2012].

4.1 Introduction

The electrons in the plasma sheet constantly undergo pitch angle scattering through wave-particle interactions and precipitate into the ionosphere. The precipitating electrons are the main contributors to ionospheric conductivity within the nightside auroral oval, the conductivity being one of the main factors controlling magnetosphere - ionosphere (M-I) coupling. More specifically, the spatial distribution of electron precipitation substantially affects the distribution of conductivity. This, in turn, strongly affects the spatial distribution of the convection electric field, which plays a crucial role in the transport of the plasma sheet particles into the inner magnetosphere [e.g. *Ebihara et al.*, 2004; *Gkioulidou et al.,* 2009], including the lower energy electrons that contribute to the aurora and the higher-energy electrons that become the seed population for radiation belt electrons [*Thorne et al.*, 2007]. Furthermore, the precipitation also results in loss of electrons from the plasma sheet, thus decreasing the number of electrons transported to the inner magnetosphere. Therefore, a realistic electron loss is crucial to modeling the electron population in the inner magnetosphere.

The pitch angle scattering can be due to either electrostatic cyclotron harmonic waves (ECH) [*Kennel et al.*, 1970; *Kennel and Ashour-Abdalla*, 1982; *Ashour-Abdalla and Kennel*, 1978; *Lyons et al.*, 1974, *Ni et al.*, 2011a] or whistler mode waves [*Joshstone et al.*, 1993; *Meredith et al.*, 1999; *Ni et al.*, 2011b]. *Chen and Schulz* [2001] established a magnetic local time (MLT) dependent scattering rate model (hereafter referred to as the Chen rate) based on statistical observations of 0.1 – 5 kHz frequency waves, which includes both ECH and whistler mode emissions. The observations show wave activity peaking towards dawn, as well as in the morning sector. Simulating bounce-averaged drifts of electrons and their losses by using the Chen rates, they obtained precipitating energy fluxes and conductivities that agreed better with statistical studies [*Hardy et al.*, 1985, 1987] than using strong diffusion everywhere loss rates. They also found better agreement between their modeled precipitating energy fluxes and PIXIE (Polar Ionospheric X-ray Imaging Experiment) data from a single storm event [*Anderson et al.*, 2000]. Although the Chen rate model is fairly simple, it is one step closer to more realistic loss rate modeling. However, the electric and magnetic field used in their simulations was not self-consistent, so the effect of the electron loss on the M-I coupling and transport of electrons into the inner magnetosphere could not be appropriately evaluated. Recently, *Ni et al.* [2011a; 2011b] have modeled loss rates, evaluating the contribution of both whistler mode chorus and ECH waves and taking into account the observed dependence of wave activity on geomagnetic activity. However, their results are limited in radial distance (L = 6) and MLT (0000-0600). Thus no other global loss rate models have become available yet that are more realistic than the Chen rate model.

Therefore in this study, we investigate the effect of the Chen loss rate, in comparison with strong diffusion loss rate, on the ion and electron plasma sheet, their coupling with the ionosphere, and their penetration into the inner magnetosphere. We do this by modeling these processes under self-consistent electric and magnetic fields with the Rice Convection Model (RCM) combined with a modified Dungey force-balanced magnetic field solver. The MLT-dependent tail ion and electrons sources are established based on statistical Geotail observations. In section 4, we conduct different simulation runs with the Chen rate, strong diffusion rate, and fractions of the two rates for conditions of substorm growth phase and evaluate their resulting precipitating electron energy fluxes against statistical DMSP electron energy fluxes that were obtained also during the growth phase. We focus on the substorm growth phase only because the RCM cannot appropriately simulate non-adiabatic processes during the substorm expansion phase. We also compare the equatorial electron differential fluxes with statistical THEMIS electron energy spectra. In both the ionosphere and the equatorial plane, the simulations using Chen rates are found to better account for the observations. After establishing that there is better agreement between observations and simulation results using the more realistic Chen rate, in section 5, we evaluate how the M-I coupling under different loss rates affects the development of the shielding of the penetration electric field in the inner magnetosphere. For this part of the study we choose storm-like convection enhancement, which is stronger than the substorm growth phase one, so that the shielding and its effects on the earthward penetration of the plasma sheet, can be seen more clearly. We find that the shielding under the Chen rate in the inner magnetosphere is found to be less efficient, allowing for deeper penetration of the plasma sheet.

4.2 Model

4.2.1 RCM combined with modified Dungey force-balanced magnetic field solver

The RCM [*Toffoletto et al.*, 2003] combined with a modified Dungey force-balanced magnetic field solver [*Gkioulidou et al*., 2011] calculates the bounce–averaged electric and magnetic drift of ions and electrons assuming isotropic distributions along the magnetic field lines and slow flow approximation, within self-consistently computed electric and magnetic fields. Details of the coupled model are given in section 3.2 of Chapter 3.

4.2.2 RCM electron loss

The RCM treats particle drifts under the assumption of strong, elastic pitch-angle scattering. Particles of the same energy invariant λ_k in eV·(R_E/nT) ($\lambda_k = E_k \cdot V^{2/3}$, where k is an index for energy channel and E_k is particle kinetic energy in eV and V is the flux tube volume in R_E/nT) move along the electric and magnetic drift paths so the total energy $q\Phi + \lambda_k \cdot V^{-2/3}$ is conserved for time-independent electric and magnetic fields, where q is electric charge (+1 for protons and –1 for electrons). The number of particles of energy invariant λ_k within the energy range from $\lambda_{k,min}$ to $\lambda_{k,max}$ and within V is defined as particle number content η_k ($\eta_k = 4\pi \cdot 2^{1/2} m^{-3/2} \cdot \int |\lambda_k|^{1/2} \cdot f_k(\lambda) d\lambda$ in $6.37 \cdot 10^2$ nT^{-1} cm^{-2}, where the integral is over the λ-range covered by energy channel k, m is the particle's mass, and f is phase space density, so that $\eta_k = n_k \cdot V$, where n_k is partial number density within the energy channel). η_k is conserved along these particles' drift paths unless there are local particle losses that remove existing particles or local particle sources that add new particles. In the RCM, electron loss due to precipitation is modeled by

$$\eta_k(\mathbf{x},t) = \eta_k(\mathbf{x} - \mathbf{v}dt, t - dt)e^{-dt * loss\ rate} \tag{4.1}$$

where **x** is the position and **v** the drift speed. The loss rate used in our simulations will be discussed in more detail in section 4.3.1.

4.2.3 Electron precipitation

Electrons that get lost from the plasma sheet precipitate into the ionosphere. The electron precipitating energy flux Φ_E in erg cm^{-2} s^{-1} is expressed by

$$\Phi_E = \pi \sum_k E_k J(E_k) dE \tag{4.2}$$

where dE is the width of the energy channel, and $J(E_k)$ is the precipitating electron differential flux in sr^{-1} eV^{-1} cm^{-2} s^{-1} given by

$$J(E_k) = 7.39 \cdot 10^{-16} \frac{\sqrt{\lambda_k}\,\eta_{k(precipitating)} V^{-2/3}}{\frac{\lambda_{k+1} - \lambda_{k-1}}{2}} \tag{4.3}$$

$\eta_{k(precipitating)}$ in equation (4.3) is the flux tube volume electron content within the loss cone and it depends on the η_k outside the loss cone and the electron loss rate,

$$\eta_{k(precipitating)} = factor * \eta_k \tag{4.4}$$

where,

$$factor = \frac{loss\ rate}{strong\ diffusion\ loss\ rate} \tag{4.5}$$

The strong diffusion loss rate is the maximum precipitation loss rate for the case of zero field-aligned potential drop and is expressed by

$$1/\tau = \sqrt{\frac{E_k}{2m}}\frac{1}{B_i}\frac{1}{V} \tag{4.6}$$

where, B_i is the ionospheric magnetic field and m is the electron mass.

4.2.4 Auroral conductivity

The RCM auroral height-integrated Pedersen and Hall conductivities are estimated by the electron precipitation from the simulated plasma distributions, using the algorithms of *Robinson et al*. [1987], namely

$$\Sigma_p = \frac{40\langle E\rangle}{16 + \langle E\rangle^2}\Phi_E^{\ 1/2} \tag{4.7}$$

$$\frac{\Sigma_H}{\Sigma_p} = 0.45\langle E\rangle^{0.85} \tag{4.8}$$

where Σ_P and Σ_H are the height-integrated Pedersen and Hall auroral conductivities respectively in ohms^{-1}, Φ_E is the precipitating energy flux given by equation (4.2), and $<E>$ is the average energy in keV expressed by

$$\langle E\rangle = \frac{\sum_k E_k J(E_k)dE}{\sum_k J(E_k)dE} \tag{4.9}$$

where $J(E_k)$ is the precipitating electron differential flux given by equation (4.3).

4.3 Simulation setup

We investigate how the electron loss rate affects the electron precipitation to the ionosphere and to determine which electron loss rate can better account for the precipitating electron energy fluxes observed by DMSP. Since the statistical DMSP results used for the comparisons were obtained during the substorm growth phase, we established our simulation conditions for the solar wind driving and tail particle sources based on observations also during substorm growth phase.

4.3.1 Electron loss rates

We focus on the effect of different electron loss rates on the auroral conductivity, and through that on the convection electric field and the resulting penetration of the plasma sheet into the inner magnetosphere. We have conducted runs using six different scattering rates, which can be divided into two groups. The first group assumes the strong diffusion loss rate given by equation (4.6) everywhere and 2/3 and 1/3 of that rate, while the second group assumes the MLT dependent *Chen* rate and 2/3, and 1/3 of that rate. The magnitude and spatial distribution of waves vary with geomagnetic activity, but the Chen rate does not include this variability. The particular fractions chosen for both rates was motivated by the study of *Schumaker et al.*, [1989], where data from near-geosynchronous SCATHA satellite in conjunction with polar-orbiting P78-1 revealed that the average lifetimes of plasma sheet electrons exceed those for the case of isotropy by a factor between 2 and 3 for $Kp \le 2$ (between 1/2 and 1/3 of strong diffusion loss rate), and 1.5 for $Kp > 2$ (2/3 of strong diffusion loss rate).

The main difference between the above two groups is that the spatial dependence of the loss rate under strong diffusion comes only from the spatial variability of the magnetic field and electron energy, while the Chen rate ρ_{MLT} also depends on the wave activity through the SCATHA wave occurrence frequency distribution [*Koons and Roeder*, 1990], and is given by

$$\rho_{MLT} = \rho(E_k, L)\left[1 + 0.8\sin(\varphi - \pi/4)\right] \tag{4.10}$$

where φ is the MLT coordinate (0 at midnight, π/2 at dawn, π at noon, and 3π/2 at dusk), and

$$\rho(E_k, L) = \min[0.08E_k^{-1.32}, 0.4\times 10^{(2L-6+0.4\log_2 E_k)}](day^{-1}) \tag{4.11}$$

is a less than everywhere strong scattering rate (energy E_k in in MeV, and L is the dimensionless label of the magnetic shell), which is based on extrapolated theoretical lifetimes by *Albert* [1994] that have been renormalized to match the empirical lifetimes by *Roberts* [1969]. The Chen rate, ρ_{MLT}, reaches a maximum at φ = 9 MLT, and a minimum at φ = 21 MLT according to wave activity.

As shown later in this chapter, under a more realistic loss rate, electrons become less isotropic with decreasing radial distances in the inner magnetosphere due to weakening of the pitch angle diffusion. However, the RCM still treats the drift of these electrons as being isotropic. Nevertheless, in this study we overlook this inconsistency.

4.3.2 Plasma boundary and initial conditions

The location of the outer boundary is specified as a 15 R_E circle centered at X = -5 R_E and Y = 0 in the equatorial plane, and reaches X = –20 R_E at midnight and |Y| = 15 R_E at dawn and dusk. The latitudes in the ionosphere that map to the outer boundary vary as the magnetic field changes. The inner boundary is at r ~2 R_E. Along the outer boundary, the proton and electron distributions at different MLT are established from a fitting of two-component kappa distributions (see equation 2.6) to statistical results of substorm growth phase periods observed by Geotail and THEMIS from 1996 to 2010. Substorm onsets were obtained from the list of *Hsu et al.* [2012] that is based on an appropriate change of AL. The data have been sorted into three time-ranges 120 - 60, 60 - 30, and 30 - 0 min before the substorm onset. Only isolated substorms, i.e., at least 3hr after the previous substorm, were used.

For initial plasma conditions, we use plasma distributions obtained from our previous RCM run [*Wang et al.*, 2011], where we started with an empty magnetosphere and plasma from the tail boundary moved into the inner magnetosphere under many hours of enhanced convection. The boundary conditions and temporal variations of the polar cap potential drop of that run are shown in Figure 5 of *Wang et al.* [2011].

4.3.3 Simulation Runs

For all the six simulation runs, we first started with the plasma sheet boundary conditions corresponding to 120 – 60 min before the substorm onset, and ran simulations with constant cross polar-cap potential drop ($\Delta\Phi_{PC}$) of 40 kV for 5 simulation hours. This allows particles from the tail boundary to populate regions of open drift paths, while particles that remain on the closed paths are from the initial conditions. We then gradually increased $\Delta\Phi_{PC}$ to 60 kV over two hours (t = 5 - 7 hr). This specified $\Delta\Phi_{PC}$ change is determined from the statistical temporal variations of the $\Delta\Phi_{PC}$, based on Weimer model [*Weimer*, 1995], from the substorm events we used to establish our tail boundary conditions (see section 4.3.2). The magnetic field was updated every 10 minutes to maintain force balance with the RCM pressures. We also changed the plasma tail boundary conditions at t = 6:00 and 6:30 to those corresponding to 60 – 30 min, and 30 - 0 min before the onset respectively. In sections 4.4.1 - 4.4.2 below we discuss the results at t = 6:45 hr, which represents 15 min before substorm onset.

4.4 Simulation results

4.4.1 Effect of MLT dependent loss rates on plasma sheet and inner magnetosphere electrons

We first investigate how different loss rates affect the electron population in the plasma sheet and inner magnetosphere. We thus examine the lifetimes of plasma sheet electrons of different energies resulting from strong diffusion loss rates everywhere, in comparison to the Chen rates. Figure 4.1 compares the radial profiles of lifetime τ under strong diffusion (dashed lines) and lifetime under the Chen rate, $1/\rho_{MLT}$, (solid lines) for the five different invariant energies at 6.6 R_E identified in the figure) at dusk (top) and dawn (bottom). It can be seen that, at both local times and for energies of 4 keV and below, the Chen lifetimes approach the limit of strong diffusion lifetimes beyond 7 R_E. However, the Chen lifetimes of the two higher energy channels (14 keV and 54 keV) barely reach the strong diffusion limit (especially at dusk where the Chen rates are weaker). For energies above 4keV, the Chen lifetimes at dawn are significantly shorter that at dusk, and, for all energies, the Chen lifetimes become significantly larger than the strong diffusion ones with decreasing radial distances.

With the same outer particle sources, the different loss rates result in quite different spatial distributions of the electron plasma sheet. In Figure 4.2 we show electron pressures for the six different cases, with runs under the Chen rate and its fractions on the left, and runs under the strong diffusion rate and its fractions on the right. The bold dashed black line in all plots is the 8 R_E circle. As expected, for both the strong diffusion and Chen rates, electron pressure decreases with increasing loss rates, that is, going from a to b and c or from d to e and f. Also these differences become larger with decreasing radial distances, since the numbers of electrons are the same at the outer boundary for these runs. The electron pressures of the strong diffusion everywhere cases are clearly lower than those of the Chen rate cases in the premidnight sector. This is due to the Chen lifetimes for higher energy electrons being much larger than the strong diffusion everywhere lifetimes at dusk beyond 8 R_E, and it results in stronger dawn-dusk electron pressure asymmetry under strong diffusion everywhere. Finally, we note the significantly larger electron pressure inside 8 R_E for all the Chen rate cases, compared to the respective strong diffusion ones. This is due to the much weaker loss rates at smaller radial distances in the Chen rate cases, which allow the electrons trapped within the closed drift trajectories inside ~7 R_E to remain there for much longer time.

To further investigate this last point, Figure 4.3 shows the electron energy spectra at geosynchronous orbit at midnight (top), dusk (middle), and dawn (bottom), for strong diffusion rate cases (dashed lines) and for Chen rate cases (solid lines). We can see that, indeed, in the Chen rate cases, the differential flux of electrons of 10 keV and above is significantly increased in comparison with the strong diffusion everywhere cases especially at dusk where the Chen rate is weaker for high-energy electrons. We can also see the decrease in electron differential fluxes with increasing loss rate for both cases.

Figure 4.4 shows compares the electron energy spectra versus radial distance along the dawn meridian for the strong diffusion and Chen rate cases with the observed electron energy spectra taken from Figure 10 of *Wang et al.*, [2011]. Quantitative comparison of the differential flux magnitudes between the observations and modeling results is beyond the scope of this paper, since the observed energy spectra pertain to different geomagnetic conditions and to locations somewhat off the magnetic equator. Nevertheless, it is clear that, in addition to the nominal plasma sheet electrons of a few keV at r > ~7 R_E, there is a distinctive population of energies from 20 - 200 keV inside ~8 R_E in the Chen rate case that is not seen in the strong diffusion rate case. These are the electrons that penetrated further into the inner magnetosphere and remained there because of very long lifetime in the Chen loss rate. This high-energy electron population in the inner magnetosphere can be also seen in the observations, indicating the Chen rate provides a more realistic electron loss in the inner magnetosphere. The above comparison shows the importance of realistic electron loss to modeling electron radiation belts since this high-energy electron population is the seed particles for the radiation belts.

4.4.2. Effect of MLT dependent loss rates on electron precipitation to the ionosphere

Next, we examine the effect of MLT dependent loss rates on the precipitating plasma sheet electrons, which are known to be the main cause of diffuse aurora. More specifically, we focus on the effect on the precipitating electron energy fluxes and the Pedersen conductivity they produce.

4.4.2.1 Energy flux

Figure 4.5 shows ionospheric plots of the precipitating electron energy flux computed from (4.3) for all the six loss rate cases, with runs under the Chen rate and its fractions on the left, and runs under the strong diffusion rate and its fractions on the right. We can notice i) a clear difference in the azimuthal distribution of the energy flux between the two major groups, with more significant enhancement in the premidnight energy fluxes in the strong diffusion everywhere cases than in the Chen rate cases, and ii) that as the fraction increases (from a to c or from d to f), the overall energy flux increases, for both the major groups.

As indicated by equations (4.1) and (4.6), the number of electrons precipitating is determined by the loss rate and the number of electrons in the plasma sheet, while the number of particles in the plasma sheet is determined by how many electrons have been lost as they drift from the outer boundary, which, as shown in equation (4.1), depends on the same loss rate. Combining equations (4.1), (4.4), and (4.5) we can estimate the number of precipitating electrons under a given loss rate η_p relative to the number of precipitating electrons under strong diffusion everywhere $\eta_{p,\,strong}$ as electrons drifting from the same boundary sources,

$$\frac{\eta_{p,strong}}{\eta_p} = \frac{1}{factor} exp\left[\int -dt \cdot (1/\tau(t)) \cdot (1 - factor(t))\right]$$

where τ is the lifetime of strong diffusion given by equation (4.6) and *factor* is as defined in equation (4.5). Note that $factor \leq 1$. Therefore, η_p is expected to be smaller than $\eta_{p,\,strong}$ for time scales shorter than $-[ln(factor)/(1\text{-}factor)]\cdot\tau$. For example, for a factor of 1/3 and τ = 200 min for typical thermal plasma sheet electrons (see Figure 4.1), as electons drift earthward from the tail boundary, η_p will be smaller than $\eta_{p,\,strong}$ within ~5 hr, which is long enough for these electrons to occupy the region of the plasma sheet.

The above estimate can explain why i) the precipitating energy flux is enhanced in the premidnight sector in the strong diffusion everywhere cases compared to the Chen rate ones, even though the electron plasma sheet pressure is smaller in that region and ii) the larger the fraction of a rate the more enhanced the energy flux, even though, again, the electron plasma sheet pressure is smaller.

We next compare our results with the statistical diffuse aurora electron precipitation from DMSP data shown in Figure 4.6, which shows average energy fluxes between 15 min – 0 min before the substorm onset. It can be seen that the Chen rate cases capture much better features of the DMSP azimuthal distribution, in particular the fluxes being much weaker in the premidnight than in the postmidnight sector. The strong diffusion everywhere cases have either too large duskside precipitation (the 2/3 of strong diffusion and strong diffusion everywhere cases) or a very symmetric premidnight – postmidnight (between 21hr and 3hr of MLT) distribution (1/3 of strong diffusion everywhere case). It can also be seen that the result of the 2/3 of Chen rate is closest to the observations. The better agreement with the Chen rate indicates that it is crucial to take into account the distributions of wave activity in order to prescribe the loss rate more realistically. This improvement is also quite encouraging considering the simplicity of the Chen rate. Since the magnitude and spatial distribution of waves vary with geomagnetic activity, in would be beneficial to develop a loss rate to be developed parameterized with geomagnetic activity in the future. Note that our simulated energy fluxes are located ~2^o - 5^o poleward of the observed ones, which is mainly due to the limitation of field line stretching of our magnetic field model (see discussion in section 3.2.4).

4.4.2.2 Conductivity

In Figure 4.7, similar to Figure 4.5, we show Pedersen conductivity computed from equation (4.7) for all the six loss rate cases. Note that we have also plotted the background Solar-EUV-generated conductivity. We see azimuthal distributions that are similar to those for the energy fluxes discussed above, as expected since the Pedersen conductivity is proportional to the square root of the precipitating energy flux. There is higher conductivity in the postmidnight sector as well as a pronounced peak in the premidnight sector for the strong diffusion everywhere cases, while the Chen rate cases have a more pronounced dawn-dusk asymmetry with their conductivities in the premidnight sector weaker than those in the post midnight sector.

4.4.3 Effect of loss rates on M-I coupling

In the previous section we showed how different electron loss rates affect the electron precipitation to the ionosphere and the resulting ionospheric Pedersen conductivity. In this section we investigate the effect of the different electron loss rates on the M-I coupling, with a focus on the penetration of the plasma sheet into the inner magnetosphere, since the shielding of the penetration strongly depends on the ionospheric conductivity [e.g. *Gkioulidou et al.*, 2011].

For this part of the study we conducted two different runs, one with the strong diffusion everywhere electron loss rate and the other one with the Chen electron loss rate. For both runs, $\Delta\Phi_{PC}$ of 40 kV is kept constant for 5 simulation hours (t = 5 hr), and we then increase it sharply to 90 kV within 10 minutes and keep it constant for another 10 minutes (t = 5:20 hr). We chose this sharp and large increase of the $\Delta\Phi_{PC}$, which is more representative of storm time convection enhancement than a substorm growth phase, because the shielding development is easier to evaluate by keeping the convection steady after it has been substantially enhanced.

In Figure 4.8 we show the Pedersen conductivity together with equipotential contour lines within the ionosphere at t = 5:20 hr for the Chen loss rate case (top) and the strong diffusion rate case (bottom). We see that the shielding of the convection electric field has started developing for both cases (notice the bending of the equipotential contour lines at lower latitudes). We can see that, although above 68^{o} latitude, the conductivity in the strong diffusion everywhere case is stronger than in the Chen rate case, below 68^{o} latitude, there is a sharp decrease in the conductivity in the strong diffusion everywhere case, while the decrease in the Chen rate case is smoother at all nightside MLTs. Especially at the postmidnight MLTs (0 – 4 hr), the conductivity in the Chen rate case below 65^{o} is ~2 ohms^{-1} and it extends to as low as ~63^{o}, while conductivity drops to almost zero below 65^{o} for the strong diffusion everywhere case. Although the precipitating energy flux is larger in the plasma sheet region, this more abrupt conductivity decrease from higher to lower latitudes in the strong diffusion everywhere case is due to the electron population that contributes to the conductivity getting lost rapidly due to very short lifetimes inside 6 R_E. For the Chen rate case, the lifetimes increase significantly with decreasing distance, allowing the electrons in the closed drift path region to remain there for a longer time (see discussion in section 4.4.1) and produce conductivity.

The relatively lower conductivity at lower latitudes in the strong diffusion everywhere case leads to stronger shielding of the convection electric field in that region, as indicated by the sharper bending of the equipotentials. The different shielding development at different latitudes for the two cases can be seen more clearly in Figure 4.9(a) where we have plotted the latitudinal profile of the azimuthal component of the electric field (the negative azimuthal electric field gives equatorward flow in the ionosphere and earthward flow in the equatorial plasma sheet) at MLT = 21 hr for the Chen rate case (blue curves) and the strong diffusion rate case (red curves), at t = 5:10 hr (just after reaching $\Delta\Phi_{PC}$ = 90 kV, dashed lines) and t = 5:20 hr (90 kV for 10 min, solid lines). We see that from 5:10 to 5:20, at higher (lower) latitudes, above 66^o (below 65^o), in the strong diffusion everywhere case, where the conductivity is higher (lower) than in the Chen rate one, the electric field magnitude decreases less (more), which means that the shielding development is slower (faster).

The azimuthal component of the electric field is responsible for the penetration of the plasma sheet population into the inner magnetosphere. In Figure 4.9(b) we show the longitudinal ion pressure profiles at 5.5 R_E (this radial distance is chosen because it was earthward of the plasma sheet inward edge before the convection enhancement), at t = 5:20 hr, for the Chen rate case (blue) and the strong diffusion rate case (red). The ion pressure is larger in the Chen rate case than in the strong diffusion rate case, which is due to the protons penetrating further earthward in the Chen rate case due to slower shielding development at lower latitudes. On the other hand, in Figure 4.9(c) we have plotted the same pressure profiles at 8 R_E (this radial distance was already within the plasma sheet before the convection enhancement), which corresponds to higher latitudes, and, as it can be seen, the ion pressure is higher for the strong diffusion everywhere case in that region. This is due to larger energization of protons by the stronger electric field because of the less efficient shielding development in the strong diffusion everywhere case.

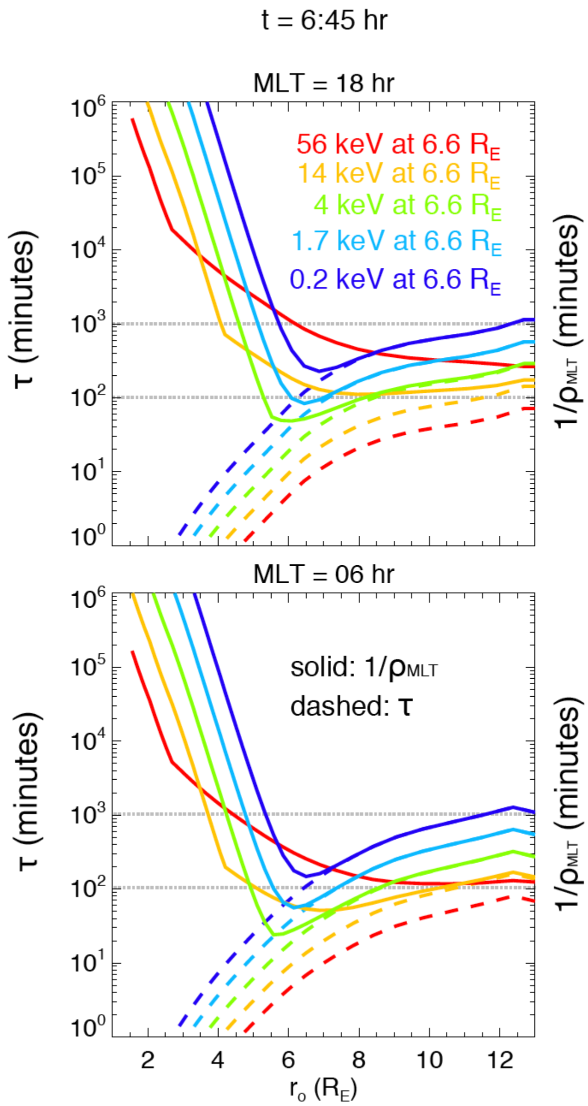

Figure 4.1 Radial profiles of lifetime τ against strong diffusion with dashed lines, and lifetime $1/\rho_{MLT}$ with solid lines, for five different invariant energies corresponding to 56, 14, 4, 1.7, 0.2 keV at 6.6 R_E with red, yellow, green, light blue, and purple respectively, at dusk (top) and dawn (bottom). The dashed and dotted grey lines indicate 100 and 1000 minutes.

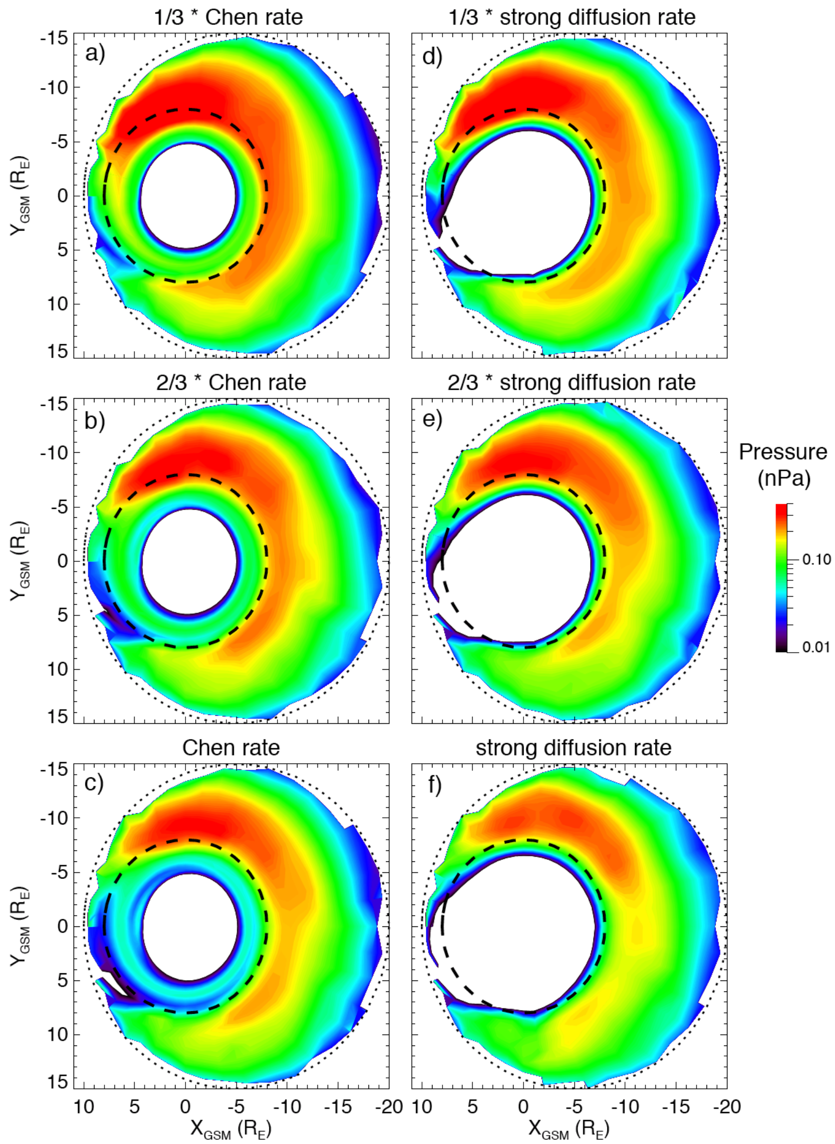

Figure 4.2 Electron pressures for the runs using a) 1/3 of Chen loss rate, b) 2/3 of Chen loss rate, c) Chen loss rate, d) 1/3 of strong diffusion everywhere loss rate, e) 2/3 of strong diffusion everywhere loss rate, f) strong diffusion loss rate everywhere. The bold dashed black line in all plots is the 8 R_E circle.

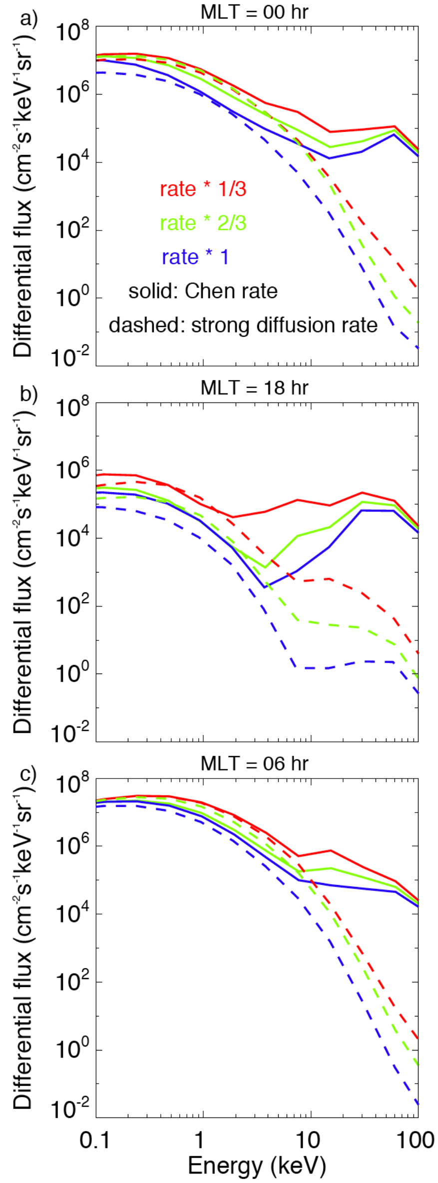

Figure 4.3 Electron energy spectra at geosynchronous at midnight (top), dusk (middle), and dawn (bottom), for strong diffusion rate and its fractions cases with dashed lines, and for Chen rate and its fractions cases with solid lines (fraction of 1/3 with red, 2/3 with green, 1 with blue).

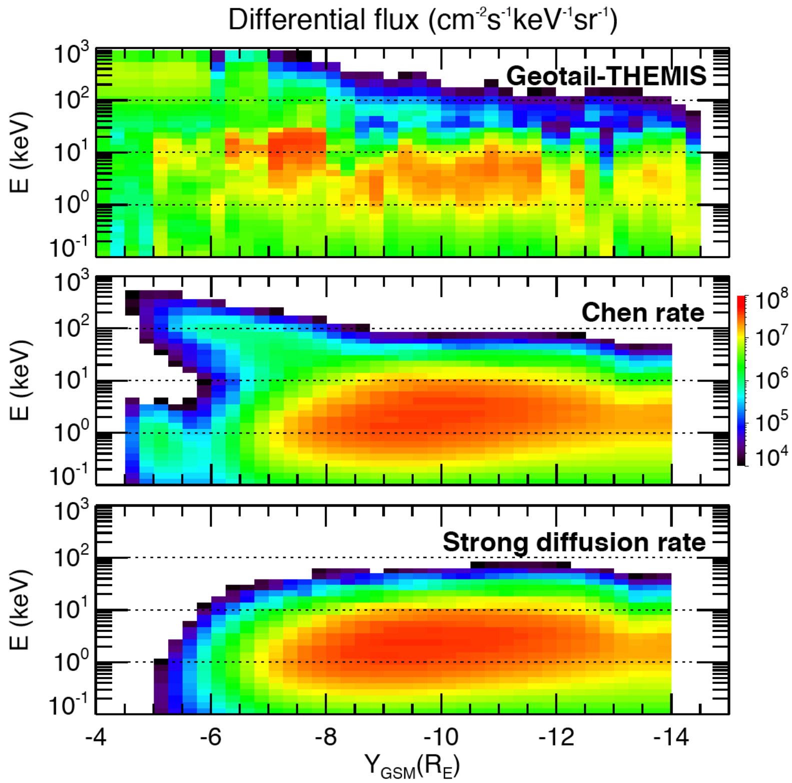

Figure 4.4 Electron energy spectra along the dawn meridian for the strong diffusion everywhere loss rate case (bottom), Chen loss rate case (middle), and observed electron energy spectra taken from Figure 10 of *Wang et al.*, [2011].

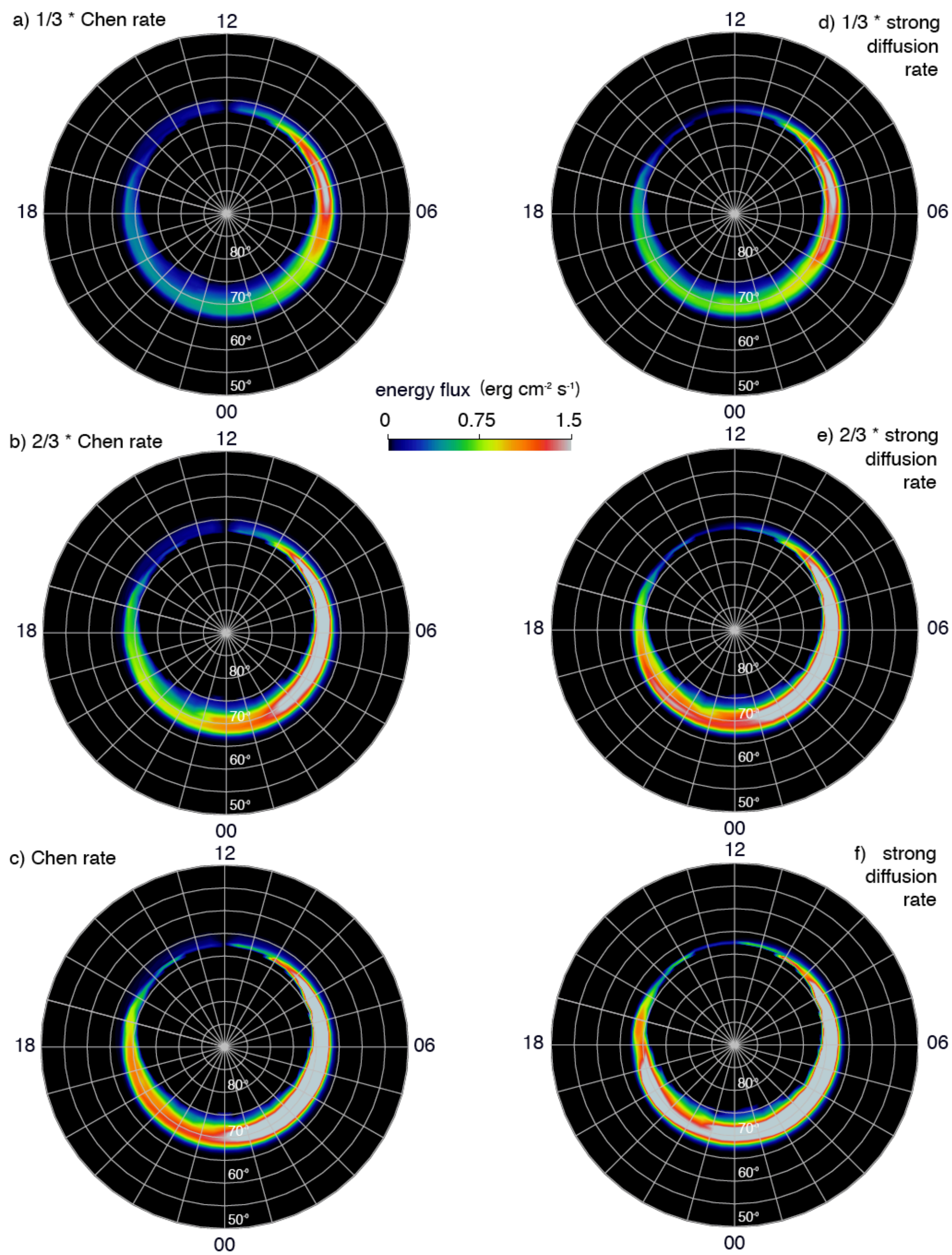

Figure 4.5 Ionospheric plots of the precipitating electron energy flux for the runs using a) 1/3 of Chen loss rate, b) 2/3 of Chen loss rate, c) Chen loss rate, d) 1/3 of strong diffusion everywhere loss rate, e) 2/3 of strong diffusion everywhere loss rate, f) strong diffusion loss rate everywhere.

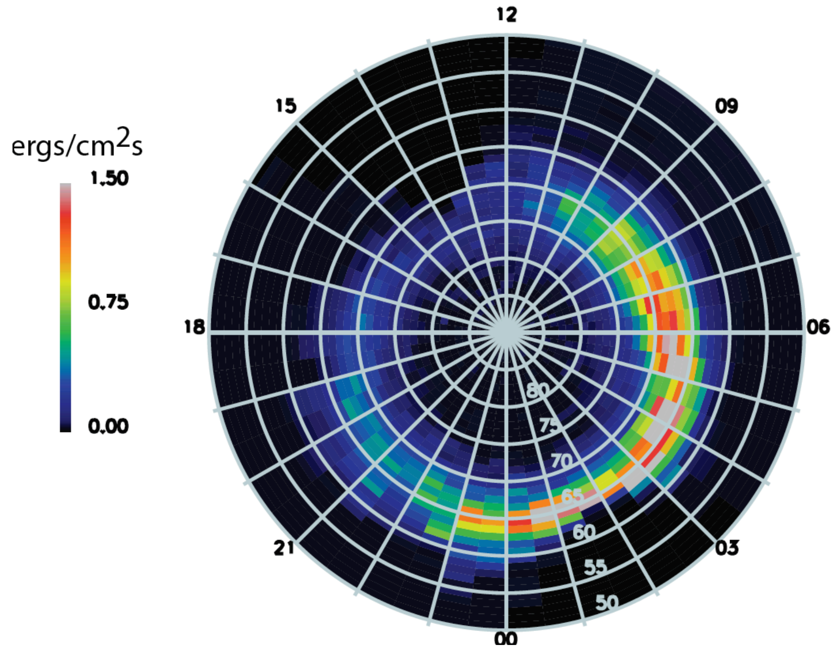

Figure 4.6 Diffuse aurora electron precipitation based on statistical DMSP data of average electron energy fluxes between 15 min – 0 min prior to substorm onset.

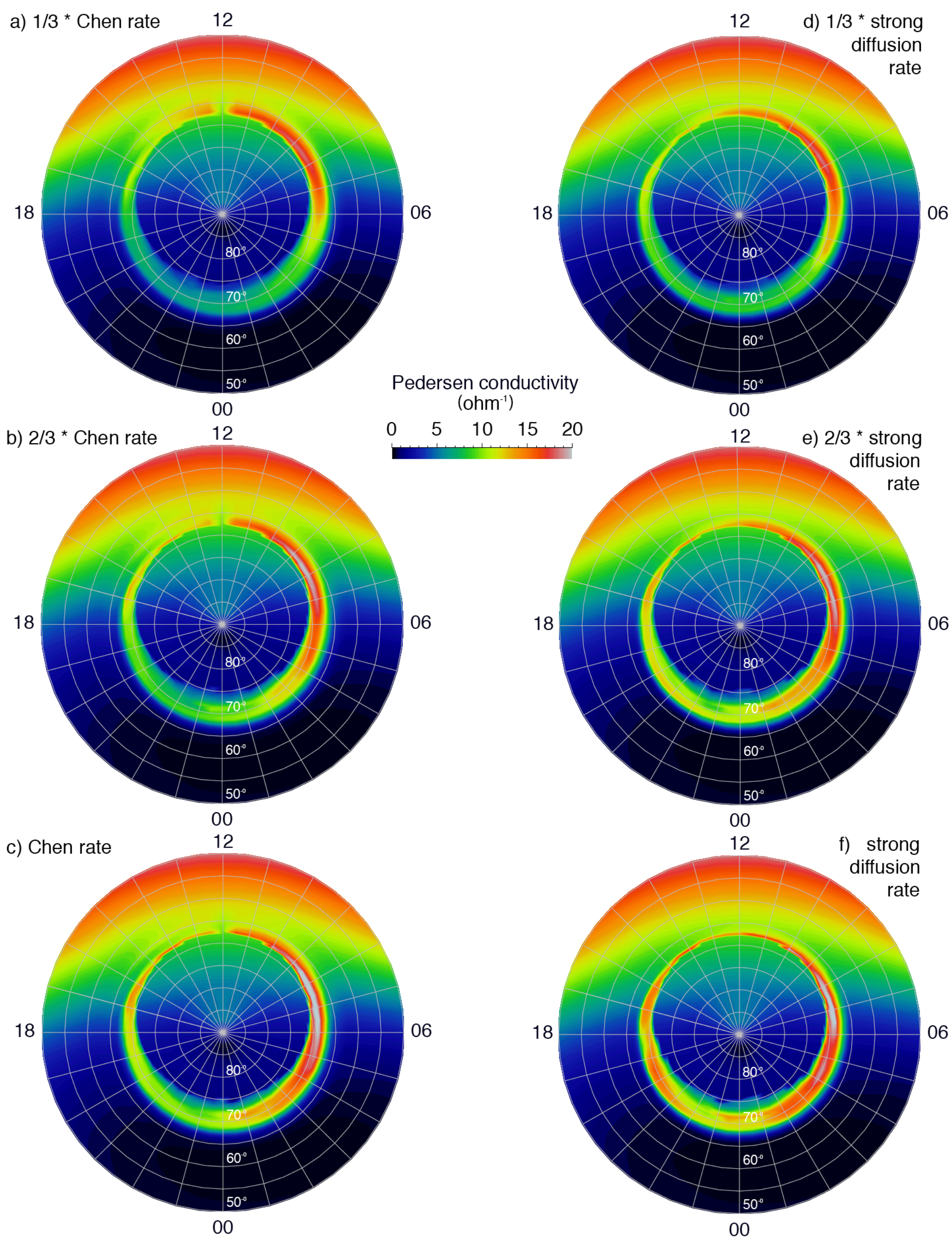

Figure 4.7 Ionospheric plots of the Pedersen conductivity for the runs using a) 1/3 of Chen loss rate, b) 2/3 of Chen loss rate, c) Chen loss rate, d) 1/3 of strong diffusion everywhere loss rate, e) 2/3 of strong diffusion everywhere loss rate, f) strong diffusion loss rate everywhere.

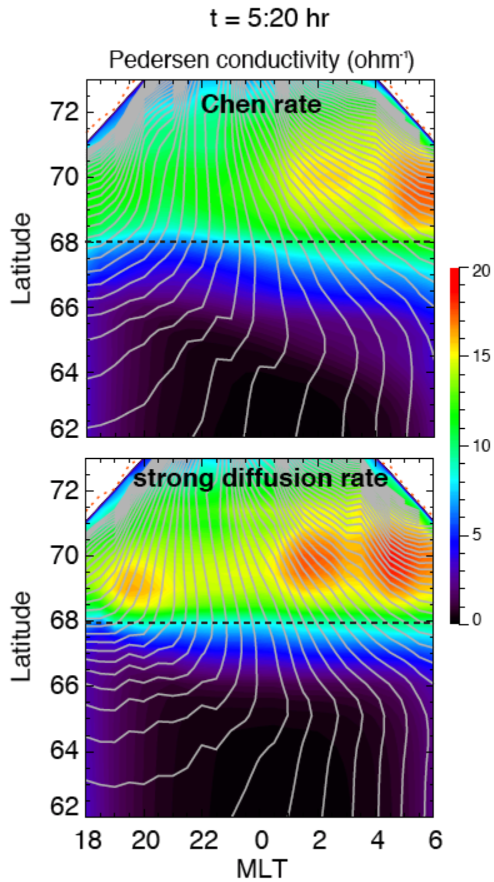

Figure 4.8 Pedersen conductivity and equipotential contour lines of 0.5 kV interval, at t = 5:20 hr, for the Chen loss rate case (top), and the strong diffusion rate case (bottom). Black dotted line indicates 68^{o} latitude.

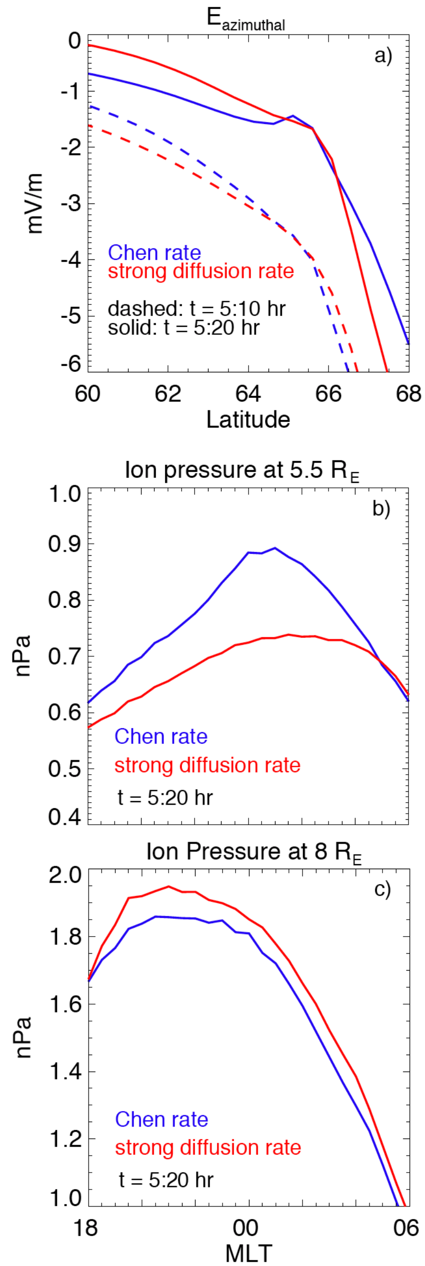

Figure 4.9 a) Latitudinal profile of the azimuthal component of the electric field at MLT = 21 hr for the Chen rate case (blue curves) and the strong diffusion rate case (red curves), at t = 5:10 hr and t = 5:20 hr, b) longitudinal ion pressure profiles at 5.5 R_E at t = 5:20 hr, for the Chen rate case (blue), and the strong diffusion rate case (red), c) same as b) but at 8 R_E.

4.5 Summary – Conclusions

We have used simulation results to evaluate the effects of a more realistic and wave-activity based MLT dependent electron loss rate (the Chen rate), in comparison with strong diffusion loss rate everywhere, on the plasma sheet ions and electrons, their coupling with the ionosphere, and their penetration into the inner magnetosphere. We simulate the earthward transport of ions and electrons from observationally based tail sources under self-consistent electric and magnetic field using the RCM coupled with a modified Dungey force-balanced magnetic field model. In addition, we also evaluate the effects as the Chen rate and strong diffusion rate everywhere decrease by factors of 2/3 and 1/3 to take into account the variation of the loss rates corresponding to different geomagnetic activity, as suggested by observations.

In the first part of this chapter we evaluated the effect of the different loss rates on the plasma sheet and inner magnetosphere electron population, as well as on energy fluxes of electrons precipitating into the ionosphere and as a result, on ionospheric Pedersen conductivity. Our results focused on substorm growth phase convection enhancement so that they can be compared more appropriately with observations.

We found that the electron pressures of the Chen rate cases are larger than those of the strong diffusion everywhere cases in the premidnight sector, since, beyond r ~8 R_E, the Chen lifetimes for higher energy electrons are much larger than the lifetime of strong diffusion everywhere at dusk. The lifetime of the Chen rate becomes significantly smaller than the strong diffusion lifetime with decreasing radial distance inside r ~7 $R_{E,}$ allowing the electrons penetrating to the inner magnetosphere to remain there for many hours or more under the Chen rate, while the electrons get lost within minutes under strong diffusion. The simulated electron energy spectrums in the inner magnetosphere under the Chen rate can qualitatively account for the 20 –

200 keV ring current electrons observed by THEMIS, but the same is not true for the strong-diffusion case. Therefore a more realistic loss rate is important for these high-energy electrons in the inner magnetosphere, and thus also for understanding the radiation belts since they are the seed population for the radiation belts.

Precipitating electron energy fluxes, and their resulting Pedersen conductivities in the ionosphere are found to be significantly enhanced at premidnight MLTs in the strong diffusion everywhere cases but not in the Chen rate cases. The dawn-dusk asymmetric profile of the precipitating energy fluxes in the Chen rate cases, with much higher energy flux at dawn rather than at dusk, agrees better with statistical DMSP observations compared to the asymmetry of the strong diffusion everywhere cases.

In the second part of the chapter, since we have established that using the more realistic Chen electron loss rate results in electron properties that are closer to the observed ones in both the ionosphere and magnetosphere than does the strong diffusion one, we investigated the effect of the different loss rates on the shielding of the convection electric field via ionospheric Pedersen conductivity. For this purpose, we focused on storm-like convection enhancement, for which the shielding development is more distinct.

We found that although at higher latitudes the conductivity in the strong diffusion everywhere case is stronger than in the Chen rate case, at lower latitudes there is a sharp decrease in the conductivity in the strong diffusion everywhere case. That sharp decrease is attributed to the high-energy electron population, responsible for the conductivity, being lost more rapidly due to lifetimes becoming very short inside 6 R_E for the strong diffusion everywhere rate. On the other hand, in the Chen rate case, the lifetimes increase significantly with decreasing distance allowing the electrons in the closed drift path region to remain there for a longer time and produce conductivity. This results in conductivity that extends further equatorward at all nightside MLTs. Therefore, the relatively higher conductivity at lower latitudes in the Chen rate case leads to less efficient shielding of the enhanced convection electric field, allowing for further inward penetration of the plasma sheet into the inner magnetosphere, compared to the strong diffusion everywhere case.

CHAPTER 5 | Summary and concluding remarks

We have conducted RCM simulations under self-consistent electric and magnetic fields in order to appropriately evaluate the plasma sheet transport into the near-Earth magnetosphere, focusing on the effects of three key factors on the large-scale M-I coupling: (1) plasma sheet ion and electron sources, (2) force balance between plasma and magnetic field, and (3) electron loss, its precipitation, and the resulting ionospheric conductivity.

Effect of plasma sheet ion and electron sources

We established from 11 years of Geotail observations the plasma sheet ion and electron sources for the RCM to realistically describe the sources as a function of particle energy, MLT, and the solar wind and IMF conditions. We first conducted RCM simulations under empirical non force-balanced T96 magnetic field to investigate how different plasma sheet states affect the M-I coupling. Responding to enhanced convection, the shielding is more efficient for a colder and denser plasma sheet, which is often found in the cases of northward IMF, than for a hotter and more tenuous plasma sheet found in the cases of southward IMF. A combination of higher pressure, and therefore stronger FAC in the near Earth region, and lower auroral conductance at low latitudes in the colder and denser plasma sheet, results in stronger shielding of the penetration electric field. On the other hand, in the hot and tenuous case, the pressure and FAC magnitudes in the inner magnetosphere are lower and the conductivity is higher, therefore the shielding is weaker.

This weaker shielding of the convection electric field under hotter and more tenuous plasma sheet leads to further earthward penetration of the low-energy protons and as a result to larger latitudinal and MLT extent of the Harang reversal, as well as stronger SAPS, than under colder and denser plasma sheet.

Effect of force-balanced magnetic field

Using the same plasma sources at our outer boundary based on observations, we conducted the RCM simulations i) coupled with a modified Dungey force-balanced magnetic field model, and ii) using the non-force balanced empirical T96 magnetic field model. Plasma transport under force-balanced magnetic field, compared with those under T96 magnetic field, results in weaker azimuthal pressure gradients in the inner magnetosphere, thus weaker R2 FAC and less efficient electric field shielding, allowing thermal plasma sheet protons and electrons to penetrate deeper into the inner magnetosphere. As a result, the inner edge of the thermal plasma sheet is more azimuthally symmetric under force-balanced magnetic field, while under T96 magnetic field there is a much more pronounced dawn-dusk asymmetry.

The locations of the inner edges and the relative position between the ion and electron edges determine the characteristics of the Harang reversal and the SAPS. The Harang reversal extends more towards dawn and the SAPS to be more confined in radial and latitudinal width under force-balanced magnetic field.

The magnitudes of the azimuthal pressure gradient, the inner edges of thermal protons and electrons, the latitudinal range of the Harang reversal, and the radial and latitudinal width of the SAPS become more consistent with observations when taking into account the feedback from force-balanced magnetic fields.

Effect of electron loss rate, precipitation, and resulting ionospheric conductivity

We conducted force-balanced RCM simulations using different electron loss rates: i) MLT dependent rate based on wave activity, and ii) strong diffusion everywhere loss rate.

Under the MLT dependent loss rate, the electron lifetimes become significantly longer with decreasing radial distance, allowing electrons that penetrated into the inner magnetosphere earlier to remain there for many hours or more, while under the strong diffusion loss rate everywhere, the electrons rapidly get lost within minutes. The simulated electron energy spectrums in the inner magnetosphere under MLT dependent loss rate, but not those under the strong diffusion everywhere, can qualitatively account for the tens to hundreds of keV ring current electrons observed by THEMIS inside ~7 R_E, which constitute the seed population for the radiation belts. Also, this high-energy electron population remaining in the near-Earth region under the MLT dependent loss rate produces substantial conductivity at lower latitudes. As convection is enhanced, this substantial conductivity allows for less efficient shielding, thus deeper penetration of the ion plasma sheet into the inner magnetosphere than under the strong diffusion everywhere rate.

Finally, the dawn-dusk asymmetry in the precipitating electron energy fluxes under the MLT dependent loss rate, with much higher energy flux at dawn rather than at dusk, agrees better with statistical DMSP observations.

As a concluding remark, we should note that the above simulations are a significant step forward to our understanding of the physical processes involved in the interplay between plasma transport and electric and magnetic fields in the inner magnetosphere. The more realistic, quantitative, self-consistent modeling of the interplay also provides more accurate account of the changes in the near-Earth magnetosphere that are critical to the development of storms and substorms.

REFERENCES

Akasofu, S.-I. (1964), The development of the auroral substorm, *Planet. Space Sci.*, 12, 273-282.

Albert, J. M. (1994), Quasi-linear pitch angle diffusion coefficients: Retaining high harmonics, *J. Geophys. Res.*, 99, 23,741– 23,745.

Anderson, P. C., R. A. Heelis, and W. B. Hanson (1991), The ionospheric signatures of rapid subauroral ion drifts, *J. Geophys. Res.*, *96*(A4), 5785–5792.

Anderson, P. C., D. L. McKenzie, M. J. Brittnacher, M. W. Chen, M. Hairston, and M. F. Thomsen (2000), Global storm time auroral X-ray morphology and timing and comparison with UV measurements, *J. Geophys. Res.*, 105, 15,757– 15,777.

Anderson, P. C., D. L. Carpenter, K. Tsuruda, T. Mukai, and F. J. Rich (2001), Multisatellite observations of rapid subauroral ion drifts (SAID), *J. Geophys. Res.*, *106*, 29,585–29,599, doi:10.1029/2001JA000128.

Ashour-Abdalla, M., and C. F. Kennel (1978), Diffuse auroral precipitation, *J. Geomagn. Geolectr.*, 30, 239– 255.

Brandt, P. C., S. Ohtani, D. G. Mitchell, M.-C. Fok, E. C. Roelof, and R. Demajistre (2002), Global ENA observations of the storm mainphase ring current: Implications for skewed electric fields in the inner magneto- sphere, *Geophys. Res. Lett., 29*(20), 1954, doi:10.1029/2002GL015160.

Bristow, W. A. and P. Jensen (2007), A superposed epoch study of SuperDARN convection observations during substorms, *J. Geophys. Res., 112*, A06232, doi:10.1029/2006JA012049.

Buzulukova, N., M.-C. Fok, J. Goldstein, P. Valek, D. J. McComas, and P. C. Brandt (2010), Ring current dynamics in moderate and strong storms: Comparative analysis of TWINS and

IMAGE/HENA data with the Comprehensive Ring Current Model, J. Geophys. Res., 115, A12234, doi:10.1029/2010JA015292.

Cahill, L., Jr. (1966), Inflation of the inner magnetosphere during a magnetic storm, J. Geophys. Res., 71, 4505–4519.

Chapman, S., and V. C. A. Ferraro (1930), A new theory of magnetic storms, *Nature* 126:129

Chapman, S., and V. C. A. Ferraro (1931), A new theory of magnetic storms, *Terr. Magn. Atmosph. Elec.* 36:171-86

Chapman, S., and V. C. A. Ferraro (1932), A new theory of magnetic storms, *Terr. Magn. Atmosph. Elec.* 37:147-56

Chen, M. W., L. R. Lyons, and M. Schulz (1994), Simulations of phase space distributions of storm time proton ring current, *J. Geophys. Res., 99*(A4), 5745–5759.

Chen, M. W., and M. Schulz (2001), Simulations of diffuse aurora with plasma sheet electrons in pitch angle diffusion less than everywhere strong, *J. Geophys. Res.*, *106*(A12), 28,949–28,966, doi:10.1029/2001JA000138.

De Zeeuw, D. L., S. Sazykin, R. A. Wolf, T. I. Gombosi, A. J. Ridley, and G. To´th (2004), Coupling of a global MHD code and an inner magnetospheric model: Initial results, J. Geophys. Res., 109, A12219, doi:10.1029/2003JA010366.

Dungey, J. W. (1963), The structure of the exosphere or adventures in velocity space, in Geophysics, *The Earth's Environment*, edited by C. DeWitt, J. Hieblot, and A. Lebeau, pp. 503 – 550, Gordon and Breach, London.

Ebihara, Y., and M.-C. Fok (2004), Postmidnight storm-time enhancement of tens-of-keV proton flux, *J. Geophys. Res., 109*, A12209, doi:10.1029/2004JA010523.

Ebihara, Y., M.-C. Fok, R. A. Wolf, M. F. Thomsen, and T. E. Moore (2005), Nonlinear impact of plasma sheet density on the storm-time ring current, J. Geophys. Res., 110, A02208, doi:10.1029/2004JA010435.

Erickson, G. M., R. W. Spiro and R. A. Wolf (1991), The physics of the Harang discontinuity, *J. Geophys. Res., 96*, 1633-1645.

Foster, J. C., and W. J. Burke (2002), SAPS: A new categorization for sub-auroral electric fields, *Eos Trans. AGU*, *83*(36), 393.

Freeman, J. W., R. A. Wolf, R. W. Spiro, and B. Hausman, B. Bales, R. Hilmer, A. Nagai, and R. Lambour, Magnetospheric specification model development code documentation, scientific description, and software documentation, contract F19628-90-K-0012, Rice Univ. for Air Force Geophy. Lab., Hanscom Air Force Base, Mass., July 1993.

Garner, T. W. (2003), Numerical experiments on the inner magnetospheric electric field, *J. Geophys. Res.*, *108*(A10), 1373, doi:10.1029/2003JA010039.

Gkioulidou, M., C.-P. Wang, L. R. Lyons, and R. A. Wolf (2009), Formation of the Harang reversal and its dependence on plasma sheet conditions: Rice convection model simulations, *J. Geophys. Res., 114*, A07204, doi:10.1029/2008JA013955.

Gkioulidou, M., C.-P. Wang, and L. R. Lyons (2011), Effect of self-consistent magnetic field on plasma sheet penetration to the inner magnetosphere: Rice convection model simulations combined with modified Dungey force-balanced magnetic field solver, *J. Geophys. Res.*, 116, A12213, doi:10.1029/2011JA016810.

Gkioulidou, M., C.-P. Wang, Wing S., and L. R. Lyons (2012), Effect of a MLT dependent electron loss rate on the magnetosphere – ionosphere coupling, *J. Geophys. Res*., submitted.

Harang, L. (1946), The mean field of disturbance of polar geomagnetic, *Terr. Magn. Atmos. Electr.*, *51*(3), 353–380.

Hardy, D., M. Gussenhoven, and E. Holeman (1985), A Statistical Model of Auroral Electron Precipitation, *J. Geophys. Res., 90*(A5), 4229-4248.

Hardy, D. A., M. S. Gussenhoven, R. Raistrick, and W. J. McNeil (1987), Statistical and functional representations of the pattern of auroral energy flux, number flux, and conductivity, *J. Geophys. Res.*, 92, 12,275 – 12,294.

Harel, M., R. A. Wolf, P. H. Reiff, R. W. Spiro, W. J. Burke, F. J. Rich, and M. Smiddy (1981a), Quantitative simulation of a magnetospheric substorm 1, model logic and overview, *J. Geophys. Res., 86*, 2217-2241.

Harel, M., R. A. Wolf, P. H. Reiff, R. W. Spiro, W. J. Burke, F. J. Rich, and M. Smiddy (1981b), Quantitative simulation of a magnetospheric substorm 2, comparison with observations, *J. Geophys. Res., 86*, 2242-2260.

Hesse, M., and J. Birn (1993), Three-dimensional magnetotail equilibria by numerical relaxation techniques, *J. Geophys. Res.*, 98, 3973–3982.

Hsu, T.-S., R. L. McPherron, J. Kissinger, X. Chu, H. Zhang, Y. S. Ge, and R. J. walker (2012), An Investigation of the Solar Cycle Effect on Substorms, *J. Geophys. Res.*, to be submitted.

Hu, B., F. R. Toffoletto, R. A. Wolf, S. Sazykin, J. Raeder, D. Larson, and A. Vapirev (2010), One-way coupled OpenGGCM/RCM simulation of the 23 March 2007 substorm event, J. Geophys. Res., 115, A12205, doi:10.1029/2010JA015360

Iijima, T., and T. A. Potemra (1976), The Amplitude Distribution of Field-Aligned Currents at Northern High Latitudes Observed by Triad, *J. Geophys. Res.*, *81*(13), 2165–2174, doi:10.1029/JA081i013p02165.

Jordanova, V. K., S. Zaharia, and D. T. Welling (2010), Comparative study of ring current development using empirical, dipolar, and self-consistent magnetic field simulations, *J. Geophys. Res., 115*, A00J11, doi:10.1029/2010JA015671.

Johnstone, A. D., D. M. Walton, R. Liu, and D. A. Hardy (1993), Pitch angle diffusion of low-energy electrons by whistler mode waves, *J. Geophys. Res.*, 98, 5959– 5967.

Kennel, C. F. and H. E. Petschek (1966), "Limit on stably trapped particle fluxes", *J. Geophys. Res.*, 71, 1.

Kennel, C. F., F. L. Scarf, R. W. Fredricks, J. H. McGehee, and F. V.Coroniti (1970), VLF electric field observations in the magnetosphere, *J. Geophys. Res.*, 75, 6136–6152.

Kennel, C. F., and M. Ashour-Abdalla (1982), Electrostatic waves and the strong diffusion of magnetospheric electrons, in *Magnetospheric Plasma Physics*, edited by A. Nishida, pp. 245–344, Cent. Acad. Publ., Tokyo.

Koons, H. C., and J. L. Roeder (1990), A survey of equatorial magnetospheric wave activity between 5 and 8 R_E, *Planet. Space Sci.*, 38, 1335–1341.

Lemon, C., R. A. Wolf, T. W. Hill, S. Sazykin, R. W. Spiro, F. R. Toffoletto, J. Birn, and M. Hesse (2004), Magnetic storm ring current injection modeled with the Rice Convection Model and a self-consistent magnetic field, *Geophys. Res. Lett., 31*, L21801, doi:10.1029/2004GL020914.

Liemohn, M. W., J. U. Kozyra, C. R. Clauer, and A. J. Ridley (2001), Computational analysis of the near-Earth magnetospheric current system during two-phase decay storms, *J. Geophys. Res.*, *106*(A12), 29,531–29,542, doi:10.1029/2001JA000045.

Liu, S., M. W. Chen, M. Schulz, and L. R. Lyons (2006), Initial simulation results of storm-time ring current in a self- consistent magnetic field model, *J. Geophys. Res., 111*, A04225, doi:10.1029/2005JA011194.

Lyons, L. R., Electron diffusion driven by magnetospheric electrostatic waves, *J. Geophys. Res.*, 79, 575– 580, 1974.

Lyons, L. R., and D. J. Williams, Quantitative Aspects of Magnetospheric Physics (1984), *D. Reidel, Dordrecht, Holland*.

Lyons, L. R., C.-P. Wang, and T. Nagai (2003), Substorm onset by plasma sheet divergence, *J. Geophys. Res.*, *108* (A12), 1427, doi: 10.1029/2003JA010178.

Matsui, H., P. A. Puhl-Quinn, J. W. Bonnell, C. J. Farrugia, V. K. Jordanova, Yu. V. Khotyaintsev, P.-A. Lindqvist, E. Georgescu, and R. B. Torbert (2010), Characteristics of storm time electric fields in the inner magnetosphere derived from Cluster data, *J. Geophys. Res.*, 115, A11215, doi:10.1029/2010JA015450.

McPherron, R. L., C. T. Russell, and M. Aubry (1973), Satellite studies of magnetospheric substorms on August 15, 1978, 9, Phenomenological model for substorms, *J. Geophys. Res.*, 78, 3131-3149.

Meredith, N. P., A. D. Johnstone, S. Szita, R. B. Horne, and R. R. Anderson (1999), ‘‘Pancake’’ electron distributions in the outer radiation belts, *J. Geophys. Res.*, 104, 12,431-12,444.

Merkin, V. G., and J. G. Lyon (2010), Effects of the low-latitude ionospheric boundary condition on the global magnetosphere, J. Geophys. Res., 115, A10202, doi:10.1029/2010JA015461.

Nakamura, M., G. Paschmann, W. Baumjohann, and N. Sckopke (1991), Ions distributions and flows near the neutral sheet, *J. Geophys. Res.*, *96*, 5631–5649.

Ni, B., R. M. Thorne, R. B. Horne, N. P. Meredith, Y. Y. Shprits, L. Chen, and W. Li (2011a), Resonant scattering of plasma sheet electrons leading to diffuse auroral precipitation: 1. Evaluation for electrostatic electron cyclotron harmonic waves, *J. Geophys. Res.*, 116, A04218, doi:10.1029/2010JA016232.

Ni, B., R. M. Thorne, N. P. Meredith, R. B. Horne, and Y. Y. Shprits (2011b), Resonant scattering of plasma sheet electrons leading to diffuse auroral precipitation: 2. Evaluation for whistler mode chorus waves, *J. Geophys. Res.*, 116, A04219, doi:10.1029/2010JA016233.

Nielsen, E., and R.A. Greenwald (1979), Electron flow and visual aurora at the Harang discontinuity, *J. Geophys. Res.*, *84* (A8), 4189-4199.

Nishimura, Y., J. Wygant, T. Ono, M. Iizima, A. Kumamoto, D. Brautigam, and R. Friedel (2008), SAPS measurements around the magnetic equator by CRRES, *Geophys. Res. Lett., 35*, L10104, doi:10.1029/ 2008GL033970.

Pembroke, A., F. Toffoletto, S. Sazykin, M. Wiltberger, J. Lyon, V. Merkin, and P. Schmitt (2012), Initial results from a dynamic coupled magnetosphere-ionosphere-ring current model, *J. Geophys. Res.*, 117, A02211, doi:10.1029/2011JA016979.

Roberts, C. S. (1969), Pitch angle diffusion of electrons in the magnetosphere, *Rev. Geophys.*, 7, 305– 337.

Robinson, R. M., R. R. Vondrak, K. Miller, T. Dabbs, and D. Hardy (1987), On calculating ionospheric conductances from the flux and energy of precipitating electrons, *J. Geophys. Res., 92*, 2565-2569.

Rodger, A. S., S. W. H. Cowley, M. J. Brown, M. Pinnock, and D. A. Simmons (1984), Dawn-Dusk (y) component of the interplanetary magnetic field and the local time of the Harang discontinuity, *Planet. Space Sci., 32*, 8, 1021-1027.

Schulz, M., and M. Chen (2008), Field-line (Euler-potential) model of the ring current, 327 *J. Sol. Terr. Phys., 70*, 482–489.

Schumaker, T. L., M. S. Gussenhoven, D. A. Hardy, and R. L. Carovillano (1989), The relationship between diffuse auroral and plasma sheet electron distributions near local midnight, *J. Geophys. Res.*, 94, 10,061 – 10,078.

Sergeev, V. A., E. M. Sazhina, and N. A. Tsyganenko (1983), Pitch-angle scattering of energetic protons in the magnetotail current sheet as the dominant source of their isotropic precipitation into the nightside ionosphere, *Planet. Space Sci.*, 31,10, 1147-1155.

Sonnerup, B. U. Ö. (1980), Theory of the Low-Latitude Boundary Layer, *J. Geophys. Res.*, *85*(A5), 2017–2026, doi:10.1029/JA085iA05p02017.

Southwood, D. J., and R. A. Wolf (1978), An Assessment of the Role of Precipitation in Magnetospheric Convection, *J. Geophys. Res.*, *83*(A11), 5227–5232.

Stiles, G. S., E. W. Hones, Jr., S. J. Bame, and J. R. Asbridge (1978), Plasma sheet pressure anisotropies, *J. Geophys. Res*., *83*, 3166–3172.

Thomsen, M. F., J. E. Borovsky, R. M. Skoug, and C. W. Smith (2003), Delivery of cold, dense plasma sheet material into the near-Earth region, *J. Geophys. Res.*, 108(A4), 1151, doi:10.1029/2002JA009544.

Thorne, R. M., Y. Y. Shprits, N. P. Meredith, R. B. Horne, W. Li, and L. R. Lyons (2007), Refilling of the slot region between the inner and outer electron radiation belts during geomagnetic storms, J. Geophys. Res., 112, A06203, doi:10.1029/2006JA012176.

Toffoletto, F. R., Spiro, R. W., Wolf, R. A., Hesse, M. and Birn, J. (1996), Self-consistent Modeling of Inner Magnetospheric Convection, in E. J. Rolfe nd B. Kaldeich (eds.), *Third International Conference on Substorms (ICS-3)*, ESA Publications Division, Noordwijk, The

Netherlands, pp. 223–230.

Toffoletto, F. R., J. Birn, M. Hesse, R. W. Spiro (2001), and R. A. Wolf, Modeling Inner Magnetospheric Electrodynamics, in *Space Weather, Geophys Monograph Ser., vol. 125*, edited by P. Song, H. Singer, and G. Siscoe, pp. 265, AGU, Washington, D. C.

Toffoletto, F., S. Sazykin, R. Spiro, and R. Wolf (2003), Inner magnetospheric modeling with the Rice Convection Model, *Space Science Reviews*, *107*, 175-196.

Toffoletto, F., S. Sazykin, R. Spiro, R. Wolf, and J. Lyon (2004), RCM meets LFM: Initial results of one-way coupling, *J. Atmos. Sol. Terr. Phys.*, 66(15–16), 1361–1370, doi:10.1016/j.jastp.2004.03.022.

Tsyganenko, N. A. (1995), Modeling the Earth's magnetospheric magnetic field confined within a realistic magnetopause, *J. Geophys. Res.*, *100*, 5599-5612.

Tsyganenko, N. A. (1996), Effects of the solar wind conditions on the global magnetospheric configuration as deduced from data-based field models, in *Proceedings of the ICS-3 Conference on Substorms, Eur. Space Agency Spec. Publ., ESA SP-389*, 181-185.

Vasyliunas, V. M. (1970), Mathematical models of magnetospheric convections and its coupling to the ionosphere. In: McCormac, B. M. (Ed.), *Particles and Fields in the Magnetosphere*. D. Reidel, Hingham, MA, pp. 60-71.

Villalón, E., and W. J. Burke (1995), Pitch Angle Scattering of Diffuse Auroral Electrons by Whistler Mode Waves, *J. Geophys. Res.*, *100*(A10), 19,361–19,369, doi:10.1029/95JA01161.

Wang, C.-P., L. R. Lyons, M. W. Chen, R. A. Wolf, and F. R. Toffoletto (2003), Modeling the inner plasma sheet protons and magnetic field under enhanced convection, *J. Geophys. Res., 108*(A2), 1074, doi:10.1029/2002JA009620.

Wang, C.-P., L. R. Lyons, T. Nagai, and J. C. Samson (2004), Midnight radial profiles of the quiet and growth-phase plasma sheet: The Geotail observations, *J. Geophys. Res., 109*, A12201, doi:10.1029/2004JA010590.

Wang, C.-P., L. R. Lyons, T. Nagai, J. M. Weygand, and R. W. McEntire (2007), Sources, transport, and distributions of plasma sheet ions and electrons and dependences on interplanetary parameters under northward interplanetary magnetic field, *J. Geophys. Res., 112*, A10224, doi:10.1029/2007JA012522.

Wang, C.-P., L. R. Lyons, V. Angelopoulos, D. Larson, J. P. McFadden, S. Frey, H.-U. Auster, and W. Magnes (2008), THEMIS observations of penetration of the plasma sheet into the ring current region during a magnetic storm, *Geophys. Res. Lett.*, 35, L17S14, doi:10.1029/ 2008GL033375.

Wang, C.-P., M. Gkioulidou, L. R. Lyons, V. Angelopoulos, R. A. Wolf, T. Nagai, J. M. Weygand, A. T. Y. Lui (2011), Spatial distributions of ions and electrons from the plasma sheet to the inner magnetosphere: comparisons between THEMIS-Geotail statistical results with the Rice Convection Model, *J. Geophys. Res.*, submitted.

Wang, H., H. Lühr, K. Häusler, and P. Ritter (2011), Effect of subauroral polarization streams on the thermosphere: A statistical study, *J. Geophys. Res., 116*, A03312, doi:10.1029/2010JA016236.

Weimer, D. (1995), Models of High-Latitude Electric Potentials Derived with a Least Error Fit of Spherical Harmonic Coefficients, *J. Geophys. Res.,* 100(A10), 19595-19607.

Wing, S., and P. T. Newell (2002), 2D plasma sheet ion density and tem- perature profiles for northward and southward IMF, *Geophys. Res. Lett.*, 29(9), 1307, doi:10.1029/2001GL013950.

Wing, S., J. R. Johnson, P. T. Newell, and C.-I. Meng (2005), Dawn-dusk asymmetries, ion spectra, and sources in the northward interplanetary magnetic field plasma sheet, *J. Geophys. Res.*, 110, A08205, doi:10.1029/2005JA011086.

Wolf, R. A. (1983), The quasi–static (slow–flow) region of the magnetosphere, in *Solar Terrestrial Physics*, edited by R. L. Carovillano and J. M. Forbes, pp. 303–368, D. Reidel, Hingham, MA.

Xing, X., L. R. Lyons, V. Angelopoulos, D. Larson, J. McFadden, C. Carlson, A. Runov, and U. Auster (2009), Azimuthal plasma pressure gradient in quiet time plasma sheet, *Geophys. Res. Lett., 36*, L14105, doi:10.1029/ 2009GL038881.

Yang, J., F. R. Toffoletto, and Y. Song (2010), Role of depleted flux tubes in steady magnetospheric convection: Results of RCM-E simulations, *J. Geophys. Res., 115*, A00I11, doi:10.1029/2010JA015731.

Zaharia, S., Cheng, C. Z., and Maezawa, K. (2004): 3-D force-balanced magnetospheric configurations, *Ann. Geophys., 22*, 251-265, doi:10.5194/angeo-22-251-2004.

Zaharia, S. (2008), Improved Euler potential method for three-dimensional magnetospheric equilibrium, *J. Geophys. Res., 113*, A08221, doi:10.1029/2008JA013325.

Zou, S., L. R. Lyons, C.-P. Wang, A. Boudouridis, J. Ruohoniemi, P. Anderson, P. Dyson, and J. Devlin (2009), On the coupling between the Harang reversal evolution and substorm dynamics: a synthesis of SuperDARN, DMSP and IMAGE observations, *J. Geophys. Res., 114*, A01205, doi:10.1029/ 2008JA013449 .